Alma Mater Studiorum – Università di Bologna

DOTTORATO DI RICERCA IN

MECCANICA E SCIENZE AVANZATE DELL'INGEGNERIA

Ciclo XXXIII

Settore Concorsuale: 09/A1 - INGEGNERIA AERONAUTICA, AEROSPAZIALE E NAVALE

Settore Scientifico Disciplinare: ING-IND/07 - PROPULSIONE AEROSPAZIALE

ANALYSIS OF THE MAIN PHENOMENA AFFECTING SOLID ROCKET MOTORS INTERNAL BALLISTICS

Presentata da: Ing. Stefano Mini

Coordinatore Dottorato

Prof. Marco Carricato

Supervisore

Prof. Fabrizio Ponti

Co-supervisore

Prof. Nicolò Cavina

Esame finale anno 2021

Abstract

In solid rocket motors, the absence of combustion controllability and the large amount of financial resources involved in full-scale firing tests, increase the importance of numerical simulations in order to asses stringent mission thrust requirements and evaluate the influence of thrust chamber phenomena affecting the grain combustion. Among those phenomena, grain local defects (propellant casting inclusions and debondings), combustion heat accumulation involving pressure peaks (Friedman Curl effect), and case-insulating thermal protection material ablation affect thrust prediction in terms of not negligible deviations with respect to the nominal expected trace. Most of the recent models have proposed a simplified treatment to the problem using empirical corrective functions, with the disadvantages of not fully understanding the physical dynamics and thus of not obtaining predictive results for different configurations of solid rocket motors in a boundary conditions-varied scenario.

This work is aimed to introduce different mathematical approaches to model, analyze, and predict the abovementioned phenomena, presenting a detailed physical interpretation based on existing SRMs configurations. Internal ballistics predictions are obtained with an in-house simulation software, where the adoption of a dynamic three-dimensional triangular mesh together with advanced computer graphics methods, allows the previous target to be reached. Numerical procedures are explained in detail. Simulation results are carried out and discussed based on experimental data.

Acknowledgements

I would sincerely like to thank those people making research possible at University of Bologna.
Thank you, Prof. Ponti, for the chance you have given me to attend this PhD experience: I would like to thank you for your courtesy, for the support you have given me every day in the lab, and for your contribution to this thesis which would not have been the same without your help. Last but not least, I would like to thank all my lab. colleagues sharing with me this adventure.
Inoltre, vorrei ringraziare tutti coloro che mi hanno supportato in questo percorso.
In primo luogo, grazie ai miei genitori per essermi stati sempre vicini e avermi incoraggiato nei momenti di sconforto.
Grazie a tutti i miei parenti su cui posso sempre contare.
Grazie agli amici di vecchia data per avermi offerto momenti di vero divertimento.
Grazie a tutti quelli che sono stati e sono tuttora presenti nella mia vita.

Contents

List of Figures

Chapter 1

1 Introduction

Solid rocket motors (SRMs) (Figure 1) represent a class of chemical propulsion engines where the thrust is produced by the ejecting of stored matter, namely the grain.

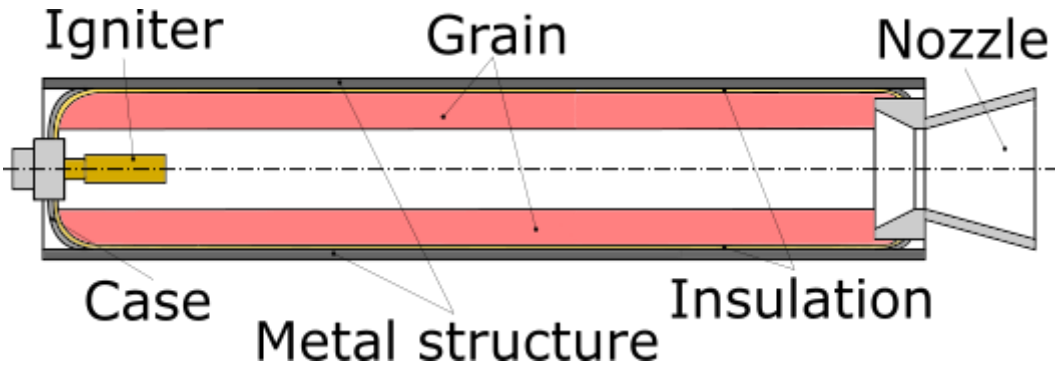

Figure 1: Solid rocket motor conceptual scheme.

Specifically, the energy source of SRMs is based on solid propellant stored within a metallic tank, namely the case. Once ignited, the propellant leads to the production of combustion hot gases which undergo a thermodynamic expansion in a convergent-divergent nozzle: indeed, the internal energy of the gas is converted into the kinetic energy of the exhaust flow and the thrust is produced by the gas pressure on the surfaces exposed to the gas. The energy from a high-pressure combustion reaction of solid propellant chemicals, permits the heating of reaction product gases to very high temperatures (3000 to 4000 K). Those gases are subsequently accelerated in the nozzle to high velocities (1800 to 4300 $^{m}/_{s}$) [1].

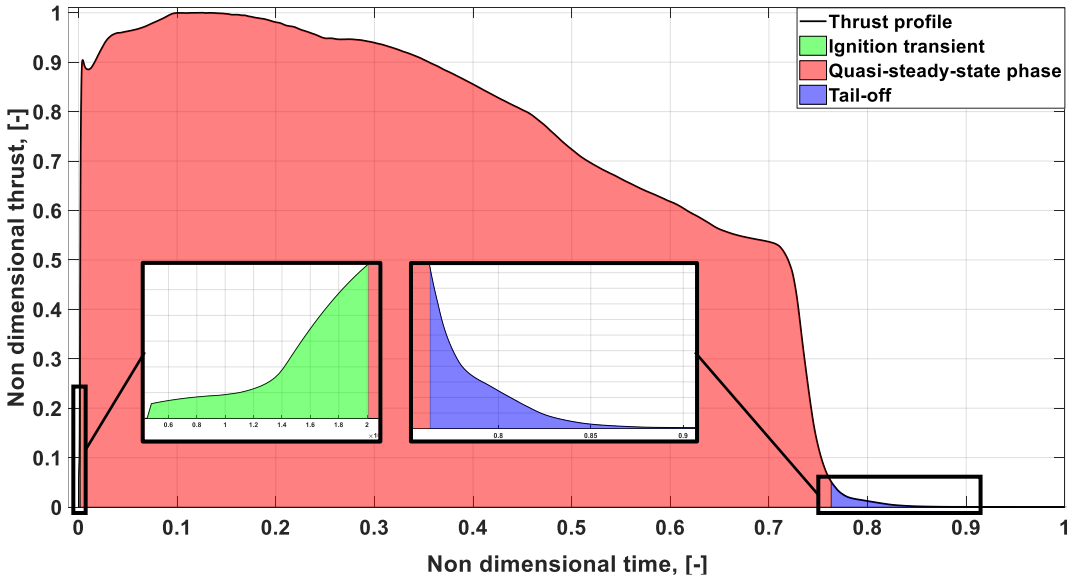

Figure 2: Thrust-time profile.

From a theoretical point of view, the main design performance parameter of a SRM is the thrust-time

profile (Figure 2). Quasi-steady-state phase represents the 90÷95% of the entire combustion period [1] and is propellant burning driven; the other two phases, namely the ignition transient and the tail-off are very bounded in time. In particular, the ignition transient phase is the interval between the release of ignition energy (usually released by the igniter) and the quasi steady-state phase. On the other hand, tail-off period is defined as the thrust-time window ranging between the ending of the quasi steady-state phase, namely the burn-out (i.e., when all the propellant is burnt) and the end of thrust production. As for the ignition transient, even the tail-off shows the occurrence of many unsteady phenomena, as will be highlighted in subchapter 1.2. In addiction to that, another rocket typical parameter is the specific impulse value, namely a measure of how effectively a rocket is able to generate 1 N of thrust per unit mass of propellant burnt. Specifically, for SRMs it can range up to 250 s in vacuum, with respect to liquid engines specific impulse which reaches values in the order of 450 s. Although liquid engines seem to have superior qualities in terms of specific impulse and controllability, solid rockets are usually relatively simple from a design perspective. In fact, they technically rely on a low number of moving parts, thus they are usually relatively simple, are easy to apply and require little servicing. Because of that, SRMs are commonly used in military applications or as boosters of large-size launchers (for instance Space Shuttle SRB (Solid Rocket Boosters) or ARIANE V boosters) or as stages in small-to-medium size launchers (for instance VEGA launcher). However, despite their relative design simplicity, they cannot be fully checked before ignition, and thrust cannot be controlled and varied after the propellant ignition. Due to the absence of thrust magnitude controllability during flight, extensive research has been conducted for decades to find the optimal design strategy in order to achieve the conflicting trade off among safety, reliability, performance, and cost [2].

1.1 Thesis motivation

Despite their relative design simplicity, solid rocket motors show a variety of phenomena affecting the grain combustion, and then the thrust prediction [3-6]. In the design and development of a new motor, the use of numerical simulations able to predict and reconstruct in an accurate way the rocket behavior in all its operative conditions is fundamental. Indeed, more accurate predictions would decrease the whole development cost of the design process since it would be reduced the need of full-scale firing tests. The result is a more efficient design by means of fast engineering simulation methods, required to model, and recreate launcher internal thermodynamics. Furthermore, once ignited, a solid rocket motor cannot be shut off thus the combustion chamber pressure/thrust should be as close as possible to experimental data. The above-mentioned statement implies the importance of modelling a great amount of the phenomena affecting the SRMs internal ballistics. Currently, in aerospace companies, the heterogeneities encountered during the combustion of solid propellant are collected in a nonlinear normalized local rate ratio, namely the Hump function, which includes all the imperfections coming from the manufacturing process too. Because of that, the Hump parameter is involved in the prediction of motor performances [7].
The scope of the present work is to evaluate some of those thrust-influencing phenomena occurring in SRMs in the direction of decreasing the error gap between simulations and experiments, hence reducing the impact of the nonlinear Hump functions in simulations as well.

1.2 Thesis objectives

The present thesis is aimed to model the following thrust-influencing phenomena occurring in the combustion chamber of SRMs in order to predict and evaluate the possible implications on internal ballistics dynamics and performance. First, among those phenomena, the main factor influencing the combustion chamber pressure/thrust in the quasi-steady state is the time evolution of the burning surface and the surface regression rate. However, during propellant casting process, small amounts

of air could be trapped in the propellant due to propellant's high viscosity and high density. Hence, inclusions occurrence take place, leading to an anomalous evolution of the main burning surface. Indeed, when the air inclusions are exposed to combustion, the flame propagation through them is faster, thus causing a significative burning surface progression increase. Unexpected variations in combustion chamber pressure pattern and early thermal protections exposure could be generated because of an anomalous burning surface regression. The same effect is also produced by propellant debondings, namely a type of void originated through the separation between the propellant and the insulation layer. Besides that, tail-off phase also requires a deeper attention. In fact, especially for multi-stage launchers, the tail-off thrust behavior is essential for the proper sequencing of stage separation, and to properly design and manage interstage wait times and separation systems total impulse. In the time range of the abovementioned phase, two phenomena could take place. First, a pressure peak, namely Friedman Curl effect [8], could occur due to a heat redistribution next to the case which leads to an increment of the burning rate. At present, the primary cause Friedman curl origins from, has not been exhaustively explained. Thus, Friedman Curl has been investigated and modelled with both the aims of a deeper understanding of the physical phenomenon and of obtaining a more accurate estimation of tail-off phase. In addition to that, as reported by experimental observations, upper stages SRMs tail-off residual thrust can last tens of seconds after the burn-out time. Past literature [9-11] has shown that the main factor, leading to the abovementioned statement, is represented by pyrolysis gases produced by the ablation of the case-insulating thermal protections (Figure 1). Boraas [9] argued that the heat source leading to the thermal protection material ablation is the radiated power by the alumina molten slag. The present study aims to integrate the previous contribution with another heat source, namely the radiated power by the nozzle region within the combustion chamber. All those sources of possible deviations from the SRM standard thrust performance are investigated and evaluated considering real test cases. Experimental results are provided by AVIO S.p.A, an Italian aerospace company which manages the design and manufacturing of the SRMs stages of VEGA launcher and of the solid rocket boosters of ARIANE V launcher.

1.3 Thesis outline

The thesis is structured as follows:

- **Chapter 2** relies on a general introduction of ROcket BOOst Simulation Tool (ROBOOST) software.
- **Chapter 3** investigates the presence of inclusions within the grain and their influence on SRM performance.
- **Chapter 4** suggests a simplified approach to model and predict the Friedman Curl effect appearing on pressure-time profiles of some SRMs.
- **Chapter 5** evaluates the effect of case-insulating thermal protection ablation on the thrust tail-off.
- **Chapter 6** concludes the thesis by summarizing the main outcomes of the research.

References

[1] Sutton, G., P., and Biblarz, O., "Rocket Propulsion Elements", *Rocket Testing,* 7th ed., John Wiley & Sons Inc., New York, 2010, pp. 711-726.

[2] Mahjub, A., Mazlan, N., M., Abdullah, M., Z., and Azam, Q., "Design Optimization of Solid Rocket Propulsion: A Survey of Recent Advancements," *Journal of Spacecraft and Rockets*, vol. 57, No. 1, 2020, pp. 3-11. https://doi.org/10.2514/1.A34594

[3] Hessler, R., O., and Glick, R. L., "Consistent Definitions for Burning-Rate Measurements in Solid Rocket Motors," *Combustion Explosion and Shock Waves*, Vol. 36, No. 1, 2000, pp. 83-106. https://doi.org/10.1007/BF02701517

[4] Majdalani, J., and Van Moorhen, W., K., "Improved Time-Dependent Flowfield Solution for Solid Rocket Motors," *AIAA Journal*, Vol. 36, No., 2, 1998, pp. 241-248. https://doi.org/10.2514/2.7507

[5] Sotter, G. and Swithenbank, J., "Vortices in Solid Propellant Rocket Motors," *AIAA Journal*, Vol. 1, No. 7, 1963, pp. 1682-1684. https://doi.org/10.2514/3.1891

[6] Kordig, J., W., and Fuller, G., H., "Correlation of Nozzle Submergence Losses in Solid Rocket Motors," *AIAA Journal*, Vol. 5, No. 1, 1967, pp. 175-177. https://doi.org/10.2514/3.3933

[7] Anthoine, J., Jézéquel, P., Prévost, M., Prévot, P., and Casalis, G., "Variable Fuel Grains Burn Velocities to Reduce Solid Rocket Motor Pressure Oscillations," *Journal of Propulsion and Power*, Vol. 31, No. 1, 2015, pp. 342-351. https://doi.org/10.2514/1.B35206

[8] Fry, R., S., "Solid Propellant Test Motor Scaling," Chemical Propulsion Information Agency (CPIA), CPTR73, Columbia, Maryland, July 2001.

[9] Boraas, S., Hyland, B., and Smart, L., "Predicted Post Burn Residual Thrust of an Orbital Transfer Motor,"AIAA Paper 1985-1395, July 1985. https://doi.org/10.2514/6.1985-1395

[10] Chang, I-S, "Slag and Enviroment of a Spinning Rocket Motor," *Journal of Spacecraft and Rockets*, Vol. 28, No. 5, 1991, pp. 599-605. https://doi.org/10.2514/3.26286

[11] Akiba, R., and Kohno, M., "Experiments with Solid Rocket Technology in the Development of M-3SII," *Acta Astronautica*, Vol. 13, No. 6/7, 1986, pp. 349-361. https://doi.org/10.1016/0094-5765(86)90090-1

Chapter 2

2 ROcket BOOst Simulation Tool (ROBOOST)

Nomenclature

Latin

A_p	=	port area, m^2
a	=	burning rate experimental factor, $m^{1-n} \cdot s^{2n-1} \cdot kg^{-n}$
c_v	=	combustion chamber gas specific heat at constant volume, $J/(kg \cdot K)$
F_{anis_i}	=	anisotropy factor of burning surface mesh *i-th* node, [-]
H_f	=	combustion enthalpy, J/kg
n	=	burning rate experimental exponent, [-]
P_b	=	burning perimeter, m
p	=	combustion chamber static pressure, Pa
p_{0_i}	=	combustion chamber pressure of burning surface mesh *i-th* node, Pa
r_b	=	burning rate, $[m/s]$
r_{b_i}	=	burning rate of burning surface mesh *i-th* node, m/s
t	=	time, s
t_0	=	reference time, s
u	=	combustion chamber gas velocity, m/s
ΔS_i	=	displacement of burning surface mesh *i-th* node, m
Δt	=	simulation time step, s

Greek

ρ	=	combustion chamber gas density, kg/m^3

Acronyms

$2D$	:	Two-dimensional
$3D$	:	Three-dimensional
CAD	:	Computer Aided Design
MDF	:	Minimum Distance Function
$PIBAL$	:	Propulsion and Internal BALlistic software
$ROBOOST$	:	Rocket BOOst Simulation Tool
$SNPE$	:	Sociètè Nationale des Poudres et des Explosifs
SPP	:	Solid Propellant rocket motor Performance computer program
SRM	:	Solid Rocket Motor
$ZEFIRO$	:	Zero First stage ROcket motor

2.1 Introduction

ROBOOST is a ballistic simulation software developed in Matlab environment at the Alma Propulsion Laboratory of the University of Bologna in collaboration with Avio S.p.A. Its aim is the simulation of the combustion process and thrust production of solid propellant rockets. It relies on a 3D approach for the simulation of the burning surface regression process. Such surface is discretized with a 3D triangular mesh, whose motion is performed though the *off-setting* technique applied to each vertex of the grid. Therefore, the software can handle generic-shaped propellant geometries with anisotropies and inhomogeneities. Combustion chamber thermodynamic quantities are computed through a 1D unsteady fluid dynamics model, where the flow is assumed to be compressible. In addition to that, 0D unsteady model is available in the case of preliminary analysis. The burning rate is estimated starting from the classical Vieille law, and it is eventually corrected with the variations caused by propellant anisotropies. Furthermore, other models are integrated in ROBOOST in the interest of coupling together multiple phenomena affecting the thrust chamber internal dynamics, like the presence of the case-insulating thermal protection layer. Igniter and nozzle dynamics are considered.

2.2 Literature review

A variety of Computer Graphics procedures linked to solid rocket internal ballistic simulators have been proposed in literature to numerically compute combustion chamber thermodynamic parameters variation with thrust-time profile as the main goal. One example is represented by SPP (Solid Propellant rocket motor Performance computer program) [1]. This simulation software shows three available approaches (two-dimensional, axisymmetric and three dimensional) all of them based on boolean geometry methods. It consists of a combination or intersection of primitive solids (cones, spheres, prisms, cylinders, toruses) used to recreate the most common rocket propellant configurations (finocyl design, tapered star design, etc.). The same approach is used in PIBAL (Propulsion and Internal BAListic software) environment, developed by SNPE Propulsion [2]. It includes several grain macro functions each related to a specific 2D or 3D grain shape (axisymmetric dendred motor, wagon wheel, etc.). The abovementioned technique, although is effective in terms of computing surface and volume shapes, is unable to deal with inclusions and defects that can generate self-intersections during surface regression.

On the other hand, a recent technique to track the interface evolution is represented by the family of level-set methods, firstly introduced by Osher and Sethian [3]. According to the classical approach [4], the interface, namely a 2D\3D surface, is computed as the zero-contour of a higher dimensional function, i.e. the level-set function. From a geometrical point of view, the interface is computed as the intersection between a higher dimensional function (hyperbolic surface in Figure 3) and a plane identifying the zero-contour section.

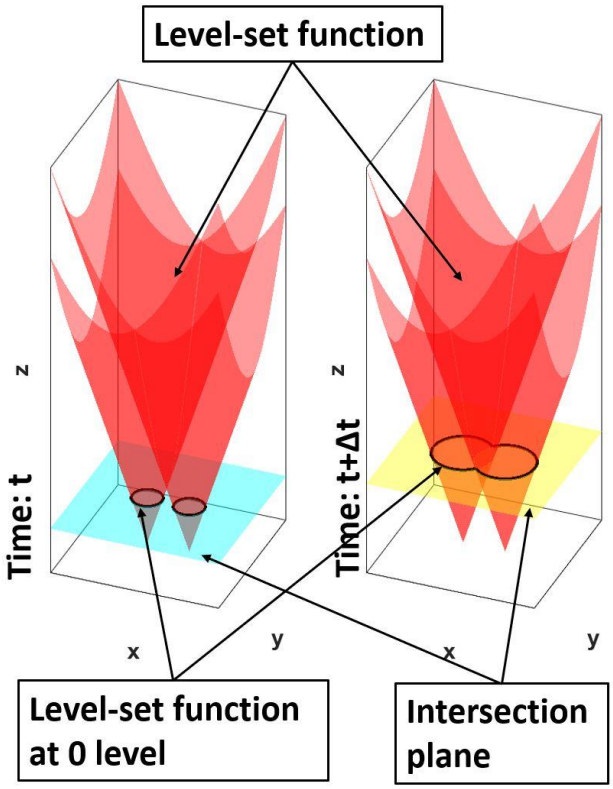

Figure 3: Level-set method.

The level-set function is usually defined as the Euclidian distance to the interface [4]. If a velocity field $\vec{v}(x, y, z)$ is introduced, then the level set function is deformed through a time variation and a spatial variation depending on the scalar product between $\vec{v}$ and the spatial gradient of the level-set function itself. The resulting initial value partial differential equation for the evolution of the level-set function is close to a Hamilton-Jacobi equation [3] and it is properly solved with respect to the hyperbolic conservation laws. Practically, level-set method implementation is equivalent to the numerical integration of level-set function partial derivatives in time and space. The main advantage of that method is an easy evaluation of surface curvature, normal and topology evolution. However, the section-by-section description used by level-set approach, make the velocity field to have some form of prevalent orientation.

Some improvements of level-set method have been addressed by Wilcox et al. [5, 6], by using an MDF (minimum distance function approach) in the software Rocballist. The minimum distance to the initial surface can be used to represent the detailed shape of the burning surface as it evolves in time: indeed, the MDF sign indicates whether the grid point is on the solid-or the gas-side of the interface. In contrast to the level-set method, there is no hyperbolic partial differential equation to be solved. Despite this method is efficient in terms of computational time, the main disadvantages are the inapplicability to radial and azimuthal burn rate variation (with respect to axial variation) and the function sign error due to the presence of sharp-angled cones pointing towards chamber volume: in practice sharp-angled cones could appear as inclusions within the grain itself. The use of a dynamic 3D triangular mesh as the core of the burning surface regression module in ROBOOST (ROcket BOOst Simulation Tool) performance estimation code, allows to reach the abovementioned target with little penalty of accuracy, due to the finite mesh discretization into triangular elements. A self-intersection removal procedure, based on triangle-triangle intersection can be used to preserve mesh coherence [7]: each triangular mesh element is meant to be a pure geometrical representation to let

the triangle vertices (nodes of the mesh) translating in the domain, simulating in that way the burning surface regression process.
The above-mentioned numerical procedure integrated in the ballistic simulator ROBOOST [8] is meant to overcome all those limitations, proposing a new effective approach in the direction of giving more detailed estimations of SRM burning surface regression, dealing with inclusions/non-conventional grain geometry configurations.

2.3 Code Overview

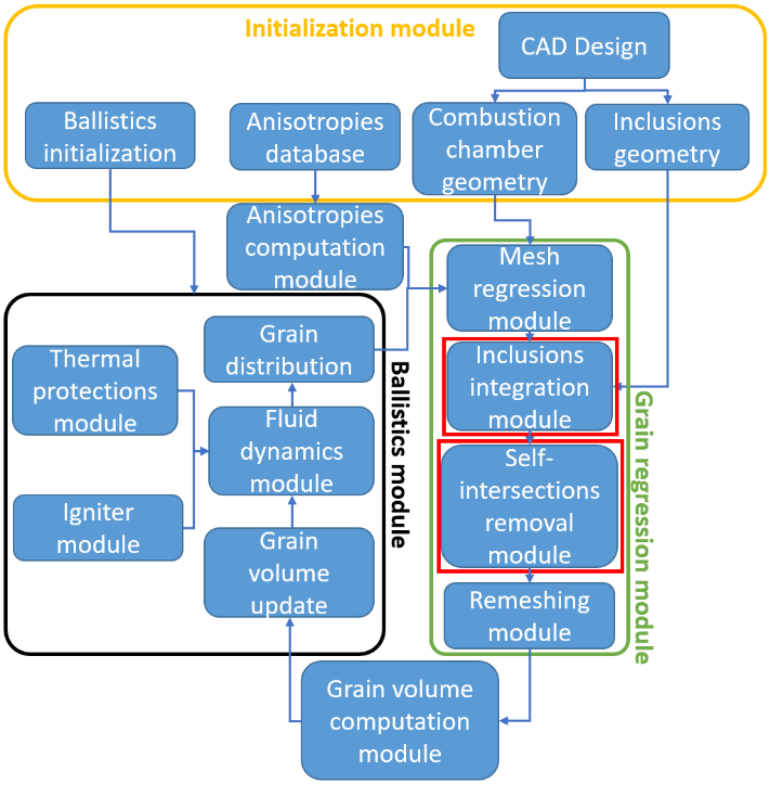

Figure 4: ROBOOST modules layout.

Figure 4 shows the modular structures of the code: each module is assigned to a specific function. The general approach is based on the burning surface regression which is modelled as a 3D triangular mesh (*Grain regression module* in Figure 4). The abovementioned strategy guarantees to ROBOOST the capability to handle generic geometric shapes (in terms of inclusions and propellant configurations): indeed, it can accept as an input, Iges format files.
Mesh nodes regression is obtained by adding along the normal direction of each node a displacement [15], whose amount is expressed by Eq. (1):

$$\Delta s_i = r_{b_i} \cdot \Delta t \tag{1}$$

$$r_{b_i} = F_{anis_i} \cdot a \cdot p_{0_i}^{n} \tag{2}$$

Because each node is managed independently from the others, point-by-point surface motion can be defined by introducing grain anisotropies as a burn rate variation table. This table can be included in the *Anisotropies computation module* (Figure 4) whose output is given in terms of a normalized factor F_{anis_i} (Eq. 2). It is identified by means of a 9 components tensor accounting the 3D anisotropy through the propellant. Each component let the software involve different grain properties according

to the material direction considered. That feature allows a more "physical" description of the surface regression process, especially in providing burn rate heterogeneities to the simulator. During simulations, since mesh triangular elements are indirectly deformed and compressed by displacements, a *Remeshing module* is needed in order to preserve mesh resolution and coherence (mesh should be two-manifold coherent) [7]. For instance, the increase of triangular elements dimension, during burning surface evolution, can produce overlapped triangles which must be removed to obtain a correct mesh evolution. *Remeshing module* includes procedures which preserve the domain length of single edges or triangle areas as well, maintaining them in the user-defined range by collapsing anomalous elements

The second fundamental block ROBOOST consists of, is the *Ballistics module*: it consists of a 1D unsteady fluid dynamics solved along the thrust chamber symmetry axis [7-9]. The main assumptions of the mathematical-physical model regarding the combustion chamber fluid-dynamics are the following ones:

1. One-dimensional flow along the motor axis.
2. All chemical reactions regarding both grain combustion and combustion chamber hot gas are neglected.
3. Solid propellant bounding the combustion chamber is assumed adiabatic.
4. Flow is considered compressible, subsonic, and inviscid.
5. Combustion chamber hot gas is considered as a *continuum*.
6. Combustion chamber hot gas obeys the perfect gas law

The model relies on the following equations:

$$\frac{\partial \rho}{\partial t} + \frac{\partial \rho u}{\partial x} = \frac{r_b P_b}{A_p} \rho_{PR} \tag{3}$$

$$\frac{\partial \rho u}{\partial t} + \frac{\partial}{\partial x}(\rho u^2 + p) = \frac{p}{A_p}\frac{\partial A_p}{\partial x} - \frac{r_b P_b}{A_p} \rho u \tag{4}$$

$$\frac{\partial}{\partial t}\left(\rho\left(c_v T + \frac{u^2}{2}\right)\right) + \frac{\partial}{\partial x}\left(u\left(\rho\left(c_v T + \frac{u^2}{2}\right) + p\right)\right) = \frac{r_b P_b}{A_p} \rho_{PR} H_f \tag{5}$$

$$p = \rho R T \tag{6}$$

Equations (3), (4) and (5) respectively represent mass balance, momentum balance and energy balance. More in detail, the right-hand side terms of the above-mentioned equations are the source terms linked to grain depletion. In fact, they are related to the burning rate (r_b), combustion chamber port area (A_p), burning perimeter (P_b), grain density (ρ_{PR}) and combustion enthalpy (H_f). Each of such quantities, except for the grain density which remains constant, evolves in time and space consistently with grain combustion process. On the other hand, Eq. (6) identifies the perfect gas law meaning that the gas produced by grain combustion behaves as an ideal, perfect gas. By numerically solving Eq.s (3) to (6), velocity and pressure fields of the flows are obtained with a low computational effort and a little penalty in time and space. The numerical approach involved regards a finite difference method based on a centered 2th order numerical scheme in space and a implicit Euler scheme in time.

Furthermore, *Ballistics module* includes the evaluation of combustion chamber temperature. It is performed starting from HTPB-based propellant thermochemical properties. By means of those properties, grain combustion reference temperature is obtained through NASA CEA (Chemical Equilibrium and Applications) program. Then, combustion chamber hot gases temperature is

estimated through the internal ballistics model linked to ROBOOST program. NASA CEA is also used to determine combustion chamber gas properties (specific heat at constant pressure, specific heat ration and molecular weight) at chemical equilibrium starting from grain chemical composition. *Grain regression module* is linked to the ballistics module in the following way: at a certain time interval $\Delta t = t - t_0$, first the regression module estimates the amount of burned propellant subtracting propellant volume at time t from propellant volume at time t_0. Then *Ballistics module* estimates thermodynamic parameters variation within the combustion chamber; new burning rate is computed starting from combustion chamber pressure by means of Eq.2. Finally, the new burning rate estimation is used to compute a new value of burned propellant in the *Grain regression module*: if the old burned grain volume is equal to the new burned grain volume less than a fixed tolerance, the code moves to the next time iteration, otherwise the abovementioned iterative procedure is repeated until convergence [7]. The overall process continues for each simulation time instant until the burn out time is achieved. Ballistics module, as shown in Figure 2, includes other two models: *Thermal protections module* and *Igniter module* [10]. The first estimates the thermal protections ablation phenomenon occurring close to the case and the nozzle throat section erosion, while the second evaluates the initial ignition transient phase, before the SRM is completely ignited, characterized by igniter behavior.

2.4 Results

ROBOOST software has been validated on ZEFIRO 23 (Z23) (Figure 5) This motor, produced by AVIO S.p.A. through the *filament-winding* manufacturing technique, represents the second stage of the European VEGA launcher. It is about 7.5 m long, with a maximum diameter of 1.9 m and a total grain mass of 24 tons [11]. The metallic case is filled with high density composite propellant consisting of aluminum powder (Al) as fuel, ammonium perchlorate (AP) as oxidizer and hydroxyl-terminated polybutadiene (HTPB) as plastic binder. It can produce and average thrust of 1122 kN with a specific impulse of 287.5s [11]. The internal bore has a variable cross section: a circular cylinder occurs in the fore and central part, close to the igniter; a finocyl shaped configuration takes place near the nozzle inlet.

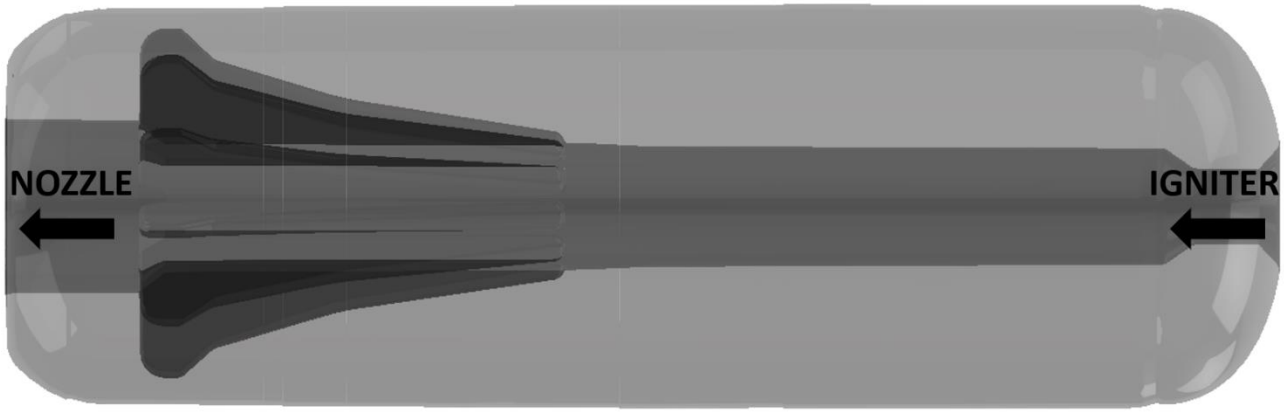

Figure 5: ZEFIRO 23, CAD geometry.

The complete motor geometry (Figure 5) has been generated through Catia CAD software. Then, Z23 configuration has been meshed through ROBOOST software (Figure 6). More in detail, a mesh of 120000 triangular faces with variable size edges has been obtained. The size ranges from a maximum resolution of 2 mm to a minimum resolution of 45 mm depending on the local surface curvature.

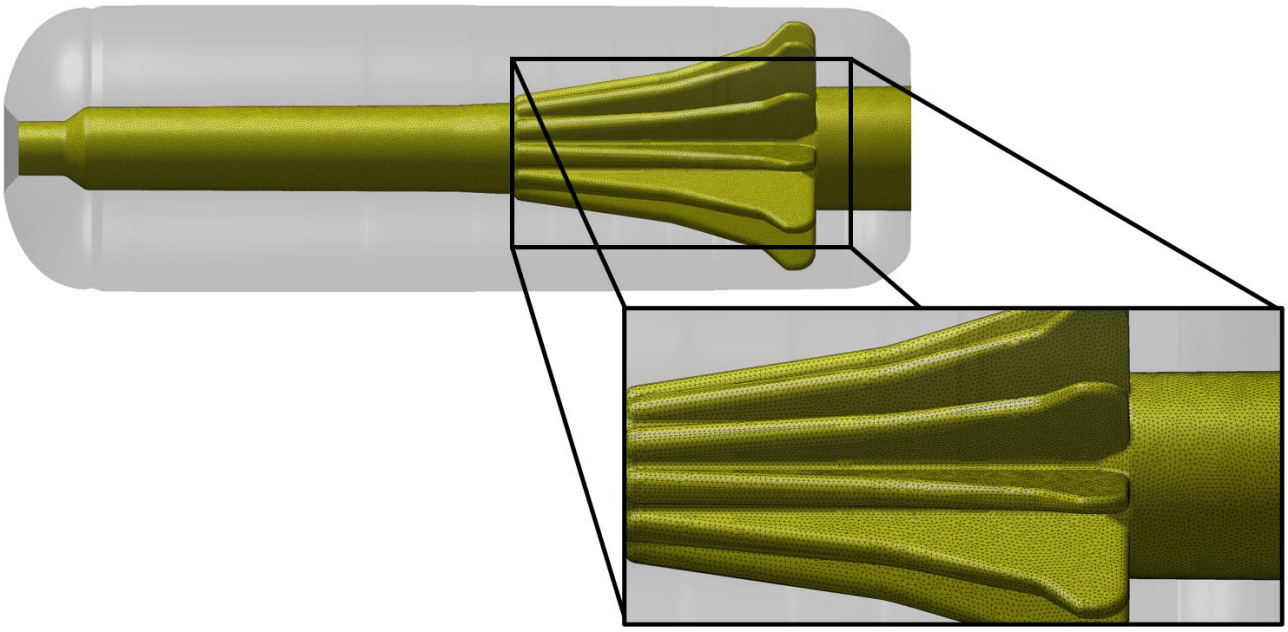

Figure 6: ZEFIRO 23, ROBOOST mesh.

Figure 7 displays burning surface evolution in time. More in detail, the yellow portion represents the burning surface. On the other hand, the green region is linked to the case-insulating thermal protection layers needed to insulate the metallic case from the combustion chamber hot gases. Percentual time is computed as the ratio between simulation dimensional time and the burn-out time when all propellant is depleted.

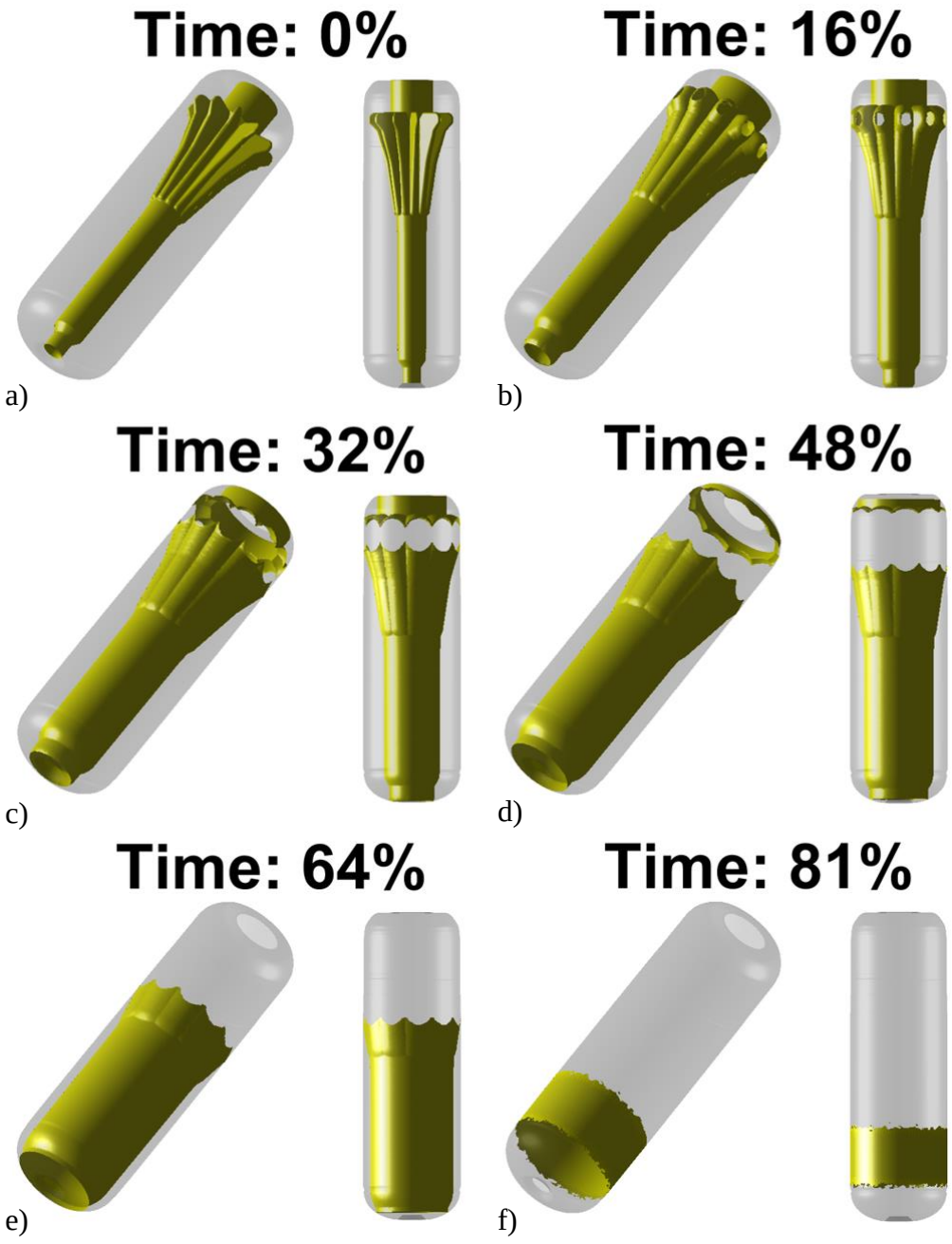

Figure 7: ZEFIRO 23 grain regression.

Since experimental data regarding the burning surface-time evolution is normally not available, the comparison between simulation and experimental data is performed through the thrust profile (Figure 8a). Experimental and simulation thrust curve are normalized with respect to a thrust reference value. As already mentioned, non-dimensional time is obtained considering the ratio with respect to the burn-out time. Finally, the thrust percentual error, defined as the instantaneous difference between the two curves, highlights how the developed three-dimensional software is close to actual data (Figure 8b). Specifically, the maximum error is about 2%: since the error trend in time is bounded in the range $\pm 2\%$, the simulation has been considered quite satisfactory. The isolated spikes in the first part of the simulation are due to the remeshing procedures and correspond to the time instant when the finocyl parts reach the casing wall. Therefore, future improvements will be focused on reducing such alteration effect in the direction of obtaining a more regular profile.

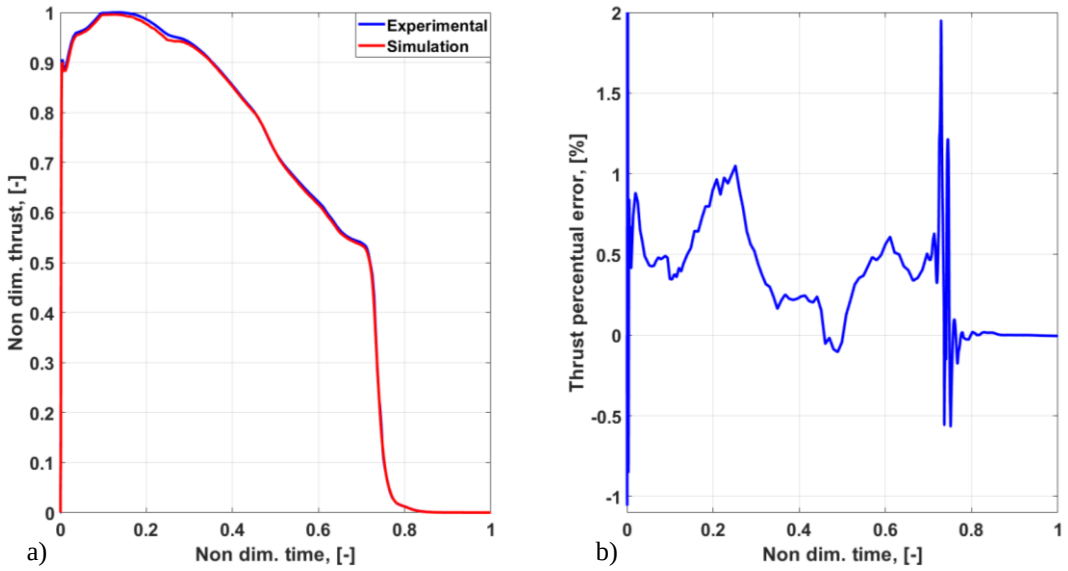

Figure 8: ZEFIRO 23 thrust comparison.

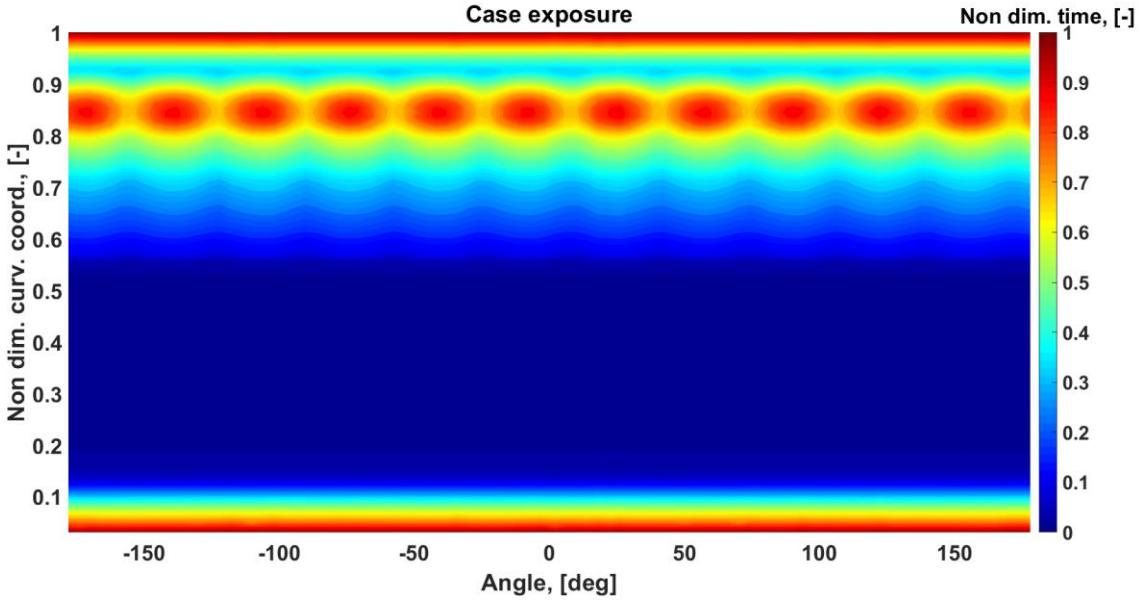

Figure 9: ZEFIRO 23 thermal protections exposure.

Figure 9 identifies case-insulating thermal protection exposure to combustion chamber hot gases. The angle identifies the azimuthal coordinate along the circumferential direction around the motor symmetry axis. The curvilinear coordinate determines the position along the case profile, starting from the igniter side of Z23. More in detail, such curvilinear coordinate is normalized in Figure 9 with its maximum value reached at the nozzle side. Finally, non-dimensional exposure time is obtained dividing each time instant with respect to the maximum exposure time.

Eleven circular shaped red zones occur linked to the eleven lobes of the finocyl propellant geometry. In fact, each lobe early approaches the case meaning that the thermal protection material is subjected to a protracted exposure to grain combustion gases (Figure 7b). On the contrary, the blue region, ranging from about 0.2 to 0.6 with respect to the non-dimensional curvilinear coordinate, shows the zone where the burning surface reaches the case at the same time instant. Indeed, no exposure time

difference takes place in the above-mentioned region, implying that the burning surface is parallel to the case.

2.5 Conclusions

A 3D software, namely ROBOOST, has been presented. This code is able to simulate the burning surface regression process, where the burning surface is discretized as 3D dynamic triangular mesh. That feature allows the program to deal with a large variety of propellant geometry configuration. Furthermore, surface displacement is applied to each mesh vertex implying independent vertex motion. Hence, propellant anisotropies can be analyzed since each vertex is handled separately from the others. On the other hand, combustion chamber fluid dynamics is modelled through a 1D unsteady approach. This solution guarantees the possibility to investigate both thrust transients (ignition transient and tail-off) and quasi-steady state phase. Subsequently, ROBOOST has been applied to ZEFIRO 23 and the thrust result has been compared with experimental data. The relative percentage error between the two curves oscillates in the range $\pm 2\%$, thus the simulation is considered quite satisfactory. Finally, case-insulating thermal protection material exposure map has been considered: eleven zones highly exposed occur due to the star lobes linked to the SRM finocyl configuration.

References

[1] Dunn, S., S., and Coats, D., E., "3-D Grain Design and Ballistic Analysis using the SPP97 Code", AIAA Paper 1997-3340, July 1997.
https://doi.org/10.2514/6.1997-3340

[2] Dauch, F., and Ribéreau, D., "A Software for SRM Grain Design and Internal Ballistics Evaluation, PIBAL (Propulsion and Internal Ballistics)", AIAA Paper 2002-4299, July 2002.
https://doi.org/10.2514/6.2002-4299

[3] Osher, S., and Sethian, J., A., "Fronts propagating with curvature-dependent speed: Algorithms based on Hamilton-Jacobi formulations", Journal of Computational Physics, vol. 79, n. 1, 1988, pp. 12-49.
https://doi.org/10.1016/0021-9991(88)90002-2

[4] Gibou, F., Fedkiw, R., and Osher, S., "A review of level-set methods and some recent applications", Journal of Computational Physics, vol. 353, n. 15, 2018, pp. 82-109.
https://doi.org/10.1016/j.jcp.2017.10.006

[5] Willcox, M., A., Brewster, M., Q., Tang, K., C., Stewart, D., S., and Kuznetsov, I., "Solid Rocket Motor Internal Ballistics Simulation Using Three-Dimensional Grain Burnback", Journal of Propulsion and Power, vol. 23, n. 3, 2007, pp. 575-584.
https://doi.org/10.2514/1.22971

[6] Willcox, M., A., Brewster, M., Q., Tang, K., C., and Stewart, D., S., "Solid Propellant Grain Design and Burnback Simulation Using a Minimum Distance Function", Journal of Propulsion and Power, vol. 23, n. 2, 2007, pp. 465-475.
https://doi.org/10.2514/1.22937

[7] Bertacin, R., Ponti, F., Corti, E., Fedele, D., and Annovazzi, A., "Numerical Simulation of the Zefiro 9 Performance Using a New Dynamic SRM Ballistic Simulator", AIAA Paper 2013-4174, July 2013.
https://doi.org/10.2514/6.2013-4174

[8] Bertacin, R., Ponti, F., and Annovazzi, A., "A New Three-Dimensional Ballistic Model for Solid Rocket Motor Non-Homogeneous Combustion", AIAA Paper 2012-3974, August 2012.
https://doi.org/10.2514/6.2012-3974

[9] Ponti, F., Souhair, N., Mini, S., and Annovazzi, A., “0D Unsteady - 1D Quasi-Stationary Internal Ballistic coupling for ROBOOST simulation tool,” AIAA Paper 2019-4140, August 2019.
https://doi.org/10.2514/6.2019-4140

[10] Ponti, F., Mini, S., and Annovazzi, A., “Parametric Study on Solid Rocket Motor Ignition Transient Prediction using ROBOOST simulation tool”, AIDAA XXV International Conference, September 2019.

[11] https://www.avio.com/it/vega

Chapter 3

3 Influence of inclusions and debondings within the grain

Nomenclature

Latin

$a(x_c)$ = case profile height function, $[m]$
ds = infinitesimal length, $[m]$
e_{az} = unit vector defining the orthonormal basis $(e_{x_c}, e_{az}, e_{x_n})$
e_x = unit vector defining the orthonormal basis (e_x, e_y, e_z)
e_{x_c} = unit vector defining the orthonormal basis $(e_{x_c}, e_{az}, e_{x_n})$
e_{x_n} = unit vector defining the orthonormal basis $(e_{x_c}, e_{az}, e_{x_n})$
e_y = unit vector defining the orthonormal basis (e_x, e_y, e_z)
e_z = unit vector defining the orthonormal basis (e_x, e_y, e_z) and $(e_\rho, e_\vartheta, e_z)$
e_ϑ = unit vector defining the orthonormal basis $(e_\rho, e_\vartheta, e_z)$
e_ρ = unit vector defining the orthonormal basis $(e_\rho, e_\vartheta, e_z)$
h_j = Lamè coefficients
$\hat{h}_j$ = unit vector regarding Lamè coefficients
$\vec{h}_j$ = vector regarding Lamè coefficients
L_{az} = debonding size along e_{az}, $[m]$
L_{x_c} = debonding size along e_{x_c}, $[m]$
L_{x_n} = debonding size along e_{x_n}, $[m]$
$\hat{n}$ = unit vector normal to the case surface
$\hat{n}_x$ = x-axis component of the unit vector normal to the case surface
$\hat{n}_y$ = y-axis component of the unit vector normal to the case surface
$\hat{n}_z$ = z-axis component of the unit vector normal to the case surface
$\vec{r}$ = position vector
w_1 = general curvilinear coordinate
w_2 = general curvilinear coordinate
w_3 = general curvilinear coordinate
x = coordinate of the orthonormal basis defined by e_x, e_y, and e_z
x_{az} = coordinate of the orthonormal basis defined by e_{x_c}, e_{az}, and e_{x_n}, $[m]$
$x_{az_{max}}$ = maximum exposure map extension along e_{az}, $[m]$
$x_{az_{min}}$ = minimum exposure map extension along e_{az}, $[m]$
x_c = coordinate of the orthonormal basis defined by e_{x_c}, e_{az}, and e_{x_n}, $[m]$
$x_{c_{max}}$ = maximum exposure map extension along e_{x_c}, $[m]$
$x_{c_{min}}$ = minimum exposure map extension along e_{x_c}, $[m]$
$x_{c_{0'}}$ = coordinate x_c computed at local reference frame origin, namely 0', $[m]$
y = coordinate of the orthonormal basis defined by e_x, e_y, and e_z

z = coordinate of the orthonormal basis defined by e_x, e_y, and e_z

Greek

α = coefficient of the line equation linked to the case envelope discretization
β = coefficient of the line equation linked to the case envelope discretization
ρ = coordinate of the orthonormal basis defined by e_ρ, e_ϑ, and e_z
ρ_* = radial position of the local reference frame origin expressed in global reference frame cylindrical coordinates, $[m]$
$\rho(x_c)$ = case profile radius function, $[m]$
ϕ = exposure map regarding the case-insulating thermal protection material, $[m]$
φ = generic scalar value

Acronyms

$ROBOOST$ = ROcket BOOst Simulation Tool
SRM = Solid Rocket Motor
$ZEFIRO\ 9$ = Zero First stage ROcket

3.1 Introduction

The physical integrity of a solid propellant grain is the major factor in affecting internal ballistics performance. Imperfections, such as cracks, inclusions, or the existence of extra uninhibited propellant surface usually causes changes in the desired internal ballistics. Specifically, the present work considers the influence of inclusions and debondings.
Inclusions are usually voids characterized by different shapes, appearing in the grain as the result of the propellant casting process. More in detail, air could remain trapped within the grain due to its high viscosity and high density, causing the porosity in the grain itself. On the other hand, debondings are essentially cavities produced by the separation between the propellant and the liner. In facts, in solid rocket motors, the interface region between the metallic case and the solid grain consists of various layers (Figure 10).

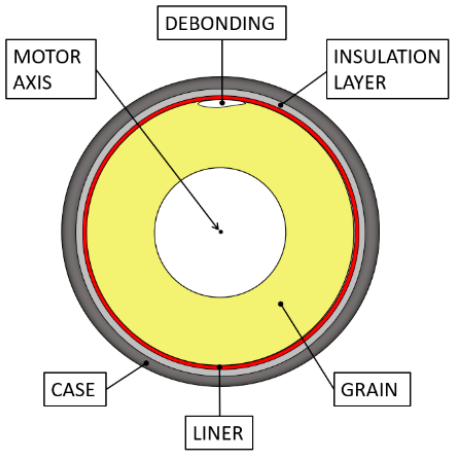

Figure 10: Propellant debonding conceptual scheme.

First, an insulation layer is used next to the case as a thermal coating [1] in order to protect it from the high amount of thermal power released by grain combustion. Then, thin adhesive layer, known as liner, bonds together both the solid propellant and the thermal insulation. The last layer, much thicker than the previous ones, is represented by pure solid propellant. The strength of interface region

is substantially dependent on stresses and strains accumulation: indeed, one of its fundamental requirements is to withstand thermal and pressure loadings occurring during the phases before launch, from manufacturing process to transportation [2]. However, if these kinds of stresses exceed the bond strength of the interface materials, a fracture may arise through the liner [3]. Hence, the propellant may separate from the insulation layer: this phenomenon is named debonding [4]. Inclusions and debondings areas are usually critical regions for at least two reasons. First, during combustion, the inclusion\debonding tip may become unstable and propagate causing a not negligible increase of combustion chamber pressure. It is important to highlight that the inclusion\debonding region contributes additional surface area for burning [5]. If the pressure becomes higher than the design pressure, it can cause mechanical deformation and further defect growth. Moreover, debonding dilatation and propagation could be enhanced by case deflection. It has been proven that the debonding velocity with case expansion is higher than that without significant case deflection itself [6]. When the burning surface approaches cavities/debondings during the combustion, the flame propagation spreads within the void region with a higher burning rate [7], thus causing a not negligible increase in burning surface advancement toward the case. The possible consequences are essentially the following ones. First, a significative burning surface regression implies a pressure increment due to the larger amount of propellant burnt. Second, a sooner exposure of the case-insulating thermal protections to the combustion chamber high-temperature gases could arise. Specifically, the inhibited area could offer a path for hot gases to prematurely attack thermal insulation layer. The thermal protection layer is usually designed to withstand a certain amount of power produced by the propellant combustion for a certain time interval. More deeply, the main parameter is the thickness of thermal protection material. If the thickness is not large enough to absorb all the hot gases convective and radiative power, the metallic case is not insulated anymore [8]. The final consequence could even be the launcher failure. Therefore, in order to ensure the proper functioning of the launcher, the cavities/debondings evolution during combustion is conveniently addressed and explained using advanced computer graphic techniques.

3.2 Cavities/debondings integration procedure

Let the main mesh be the burning surface without any kind of inclusions at a certain temporal iteration. Cavities/debondings integration algorithm (Figure 11) essentially consists in verifying if intersections occur between the main mesh and each cavity/debonding mesh (*self-intersections removal algorithm*).

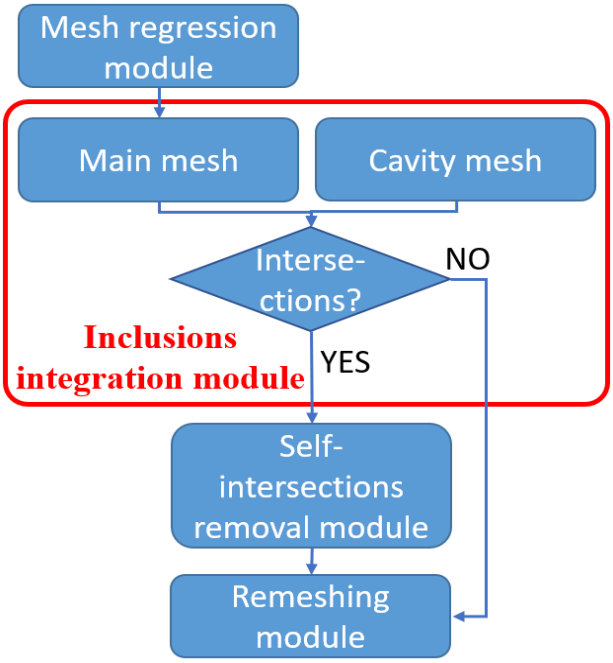

Figure 11: Cavities/debondings integration flowchart.

If there is at least one intersection point, meaning that the propellant has a common region with the cavity volume, then the cavity is included using the Self-intersections removal module explained before. On the contrary, if no intersection is found the main mesh remains unaltered: the burning surface has not approached the cavity/debonding surface yet. The previous procedure runs for each cavity/debonding: indeed, ROBOOST can handle a generic number of cavities with generic shapes. Furthermore, in order to facilitate cavity/debonding integration in the burning surface mesh, a local mesh refinement procedure is performed before cavity sticking (Figure 12): indeed, intersection points between cavity and burning surface mesh are more accurately identified if triangles are of the same size.

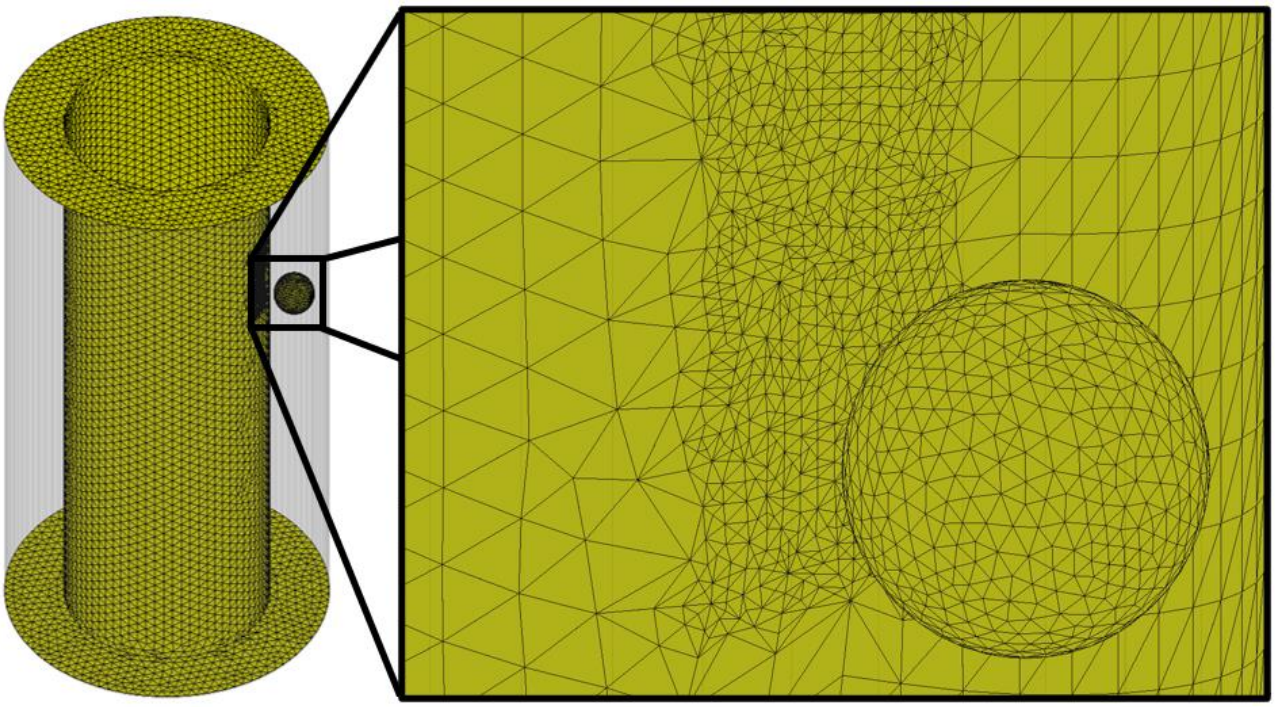

Figure 12: Local mesh refinement.

3.2.1 Self-intersections removal algorithm

The self-intersection removal algorithm (Figure 13) basic approach is outlined in [9]. First, mesh nodes are displaced along their normal direction according to the local burning rate (*Raw offset triangular mesh* block). Second, low-quality aspect ratio triangles are removed in the direction of avoiding numerical instabilities (*Remove degenerate triangles* block). Re-meshing procedures allow to reach such target. Third, triangles self-intersection points are computed through geometrical primitive-primitive intersection functions using the Moller algorithm [10]. To speed up the self-intersection identification process, the mesh is partitioned into subsets using an Axis-Aligned Bounding Box (AABB) procedure. Figure 14 shows an intersection between an elliptical inclusion (within the red circle Figure 14) and an example solid rocket motor burning surface (yellow triangular mesh). Moreover, the yellow surface (Figure 14) represents the valid region domain: it includes the set of triangles defining the outer boundary of the offset volume from the raw offset triangular mesh. On the other hand, the invalid region (red surface in Figure 14) is the zone occurring due to self-intersections formation which must be removed.

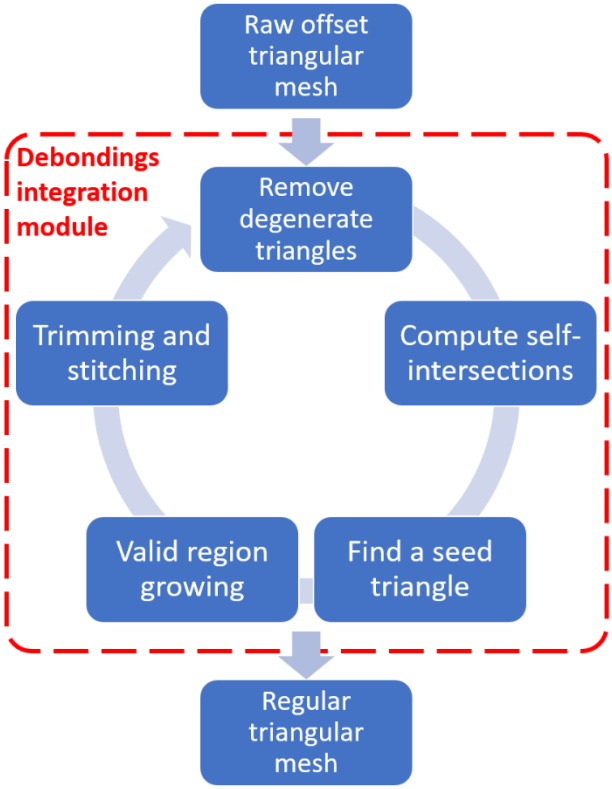

Figure 13: Self-intersection removal algorithm flowchart.

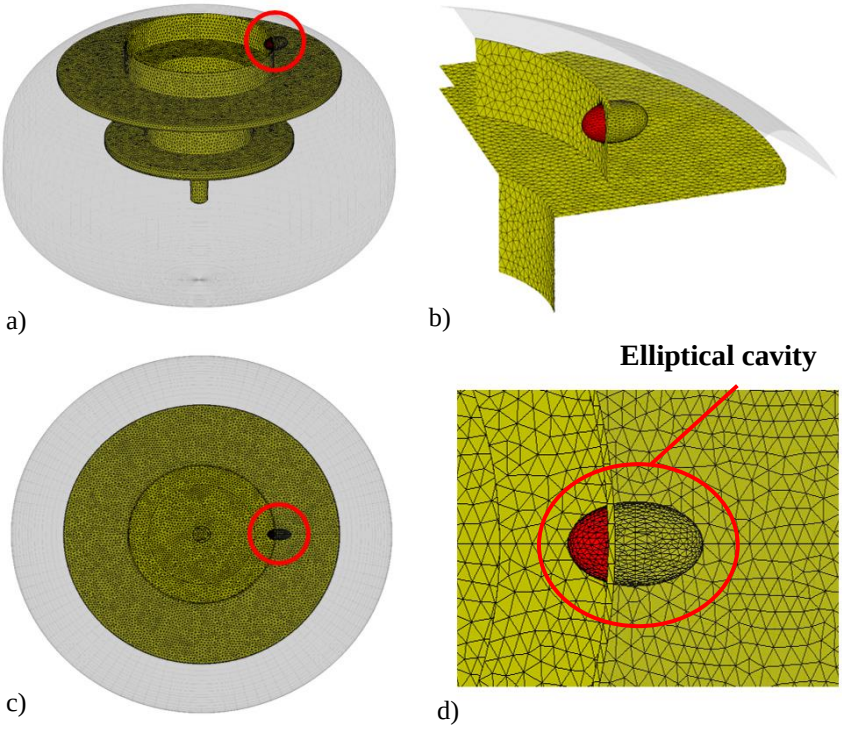

Figure 14: Cavity intersection with burning surface.

Subsequently, once the triangle-triangle intersections have been computed, the triangular mesh is classified into three subsets of triangles (Figure 15):

- *valid triangles:* triangles entirely contained in the valid region. Those triangles represent the physical grain burning surface.
- *Partially valid triangles:* those triangles lie on the boundary between the valid and the invalid region. Each triangle consists of a valid and invalid portion divided by the intersection line (line LMN in Figure 15).
- *Invalid triangles:* those triangles belong to the invalid region.

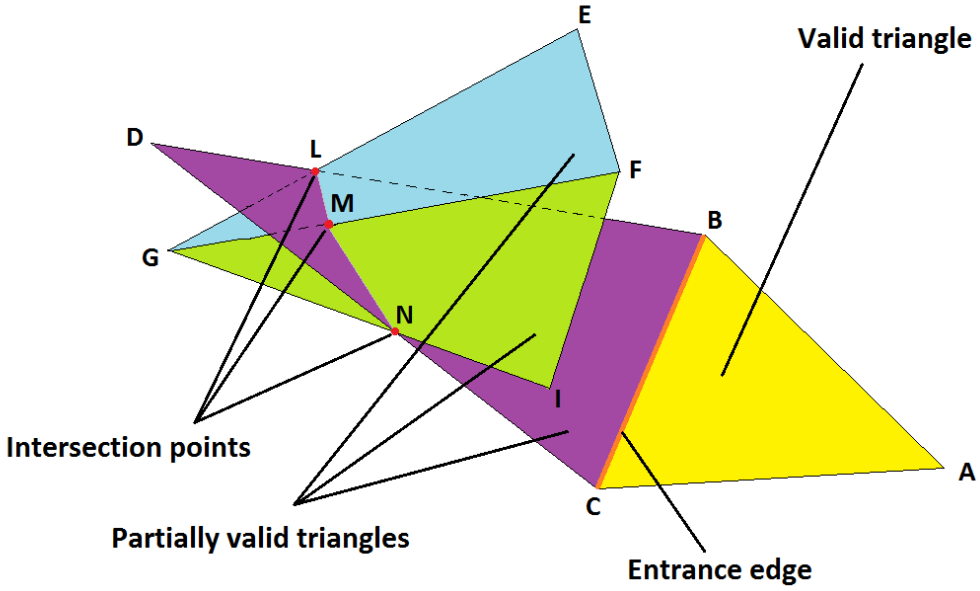

Figure 15: Mesh triangle subsets.

Valid triangles are identified by a growing region algorithm that requires an initial valid triangle (*seed triangle*). A seed triangle resides in the set of triangles all having the three vertices on the convex hull of the triangular mesh. A seed triangle is exclusively chosen as a growing region starting triangle since it is always included in the valid triangle set. Figure 5 shows the valid region expansion process: valid region propagation is performed until it reaches partially valid triangles, and therefore mesh self-intersection line (red line in Figure 16).

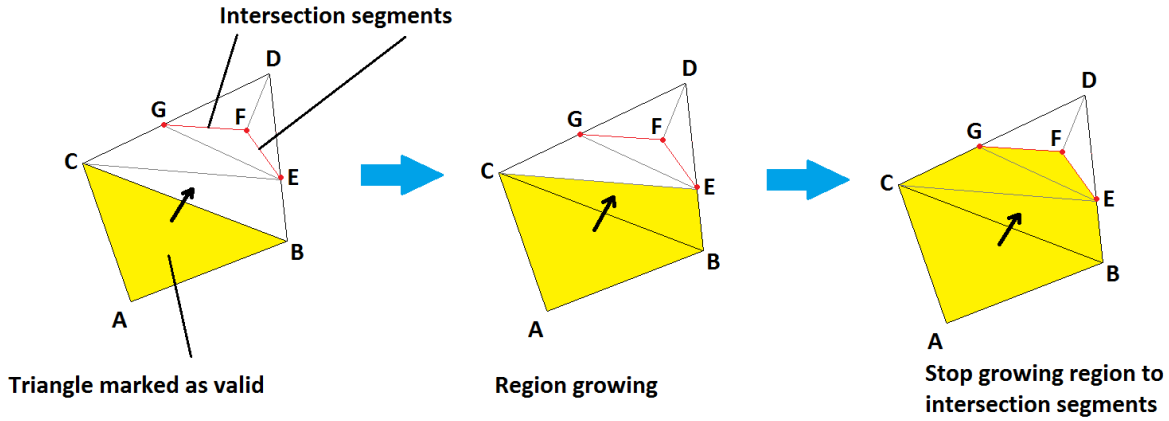

Figure 16: Growing region expansion process.

The core of the growing region algorithm is the capability to cross over the self-intersection and to move to the sub-triangles of the counterpart triangle (partially valid triangle having a common edge with the partially valid triangle which the growing region expands from). This process is identified as *crossing-the-river* method and allows to explore an unvisited region of the mesh. More in detail, in Figure 6, *crossing-the-river* procedure allows to propagate the growing region from the valid part (a) of a partially valid triangle T_p to the valid part of its counterpart, namely T_c.

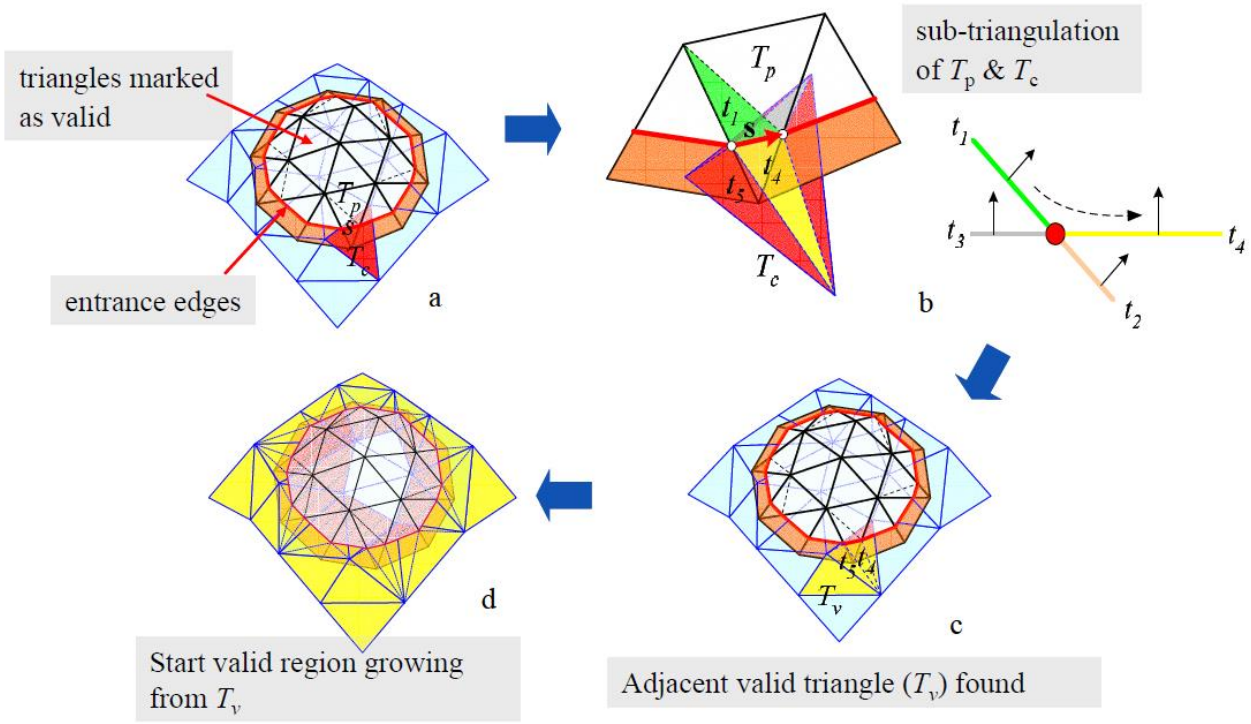

Figure 17: Crossing-the-river procedure [9].

Steps shown in Figure 17 are the following:

- Triangles belonging to valid region (the white region in the figure) are marked as valid; on the other hand, near the boundary (orange region) there is a partially valid triangle T_p and its counterpart T_c (red triangle in Figure 17b). The problem consists of moving from T_p to T_c crossing the red entrance edge.
- After the sub-triangulation of both T_p and T_c ,valid growing region propagates from t_1(sub-triangle of T_p) to t_4(sub-triangle of T_c) by means of a criterion based on triangle normals discussed later (Figure 17b)
- Therefore, a new valid triangle T_v is found becoming the *seed triangle* for the unvisited region (Figure 17c).
- Valid region propagates starting from T_v. The yellow region becomes a part of the valid region itself (Figure 17d). It is important to notice that self-intersections do no longer exist since the triangles not satisfying crossing the river criterion are removed (like t_2 andt_3 shown by Figure 17b).

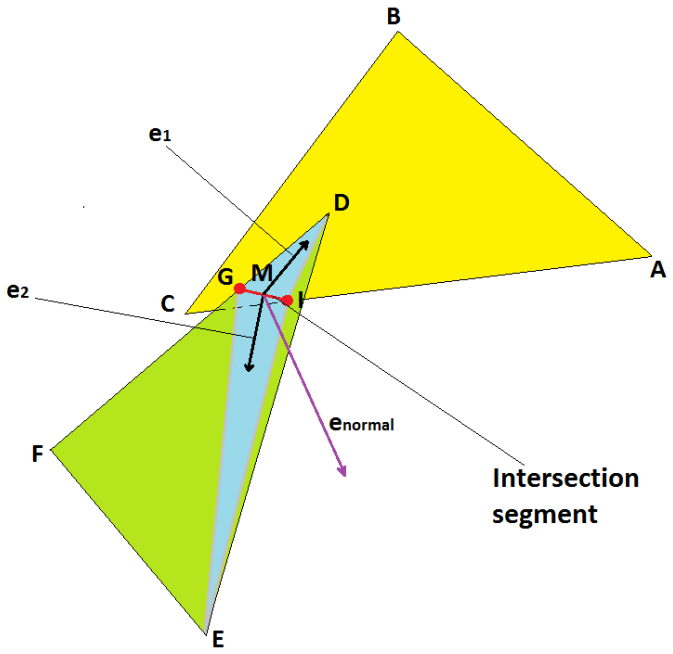

Figure 18: Crossing-the-river criterion.

Figure 18 displays the *crossing-the-river* criterion: ABC is a partially valid triangle (T_p), DEF is its counterpart (T_c). DGI and GIE are t_1 and t_2 (triangles belonging to the sub-triangulation). M is the mean point of the intersection segment defined by the points G and I. More in detail, the previously mentioned criterion is based on the following passages:

- Consider a partially valid triangle T_p, its counterpart triangle T_c and their sub-triangulations.
- Compute the counterpart normal (e_{normal}) that is a unit vector passing through the mean point of the intersection segment and perpendicular to the plane which T_c belongs to.
- Consider the two sub-triangles (t_1 and t_2) of T_c adiacent to the intersection segment. Then compute the two unit vectors (e_1 and e_2) on T_c plane corresponding to t_1 and t_2:
  - pointing outwards with respect to the intersection segments;
  - passing through the mean point of the intersection segment.
- Evaluate the scalar product betweene_{normal} and each of e_1 and e_2.
- Select between t_1 and t_2 the one for which the scalar product estimated at the previous 3 is negative. In Figure 4.13 the chosen sub-triangle is t_1.

Finally, with the aim of testing the reliability and robustness of the self-intersection removal algorithm in challenging conditions, two SRM test geometries were designed.
The first test geometry (Figure 19a) is about 1 meter long, with a maximum case diameter of 0.8 meters. Its main characteristics are related to its central bore: it consists of four tubular shapes, each with an average diameter of 0.1 meters and a depth of 0.4 meters. As in previous examples, the motor solid geometry has been generated using SolidWorks CAD software and the mesh with Gmsh software [11]. The generated mesh consists of 32500 triangles defined with 16400 mesh nodes with a variable resolution in the range of 1÷10 millimeters. This simulation represents an example of the effectiveness and robustness of the self-intersection removal algorithm used: indeed, this geometry reveals many self-intersecting triangles located close to the intersection region of the four tubular structures (red regions in Figure 19c)

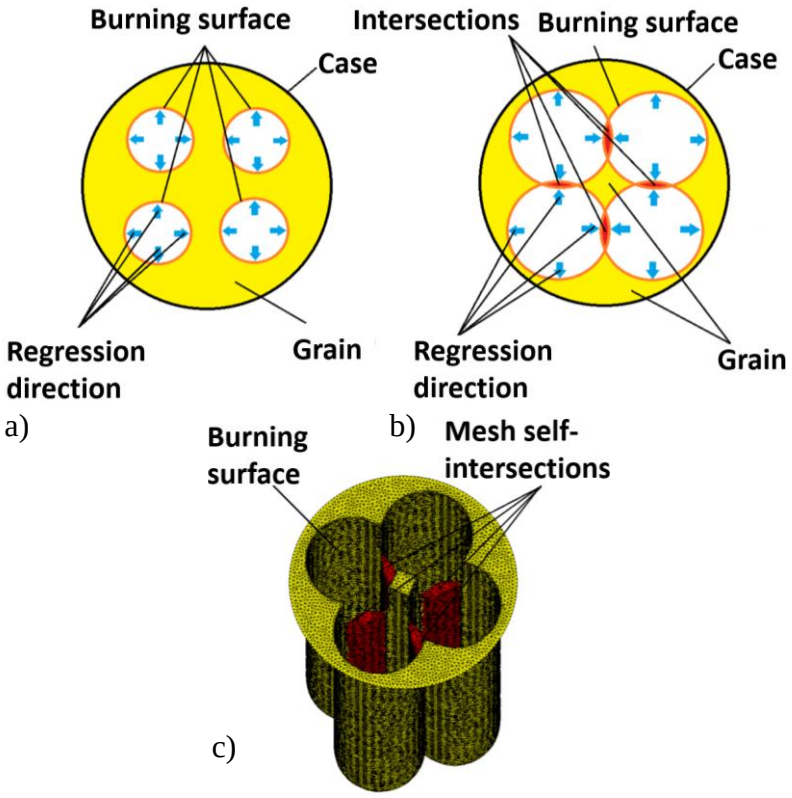

Figure 19: Self-intersections generation in multi-perforated grain.

Figure 20 shows the spatial evolution of the burning surface in its time regression process. More precisely all self-intersections are removed with the abovementioned algorithm in the time range between Figure 20b and Figure 20c.

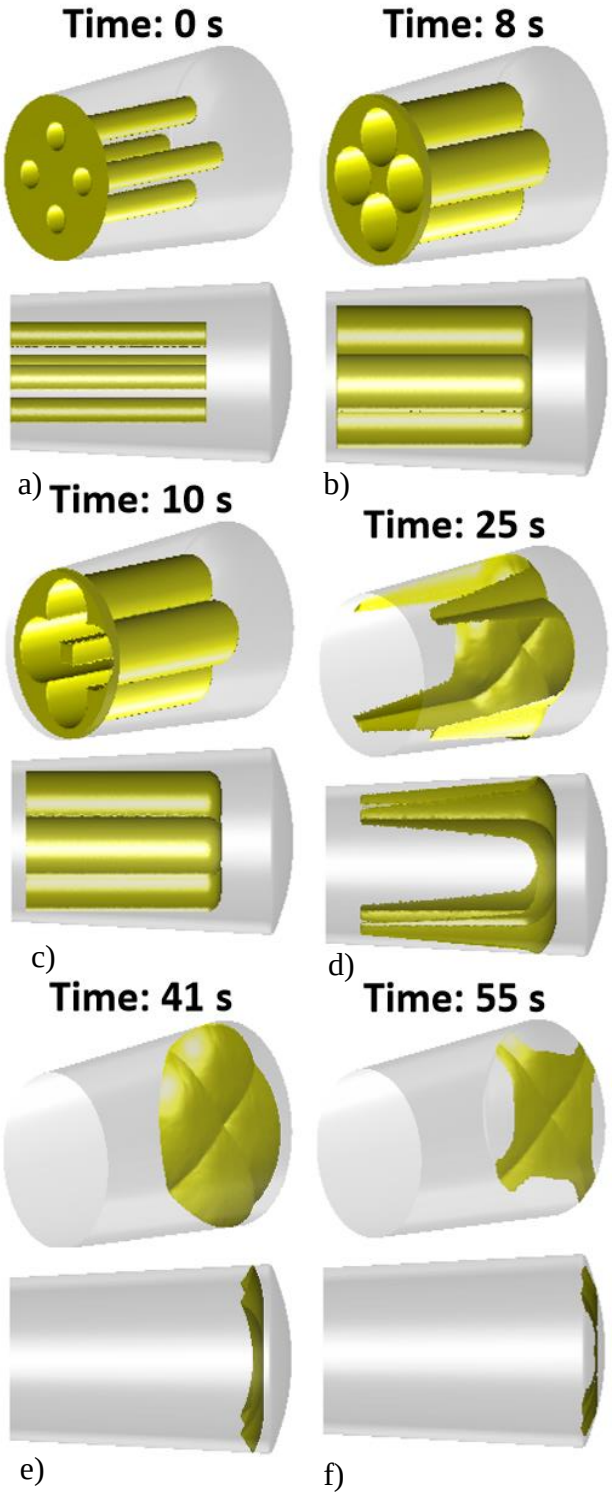

Figure 20: Burning surface regression in a multi-perforated SRM.

That step is needed in order to correctly estimate geometrical parameters time evolution (Figure 21). In fact, the self-intersections occurrence results in an erroneous burning surface increment (Figure 21a) due to the arising of the red intersecting regions (Figure 19) which leads to a wrong volume-time slope increment as well (Figure 21b).

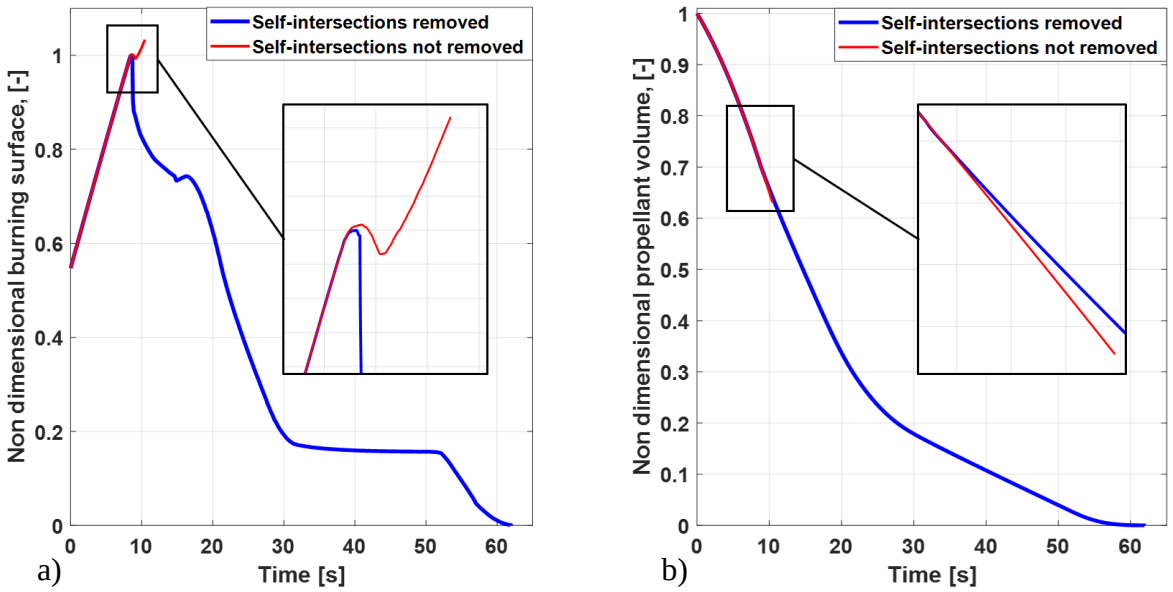

Figure 21: Burning surface and propellant volume evolution regarding multi-perforated SRM.

Furthermore, another interesting result is the internal case exposure map evaluated at the end of combustion (Figure 22). Exposure map is conveniently expressed in length units instead of time units, where the length is identified by the amount of web. Notably, the web parameter at a specified time is obtained computing the integral of the burning rate-time profile up to the time instant of interest. Thus, the web represents the distance displayed by the burning surface from its initial position and the case itself.

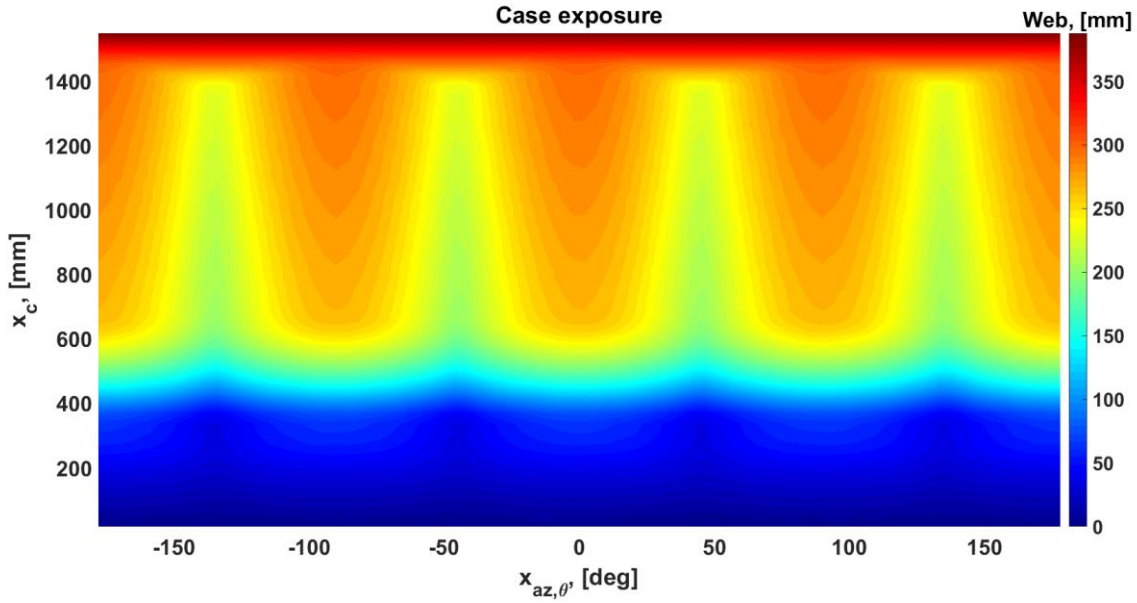

Figure 22: Multi-perforated SRM thermal protection exposure.

The blue zone can be linked to an end-burn combustion type which takes place during the last time instants (Figure 20e-f). Four orange-to-yellow regions can be identified near the 2D map horizontal center line: these are related to the propellant tubular structures intersecting each other (Figure 20c-d) which approach the case earlier than the other part of the burning surface.

The second geometry consists of cross shape propellant configuration where the four lobes are aimed to merge during burning surface evolution.

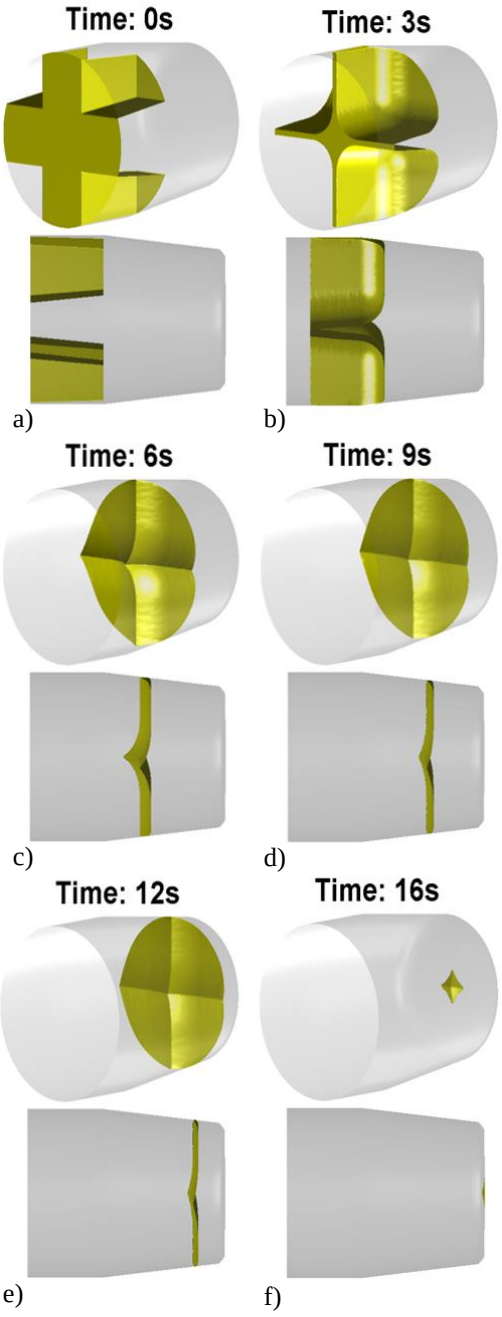

Figure 23: Burning surface regression in a cross shaped SRM.

The generated mesh consists of 108200 triangles defined with 54640 mesh nodes with a variable resolution in the range of 0.3÷2 millimeters. Figure 23 shows the time evolution of the burning surface. When the four lobes consume the central cross of propellant, the invalid region arises (red triangles showed in Figure 24). In a similar for the previously discussed geometry, if the self-intersections were not removed, the burning surface area would rapidly increase (red line in Figure 25a) diverging from the true solution (blue line in Figure 25a), while the propellant volume (red line

in Figure 25b) decreases faster than the correct trend (blue line in Figure 25b). These effects would influence the burning surface regression rate leading to a wrong simulation. Therefore, it is crucial to ensure the detection and the removal of the self-intersections.

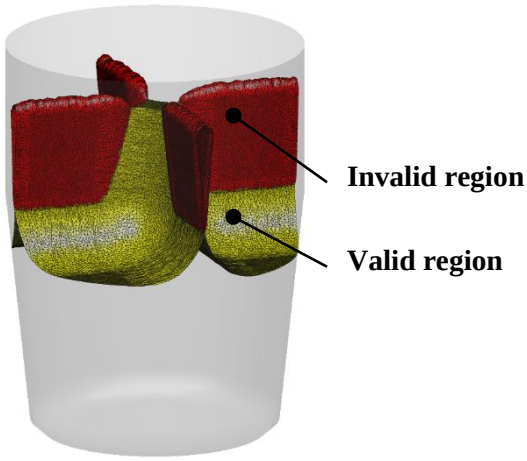

Figure 24: Valid/invalid triangle region.

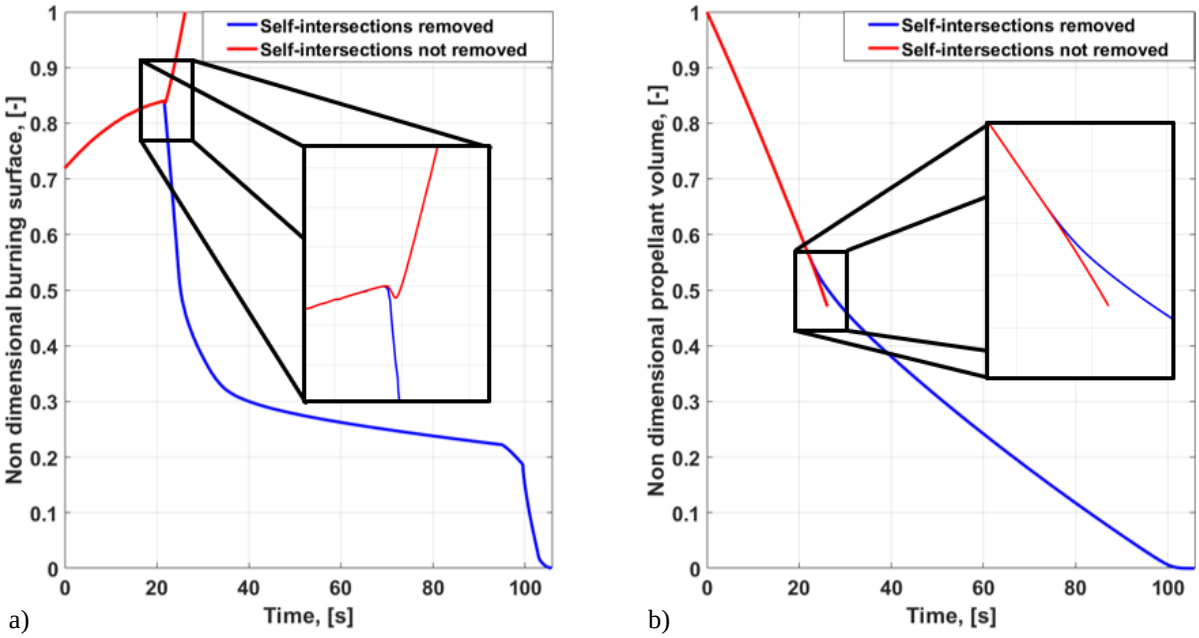

Figure 25: Burning surface and propellant volume evolution regarding cross shaped SRM

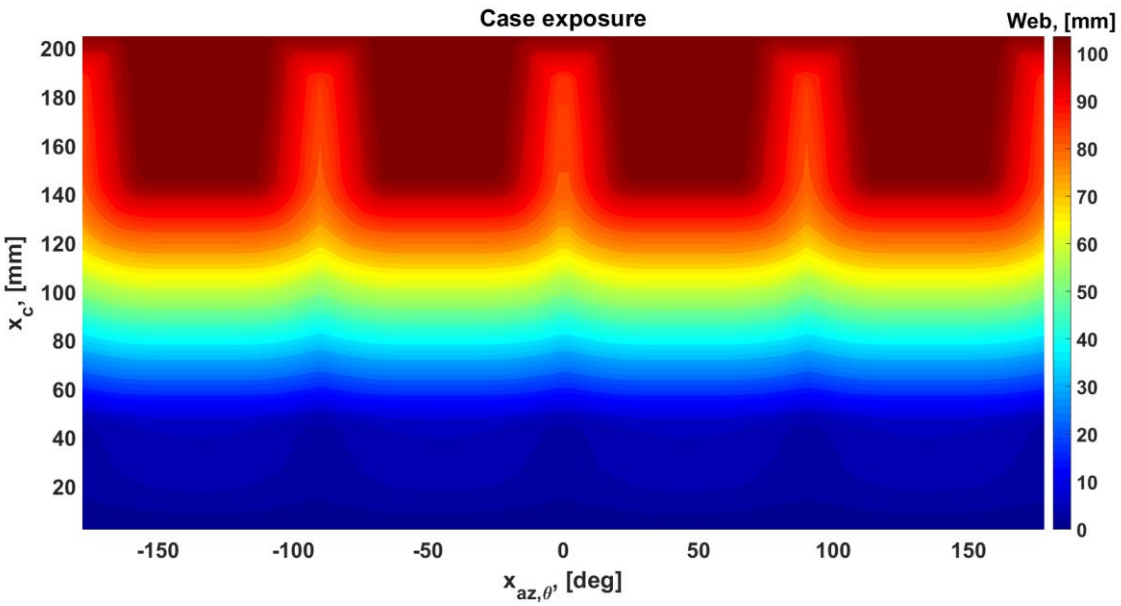

Figure 26: Cross shape SRM thermal protection exposure

Figure 26 is linked to the thermal exposure map, where the contour map displays how long the thermal protection material have been exposed to the combustion chamber hot gases.

3.3 Debondings map generation method

The aim of the present study is the identification of the debondings impact on case-insulating thermal exposure by varying the position and the size of the debonding on the case surface, through a novel method. The first step consists of determining the thermal protection exposure map by using ROBOOST software. Since, as highlighted in the previous paragraph, it relies on a 3D representation of the burning surface discretized with a triangular mesh, there is the possibility to track the burning surface vertex position on the SRM case at each simulation iteration.

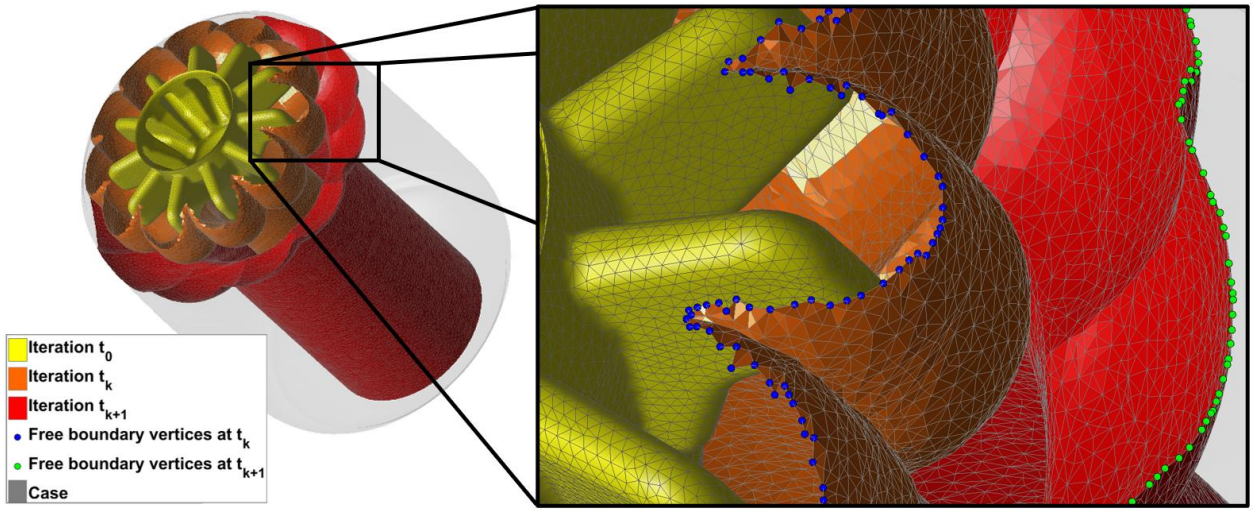

Figure 27: Mesh free boundary vertices.

More in detail, burning surface vertices laying on the case are the points belonging to the free boundary triangular facets (i.e., mesh edges) of the mesh itself. A facet in the triangulation is on the free boundary if it is referenced by only one triangle, implying that the set of free boundary facets vertices coincides with the set of the outer edges of the 3D triangulation. Figure 27 shows at different ROBOOST iterations, namely t_k and t_{k+1}, mesh free boundary points moving from the blue positions to the new positions represented by green dots. This occurs at the same time of burning surface mesh recession meaning that each vertex is uniquely linked with both a specific position on the case surface and a specific time instant. The software collects the previously mentioned parameters for each mesh vertex at every simulation time. Therefore, surface points which approaches earlier the case are associated with a larger exposure time since the case region at the same position of those points is no longer inhibited due to the local complete depletion of the grain. On the contrary, if case regions are exposed to combustion chamber hot gases later (surface free boundary points approach the case at larger simulation time), such regions are linked to a smaller exposure time. However, the exposure map regarding case-insulating thermal protection material is conveniently expressed in length units instead of time units, where the length is identified by the amount of web. Notably, the web parameter at a specified time is obtained computing the integral of the burning rate-time profile up to the time instant of interest. Thus, the web represents the distance displaced by the burning surface from its initial position and the case itself. As a matter of fact, exposure maps are linked to the difference between the maximum web distance and the web value at each point of the case in order to better highlight the thermal protection exposure. This means that high exposure maps values correspond to case regions where the propellant is burned earlier with respect to case zones regarding lower exposure values. Therefore, maps high values coincide with early case-insulating material exposure. Hence, with the above-mentioned strategy, web maps do no longer depend on the burning rate at a specific time instant, but they are suitable for general values of burning rate. From a numerical perspective, with the aim of an effective and straightforward analysis of the case geometry, the red reference frame (Figure 28) is introduced.

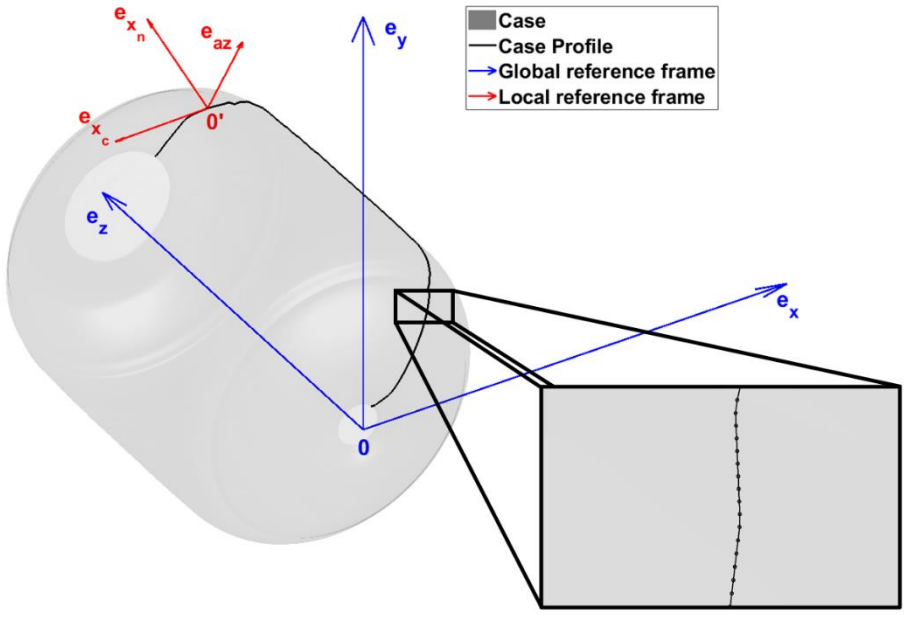

Figure 28: Reference frames.

It consists of three perpendicular unit vectors: e_{x_c}identifies the curvilinear coordinate along the case profile, e_{az} is the azimuthal coordinate unit vector along the circumferential direction around the

motor axis e_z, and e_{x_n} corresponds to the perpendicular direction to the plane of the case profile. Since exposure maps are computed on the case surface, the local reference frame $0'e_{x_c}e_{az}e_{x_n}$ establishes two coordinates needed for the graphical representation of the maps. Such quantities are x_c (curvilinear coordinate) and x_{az} (azimuthal coordinate). The second step regarding the identification of the debonding influence is the gradient computation of the web exposure map: indeed, the gradient is aimed to preliminary identify the most critical positions of debondings on case surface.

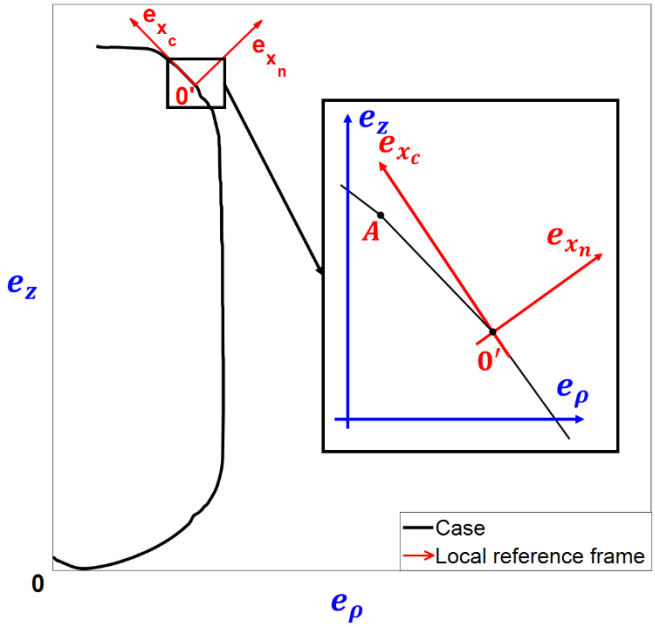

Figure 29: Reference frame for gradient computation.

The reference frame used to express the gradient is the local coordinate system (red reference frame in Figure 29) laying on the case envelope. The case profile is discretized into a certain number of small linear segments along the curvilinear coordinate (segment A0' in Figure 29 or the magnified window in Figure 29). That linear approximation guarantees a simpler form of the Lamè coefficients (subparagraph 3.3.1) regarding the gradient expression without loss of accuracy. In fact, it is sufficient to increase the number of linear discretization segments to obtain a more refined gradient map following in a more consistent way the case profile curvature. In addition to that, blue reference frame appearing in Figure 29 is the same global reference frame of Figure 28 but expressed in cylindrical coordinates with respect to the motor axis. The gradient of the web exposure map ϕ is identified by Eq. (1). More details on Eq. (1) are shown in subparagraph 3.3.1.

$$\nabla\phi = \frac{\partial\phi}{\partial x_c}\vec{e}_{x_c} + \frac{1}{(x_c - x_{c_{0'}})\sqrt{\frac{\beta^2}{\beta^2+\alpha^2}} + \rho_*}\frac{\partial\phi}{\partial x_{az,\theta}}\vec{e}_{az} \tag{1}$$

Eq. (1) is computed for each discretization segment of the case (segment A0' in Figure 29). α and β are defined by Eq. (2), representing the straight line passing through the two segment vertices (like A and 0'). In general, the case profile shape is known from the rocket geometry.

$$\alpha\rho + \beta z + \gamma = 0 \tag{2}$$

$$x_{az} = \rho \cdot x_{az,\theta} \tag{3}$$

ρ_* is the reference frame ($\rho_* = \rho_0$, in Figure 29) center radial position expressed in the global cylindrical reference frame x_{c_0}, is the curvilinear coordinate value up to the center of the local reference frame. Indeed, as pointed out before, the local reference frame is sequentially moved on each segment of the case in order to evaluate segment-by-segment gradient value of the case-insulating exposure map. $\frac{\partial \phi}{\partial x_c}$ and $\frac{\partial \phi}{\partial x_{az,\theta}}$ are approximated using a second order centered scheme respectively along the curvilinear coordinate and the azimuthal direction. Equation (3) shows the formula linking x_{az} and $x_{az,\theta}$: the gradient has been computed by considering the azimuthal coordinate expressed in angle ($x_{az,\theta}$) since the domain defined by $[x_{az,\theta_{min}}, x_{az,\theta_{max}}] \times [x_{c_{min}}, x_{c_{max}}]$ is rectangular, and then it has been represented with arch azimuthal coordinate (x_{az}). Once the debondings most critical positions are identified through the gradient maps, the effect of debonding extension along case curvilinear coordinate x_c and azimuthal coordinate x_{az} is investigated through a low time-consuming procedure. The following step represents the final point of the overall procedure. Starting from debondings critical positions, maps concerning the effect of different debondings positions on the case exposure are computed.

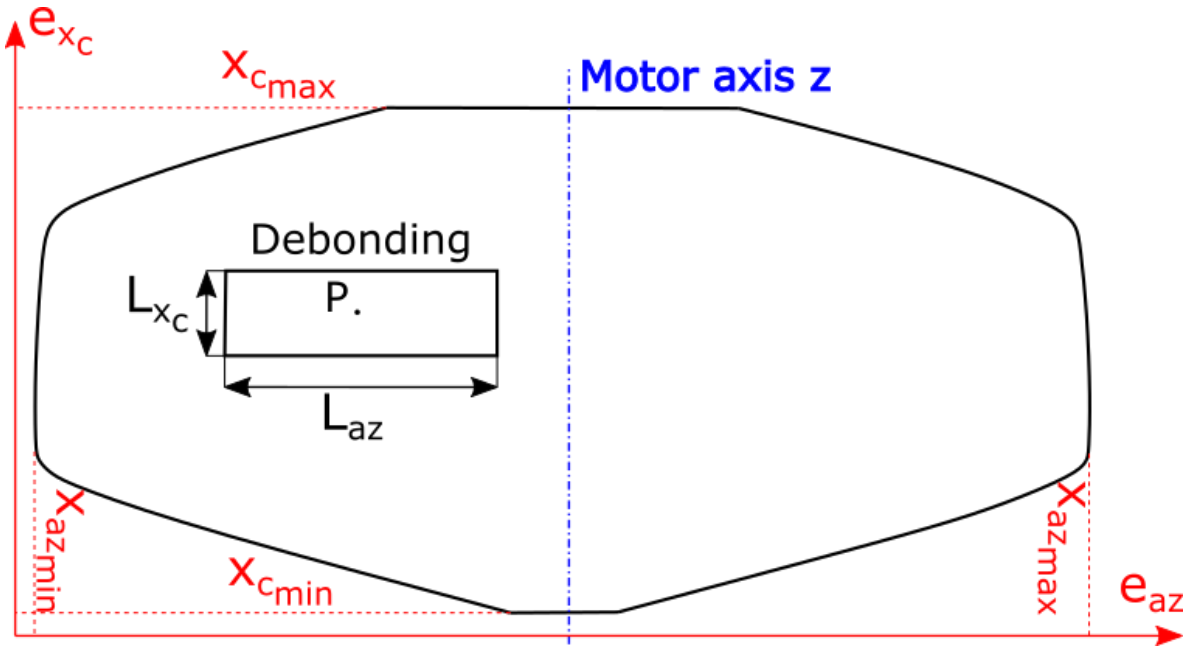

Figure 30: Debonding influence map generation.

First, size and geometry of the debonding along x_c and x_{az} are chosen (in Figure 30 the displayed debonding has a square-shaped geometry with dimensions L_{x_c} and L_{az}). Then, the debonding is positioned at different points on the case exposure map (in Figure 30 case exposure map is represented with black curve bounding the debonding). The new map, namely *debonding influence map*, is computed by associating at each point (linked to the debonding center, like point P in Figure 30) the difference between the maximum and the minimum web exposure among exposure values restrained

by the debonding geometry on the web exposure map itself. The new map is associated to the effect of the debonding positioned at each point on the case surface. No considerations have been introduced regarding the debonding thickness, namely the debonding size along the direction e_{x_n}. Indeed, in actual debondings the thickness is an order of magnitude lower than the other two dimensions, namely L_{x_c} and L_{az}. Thus, the thickness is assumed to have a lower effect in terms of anticipating the thermal protection case exposure with respect to the map obtained following the above-mentioned procedure. The maximum effect occurs when the burning surface moving toward the debonding remains parallel to the case. It is of fundamental importance to highlight that with such map (Figure 30), not only debondings extended in one direction (e_{x_c} or e_{az}) can be investigated. Such method offers the possibility to deal with debondings characterized by generic aspect ratio values, where the aspect ratio is intended as the ratio between L_{x_c} and L_{az}. Even more, generic-shaped debondings can be included. In fact, in order to generate the debonding position influence map, it is sufficient to superimpose the debonding generic shape on the case exposure map and evaluating, as already mentioned before, the maximum difference among the exposure values bounded by the debonding itself. Finally, the above-mentioned procedure is validated with respect to ROBOOST software by comparing the two results for a series of debondings. Their location has been conveniently chosen in the direction of investigating both the most critical positions on the case and the impact of the debonding direction of elongation.

3.3.1Formulation of exposure map gradient expression

The abovementioned thermal protection exposure maps have been obtained in a curvilinear reference frame described in 0. This curvilinear coordinate system can be described by three orthogonal level surfaces:

$$\begin{cases} w_1 = f(x,y,z) \\ w_2 = g(x,y,z) \\ w_3 = z(x,y,z) \end{cases} \tag{4}$$

Where w_1, w_2 and w_3, are the curvilinear coordinate, x, y, z are the Cartesian coordinate. In the curvilinear reference frame, the gradient is written as follow:

$$\nabla\varphi = \sum_{j=1}^{3} \frac{1}{h_j}\frac{\partial\varphi}{\partial w_j}\hat{h}_j = \sum_{j=1}^{3} \frac{\vec{h}_j}{\left\|\vec{h}_j\right\|^2}\frac{\partial\varphi}{\partial w_j} \tag{5}$$

$$\vec{h}_j = \frac{\partial\vec{r}}{\partial w_j} \tag{6}$$

$$h_j = \left\|\frac{\partial\vec{r}}{\partial w_j}\right\| \tag{7}$$

Where h_j are the Lamè coefficients, $\vec{r}$ is the position vector and in the Cartesian coordinate it is written as follow

$$\vec{r} = x\, e_x + y\, e_y + z\, e_z \tag{8}$$

Where e_x, e_y, e_z are the Cartesian basis. To evaluate the Lamè coefficients, the vector $\vec{r}$ needs to be written as function of the curvilinear coordinate (w_1, w_2, w_3).

$$\vec{r} = k_x(w_1, w_2, w_3)\, e_x + k_y(w_1, w_2, w_3)\, e_y + k_z(w_1, w_2, w_3)\, e_z \tag{9}$$

$$\begin{cases} x = k_x(w_1, w_2, w_3) \\ y = k_y(w_1, w_2, w_3) \\ z = k_z(w_1, w_2, w_3) \end{cases} \tag{10}$$

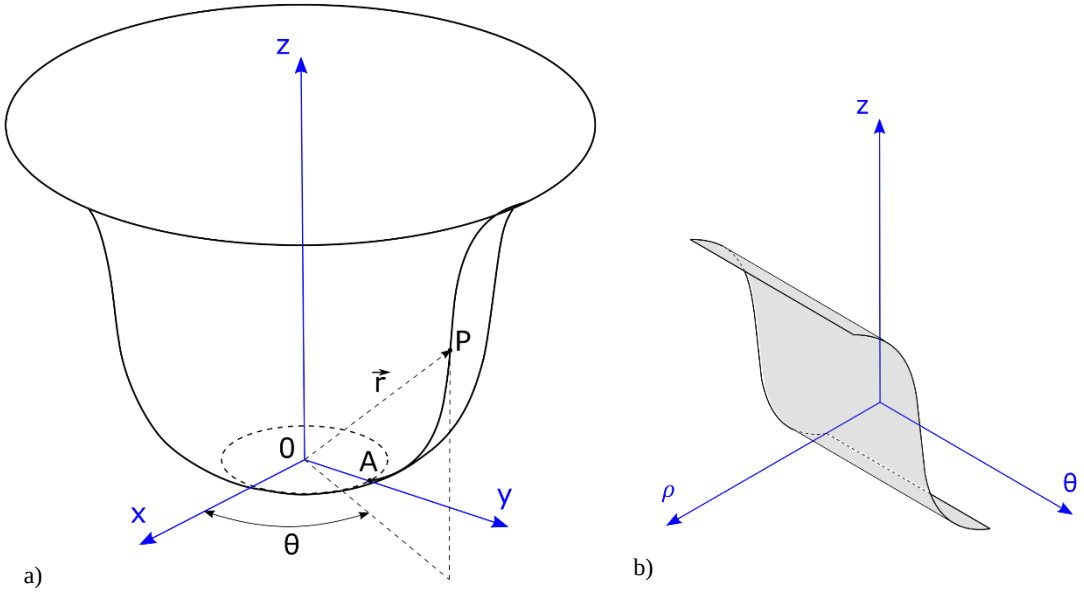

Figure 31: Surface of revolution.

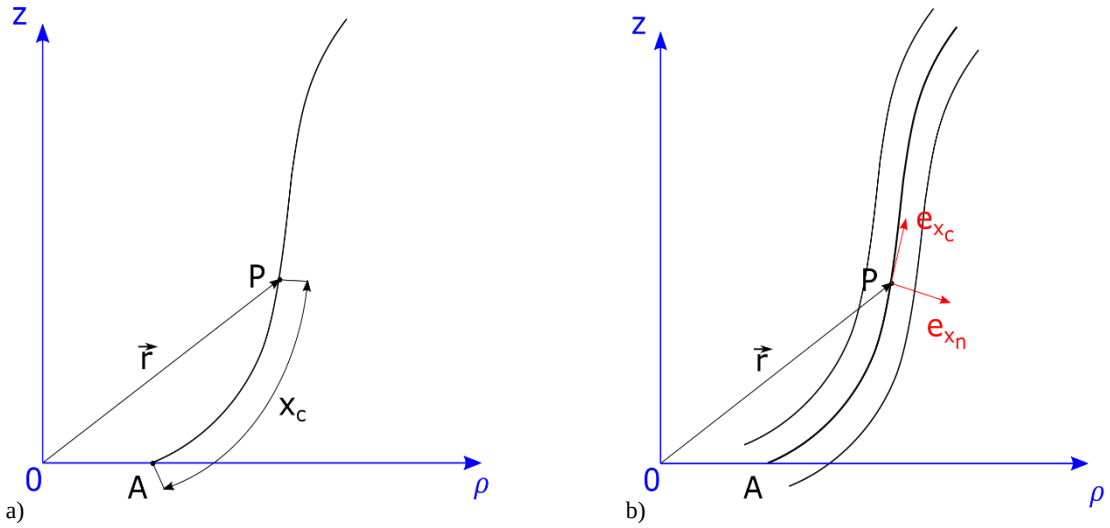

Figure 32: Curvilinear coordinate system.

Figure 31a shows a general revolution surface obtained rotating the red curve along the z-axis. w_2 is defined as the angle θ between the projection of $\vec{r}$ on xy-plane and the x-axis. Figure 31b shows the same surface in cylindrical coordinate. Figure 31shows the definition of w_1 and w_3: w_1 is defined as the length of red curve from the point A to P, w_3 is the last coordinate defined by the basis always orthogonal to the case surface.

$$\begin{gathered} w_1 = x_c = \int_A^P ds \\ w_2 = \theta \\ w_3 = x_n \end{gathered} \tag{11}$$

The functions k_x, k_y and k_z in the general form are quite complicated to be obtained, but the gradient needs to evaluate on the case surface, therefore k_x, k_y and k_z could be written considering small values of x_n. The black solid curves in Figure 32b are the isoline for the curvilinear coordinate x_n. For small value of x_n, a general point (x, y, z) could be written as follow:

$$\begin{aligned} x = k_x(x_c, \theta, x_n) &= \rho(x_c)\cos(\theta) + \hat{n}_x(x_c, \theta)x_n \\ y = k_y(x_c, \theta, x_n) &= \rho(x_c)\sin(\theta) + \hat{n}_y(x_c, \theta)x_n \\ z = k_z(x_c, \theta, x_n) &= a(x_c) + \hat{n}_z(x_c, \theta)x_n \end{aligned} \tag{12}$$

where $\hat{n}$ is the normal to the case. Therefore, it is straightforward the evaluation $\vec{r}$ and the Lamé coefficients.

$$\begin{gathered} \vec{r} = [\rho(x_c)\cos(\theta) + \hat{n}_x(x_c, \theta)x_n]\,\hat{e}_1 + [\rho(x_c)\sin(\theta) + \hat{n}_y(x_c, \theta)x_n]\,\hat{e}_2 + [a(x_c) + \hat{n}_z(x_c, \theta)x_n]\,\hat{e}_3 \\ \vec{h}_1 = \frac{\partial \vec{r}}{\partial w_1} = \frac{\partial \vec{r}}{\partial x_c} = \left[\frac{\partial \rho}{\partial x_c}\cos(\theta) + \frac{\partial \hat{n}_x}{\partial x_c}x_n\right] e_x + \left[\frac{\partial \rho}{\partial x_c}\sin(\theta) + \frac{\partial \hat{n}_y}{\partial x_c}x_n\right] e_y + \left[\frac{\partial a}{\partial x_c} + \frac{\partial \hat{n}_z}{\partial x_c}x_n\right] e_z \\ \left\|\vec{h}_1\right\|^2 = \left(\frac{\partial \rho}{\partial x_c}\right)^2 + \left(\frac{\partial a}{\partial x_c}\right)^2 + \left[\left(\frac{\partial \hat{n}_x}{\partial x_c}\right)^2 + \left(\frac{\partial \hat{n}_y}{\partial x_c}\right)^2 + \left(\frac{\partial \hat{n}_z}{\partial x_c}\right)^2\right](x_n)^2 + 2\left[\frac{\partial \rho}{\partial x_c}\cos(\theta)\frac{\partial \hat{n}_x}{\partial x_c} + \frac{\partial \rho}{\partial x_c}\sin(\theta)\frac{\partial \hat{n}_y}{\partial x_c} + \frac{\partial a}{\partial x_c}\frac{\partial \hat{n}_z}{\partial x_c}\right]x_n \\ \vec{h}_2 = \frac{\partial \vec{r}}{\partial w_2} = \frac{\partial \vec{r}}{\partial \theta} = \left[-\rho(x_c)\sin(\theta) + \frac{\partial \hat{n}_x}{\partial \theta}x_n\right] e_x + \left[\rho(x_c)\cos(\theta) + \frac{\partial \hat{n}_y}{\partial \theta}x_n\right] e_y + \left[\frac{\partial \hat{n}_z}{\partial \theta}x_n\right] e_z \\ \left\|\vec{h}_2\right\|^2 = \rho(x_c)^2 + \left[\left(\frac{\partial \hat{n}_x}{\partial \theta}\right)^2 + \left(\frac{\partial \hat{n}_y}{\partial \theta}\right)^2 + \left(\frac{\partial \hat{n}_z}{\partial \theta}\right)^2\right](x_n)^2 + 2\left[-\rho(x_c)\sin(\theta)\frac{\partial \hat{n}_x}{\partial \theta} + \rho(x_c)\cos(\theta)\frac{\partial \hat{n}_y}{\partial \theta}\right]x_n \\ \vec{h}_3 = \frac{\partial \vec{r}}{\partial w_3} = \frac{\partial \vec{r}}{\partial x_n} = \hat{n}_x(x_c, \theta)\,e_x + \hat{n}_y(x_c, \theta)\,e_y + \hat{n}_z(x_c, \theta)\,e_z \\ \left\|\vec{h}_3\right\|^2 = \hat{n}_x(x_c, \theta)^2 + \hat{n}_y(x_c, \theta)^2 + \hat{n}_z(x_c, \theta)^2 = 1 \end{gathered} \tag{13}$$

Assuming $x_n \to 0$, the Lamé coefficients becomes:

$$\begin{gathered} \vec{h}_1 = \frac{\partial \vec{r}}{\partial w_1} = \frac{\partial \vec{r}}{\partial x_c} = \frac{\partial \rho}{\partial x_c}\cos(\theta)\,e_x + \frac{\partial \rho}{\partial x_c}\sin(\theta)\,e_y + \frac{\partial a}{\partial x_c}\,e_z \\ \left\|\vec{h}_1\right\|^2 = \left(\frac{\partial \rho}{\partial x_c}\right)^2 + \left(\frac{\partial a}{\partial x_c}\right)^2 \\ \vec{h}_2 = \frac{\partial \vec{r}}{\partial w_2} = \frac{\partial \vec{r}}{\partial \theta} = -\rho(x_c)\sin(\theta)\,e_x + \rho(x_c)\cos(\theta)\,e_y \\ \left\|\vec{h}_2\right\|^2 = \rho(x_c)^2 \end{gathered} \tag{14}$$

$$\vec{h}_3 = \frac{\partial \vec{r}}{\partial w_3} = \frac{\partial \vec{r}}{\partial x_n} = \hat{n}_x(x_c,\theta)e_x + \hat{n}_y(x_c,\theta)e_y + \hat{n}_z(x_c,\theta)e_z = \hat{n}$$

$$\left\|\vec{h}_3\right\|^2 = 1$$

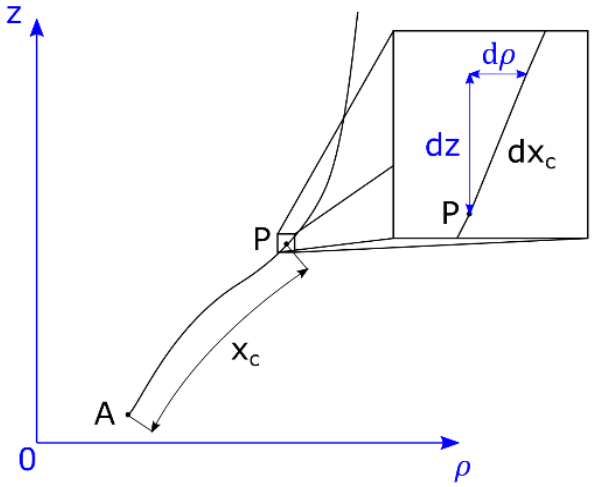

Figure 33: Geometric relation.

With reference to Figure 33, Eq. (15) is established.

$$\left(\frac{\partial \rho}{\partial x_c}\right)^2 + \left(\frac{\partial a}{\partial x_c}\right)^2 = 1 \tag{15}$$

$$d\rho = \frac{\partial \rho}{\partial x_c} dx_c, da = \frac{\partial a}{\partial x_c} dx_c \tag{16}$$

Applying the Pythagoras theorem on the triangle shown in Figure 33, Eq. (17) is obtained.

$$dx_c = \sqrt{d\rho^2 + da^2} = \sqrt{\left(\frac{\partial \rho}{\partial x_c}\right)^2 + \left(\frac{\partial a}{\partial x_c}\right)^2}\, dx_c \tag{18}$$

The previous result is then substituted into Eq. (14), leading to Eq. (19).

$$\nabla\varphi = \sum_{j=1}^{3} \frac{\vec{h}_j}{\left\|\vec{h}_j\right\|^2}\frac{\partial \varphi}{\partial w_j} = \frac{\partial \varphi}{\partial x_c}\frac{\vec{h}_1}{\left\|\vec{h}_1\right\|^2} + \frac{\partial \varphi}{\partial \theta}\frac{\vec{h}_2}{\left\|\vec{h}_2\right\|^2} + \frac{\partial \varphi}{\partial x_n}\frac{\vec{h}_3}{\left\|\vec{h}_3\right\|^2} =$$
$$= \frac{\partial \varphi}{\partial x_c}\left[\frac{\partial \rho}{\partial x_c}\cos(\theta)\, e_x + \frac{\partial \rho}{\partial x_c}\sin(\theta)\; e_y + \frac{\partial a}{\partial x_c}\; e_z\right]$$
$$+ \frac{\partial \varphi}{\partial \theta}\frac{\left[-\rho(x_c)\sin(\theta)\; e_x + \rho(x_c)\cos(\theta)\, e_y\right]}{\rho(x_c)^2} + \frac{\partial \varphi}{\partial x_n}\,\hat{n} \tag{19}$$

$$= \frac{\partial \varphi}{\partial x_c}\left[\frac{\partial \rho}{\partial x_c}\cos(\theta)\, e_x + \frac{\partial \rho}{\partial x_c}\sin(\theta)\; e_y + \frac{\partial a}{\partial x_c}\; e_z\right] + \frac{\partial \varphi}{\partial \theta}\frac{1}{\rho(x_c)}\left[-\sin(\theta)\; e_x + \cos(\theta)\, e_y\right] + \frac{\partial \varphi}{\partial x_n}\,\hat{n}$$

$$\hat{e}_{x_c} = \frac{\partial \rho}{\partial x_c}\cos(\theta)\, e_x + \frac{\partial \rho}{\partial x_c}\sin(\theta)\; e_y + \frac{\partial a}{\partial x_c}\; e_z$$

$$\hat{e}_\theta = -\sin(\theta)\; e_x + \cos(\theta)\, e_y$$

$$\nabla\varphi = \frac{\partial \varphi}{\partial x_c}\hat{e}_{x_c} + \frac{\partial \varphi}{\partial \theta}\frac{1}{\rho(x_c)}\hat{e}_\theta + \frac{\partial \varphi}{\partial x_n}\,\hat{n}$$

Finally, it is possible to introduce x_{ac} coordinate: $x_{ac} = \theta\ \rho(x_c)$, therefore:

$$\frac{\partial \varphi}{\partial \theta} = \frac{\partial \varphi}{\partial x_{ac}}\frac{\partial x_{ac}}{\partial \theta} = \frac{\partial \varphi}{\partial x_{ac}}\ \rho(x_c) \tag{20}$$

The Eq. 14 could be specialized for a discretized shape of the case. The parametric curve defined by $\big(\rho(x_c), a(x_c)\big)$ could be discretized in segments which could be described by the following equation (Eq. (21)):

$$\alpha\rho + \beta z + \gamma = 0 \rightarrow z = -\frac{\alpha}{\beta}\rho \rightarrow dz = -\frac{\alpha}{\beta}d\rho \tag{21}$$

where α and β are the two coefficients obtained by the subsequent linearization.

$$x_c' = \int_C^D ds = \int_C^D \sqrt{(d\rho)^2 + dz^2} = \int_{\rho_C}^{\rho_D} \sqrt{1 + \left(\frac{\alpha}{\beta}\right)^2}\, d\rho = \sqrt{\frac{\beta^2 + \alpha^2}{\beta^2}}(\rho_D - \rho_C) \tag{22}$$

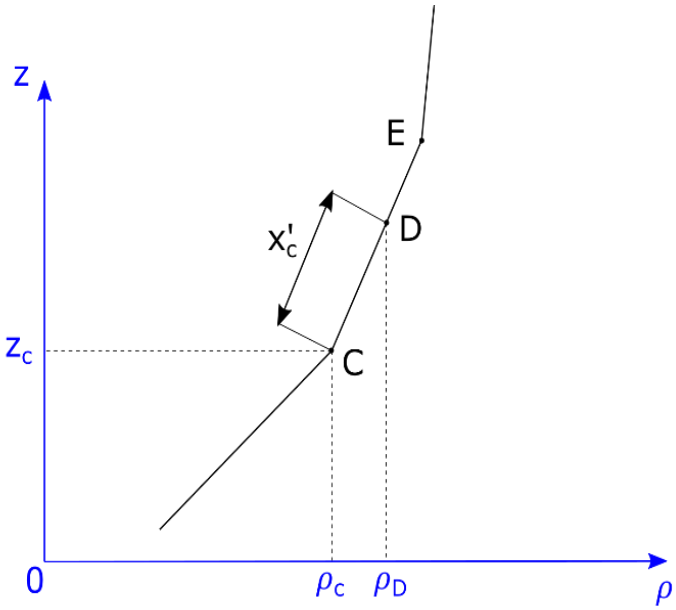

Figure 34: Case profile discretization.

$$\rho_D = \frac{x'_c}{\sqrt{\frac{\beta^2+\alpha^2}{\beta^2}}} + \rho_C = \sqrt{\frac{\beta^2}{\beta^2+\alpha^2}}\, x'_c + \rho_C \tag{23}$$

Then, Eq. (23) is substituted into the Eq. (19), where $\rho = \rho_D$. Eq. (24) is obtained.

$$\nabla\varphi = \frac{\partial\varphi}{\partial x_c}\hat{e}_{x_c} + \frac{\partial\varphi}{\partial\theta}\frac{1}{\sqrt{\frac{\beta^2}{\beta^2+\alpha^2}}\, x'_c + \rho_C} + \frac{\partial\varphi}{\partial x_n}\hat{n} \tag{24}$$

Only the gradient component along $\hat{e}_{x_c}$ and $\hat{e}_\theta$ are important, because the thermal protection maps belong to the case surface, therefore the previous gradient becomes

$$\nabla\varphi = \frac{\partial\varphi}{\partial x_c}\hat{e}_{x_c} + \frac{\partial\varphi}{\partial\theta}\frac{1}{\sqrt{\frac{\beta^2}{\beta^2+\alpha^2}}\, x'_c + \rho_C}\hat{e}_\theta \tag{25}$$

3.4 Numerical results

3.4.1 Cavities

As a first step ROBOOST simulation software has been applied to the third stage of Vega launcher, namely Z9 (ZEFIRO 9). Vega is designed to launch small payloads — up to 1,500 kg satellites for scientific and Earth observation missions in low Earth orbits. It consists of 4 stages: 3 of them are

solid propellant based, the fourth, coupled with the payload fairing, is essentially a liquid propellant engine. Z9 is 3.5 meters tall, has a diameter of slightly less than 2 meters, weighs 11.5 tons and burns 10.5 tons of high-density Al-HTPB-AP composite propellant. Its central bore has a circular section in the fore and the central part, a finocyl-shaped configuration in the rear part near the nozzle inlet.

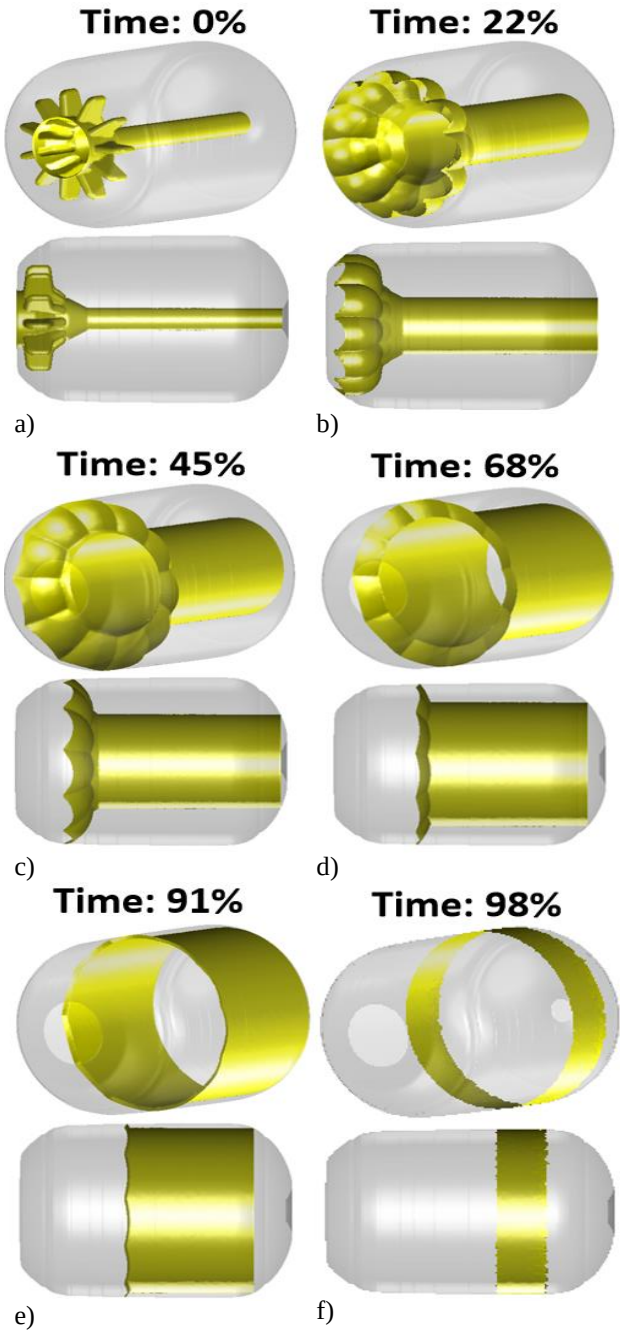

Figure 35: Burning surface regression in Z9.

The motor solid geometry has been generated using SolidWorks CAD software and its conversion to triangle surface mesh has been completed with an opensource software that is a free 3D finite element mesh generator, namely Gmsh [11]. A variable resolution in the range of 5÷30 millimeters is established for the burning surface: indeed, smallest triangles are located close to mesh high curvature

regions, instead the largest ones are centered in low curvature zones. The propellant burning surface regression, obtained with ROBOOST software, is shown in Figure 35.
A comparison between simulation and experimental motor internal pressure is proposed (Figure 36a). The red experimental profile of Z9 firing is assumed as reference curve.

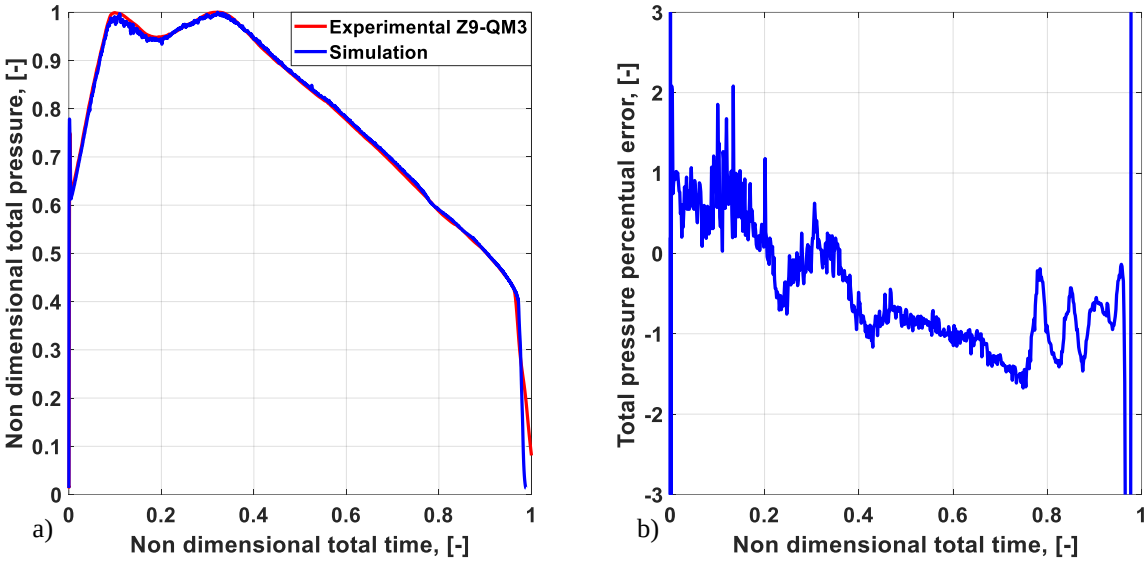

Figure 36: Combustion chamber pressure comparison.

Contributions provided by igniter [12], nozzle erosion [13], and ablation of thermal protections [13], are considered in the abovementioned simulation. Thermal protection contribution is obtained using a semi-empirical formulation developed starting from models explained in [14, 15]. Moreover, an empirical web-dependent Hump function [16], acquired from real firing test, is included in the burn rate computation in the direction of giving a pressure estimation closer to reality. Hump function essentially involves the influence that grain heterogeneities, due to propellant casting process, have on combustion chamber pressure. Total pressure relative percentage error computed with respect to the experimental data (Figure 36b), belongs to a variation range of ±2% which can be considered satisfactory. Figure 37 shows thermal protections exposure time along SRM case.

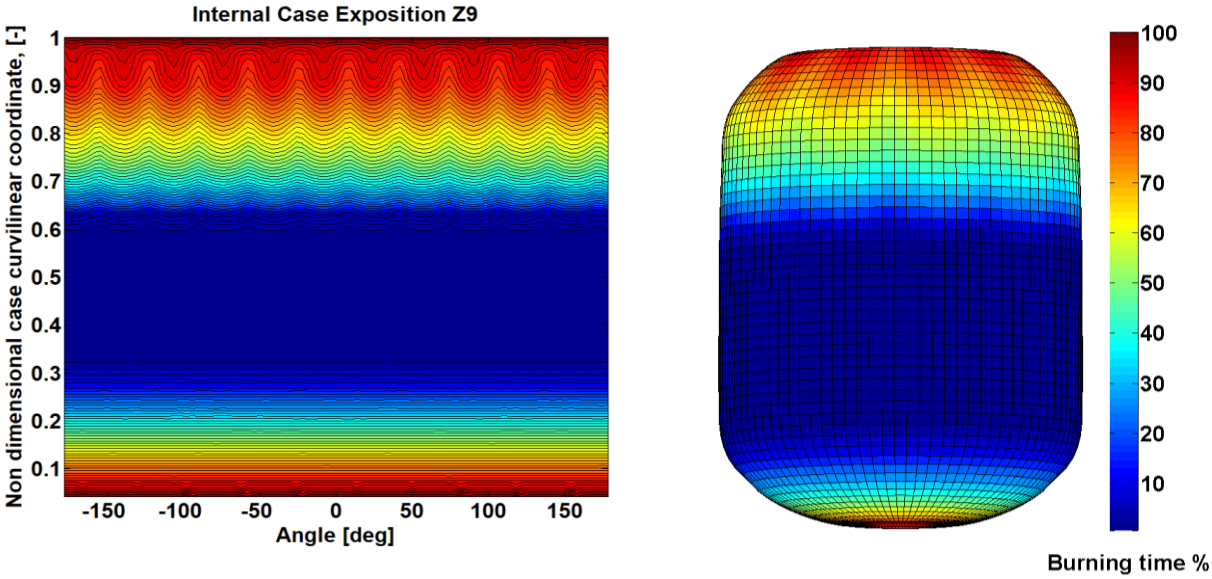

Figure 37: Z9 thermal protection exposure map.

The contour map represents a color-varying scale linked to case exposition time percentage (time has been normalized with respect to burnout time). Indeed red-orange zones are the first ones to be exposed to the combustion chamber heat; on the other hand, blue regions correspond to lower thermally stressed regions due to an exposition time close to zero. All previously mentioned considerations make internal case exposition map an effective tool to preliminary design thermal protections thickness for a SRM case.

After validating the code, the following simulation shows the impact of inclusions within the propellant on Z9 combustion chamber ballistics. The same mesh used in the validation process has been employed also in this simulation. Moreover, it is assumed a certain spatial distribution of air inclusions (Figure 38a, b, c). 46 spherical shaped cavities with a diameter of 20 millimeters are considered in the simulation ((Figure 38d). Such cavitiy spatial distribution has been obtained from experimental data. In general, the occurrence of cavities is checked through radiography as a non-destructive diagnostic tool for measuring spatial position and surface extension of each cavity. More in detail, an ordinary x-ray imaging system shows an accuracy of about 0.5 mm. Inspection tests are applied to both the overall motor and/or at specific regions. Cavities identification is useful to determine, by the above-mentioned procedure, the effect on the exposure of case thermal protection insulating material. If this exposure has been considered unacceptable, the SRM would probably undergo specific attempts of repair before final firing.

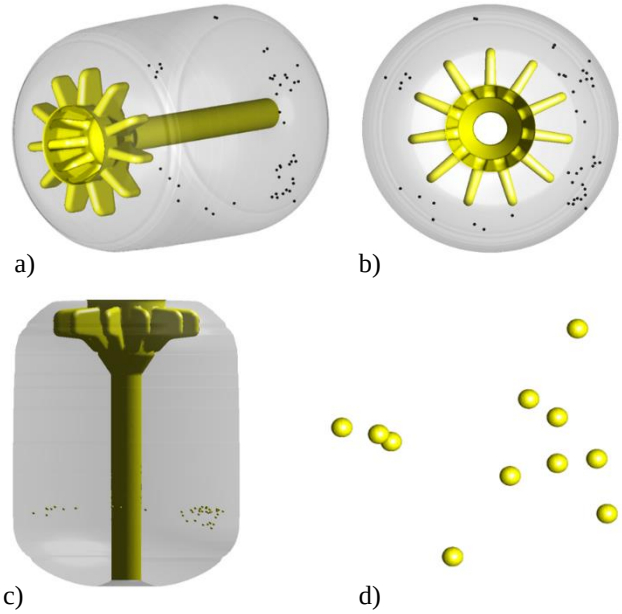

Figure 38: Z9 with inclusions.

Figure 39 shows burning surface regression results. From a qualitative point of view, it is possible to highlight that, when cavities are included (Figure 39d, e, f), surface evolution changes with respect to standard Z9 configuration (Figure 35d, e, f).

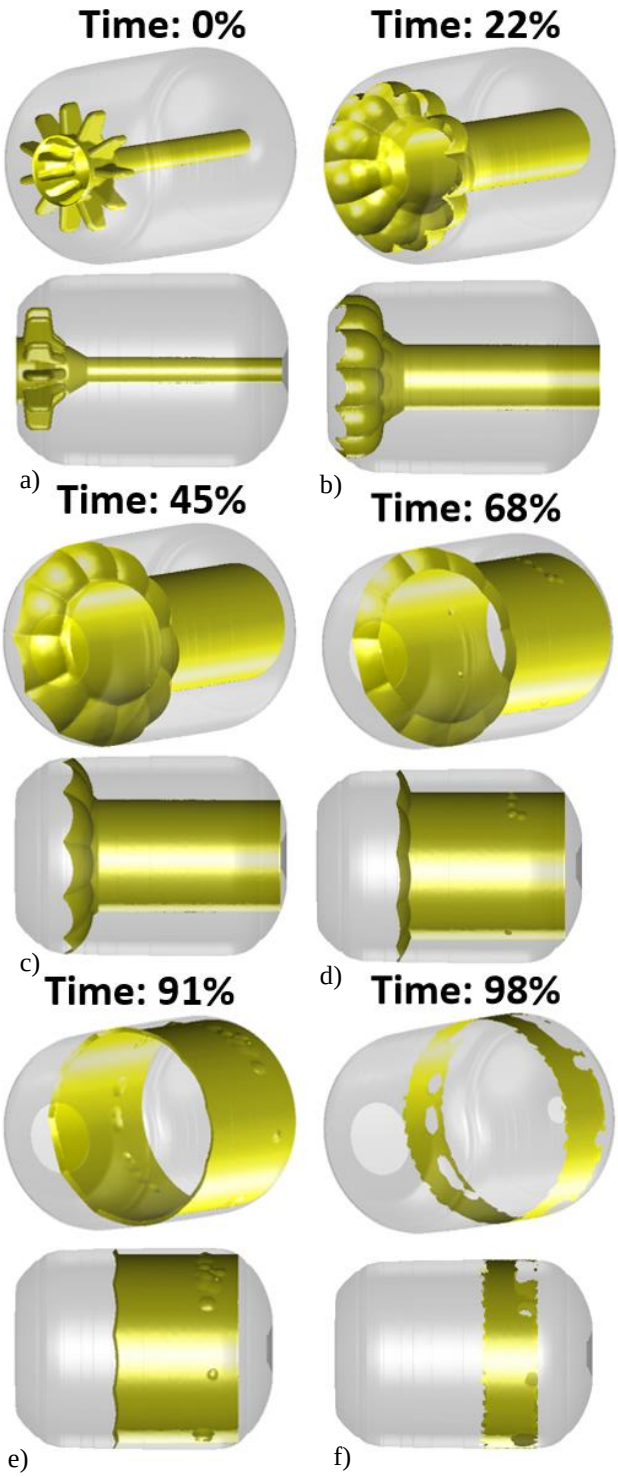

Figure 39: Burning surface regression in Z9 with inclusions.

The percentual difference (Figure 40b, Figure 41b) is computed as the relative error with respect to standard Z9 configuration shown before.

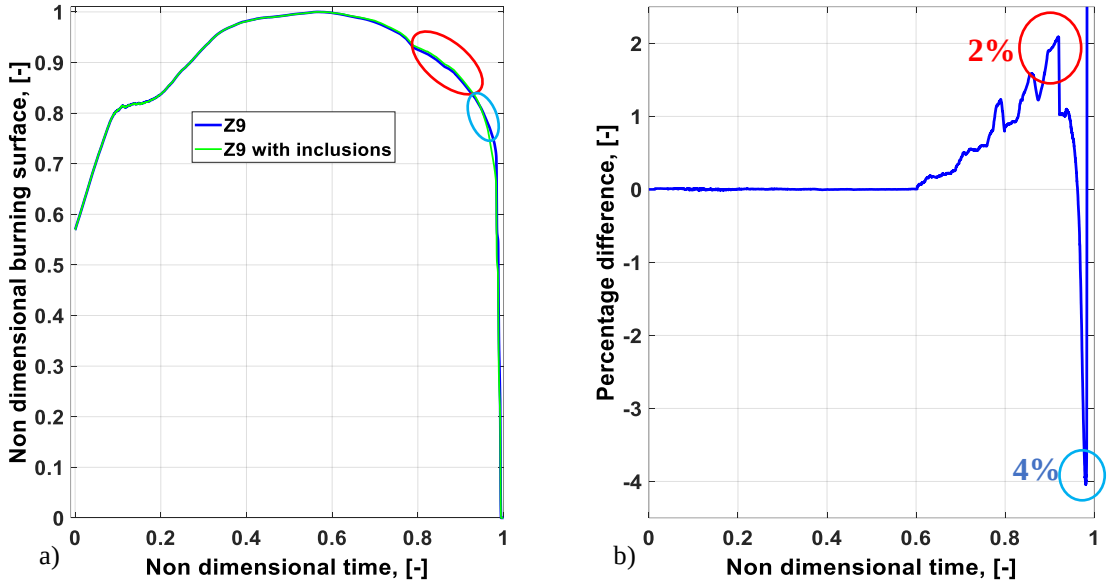

Figure 40: Burning surface comparison.

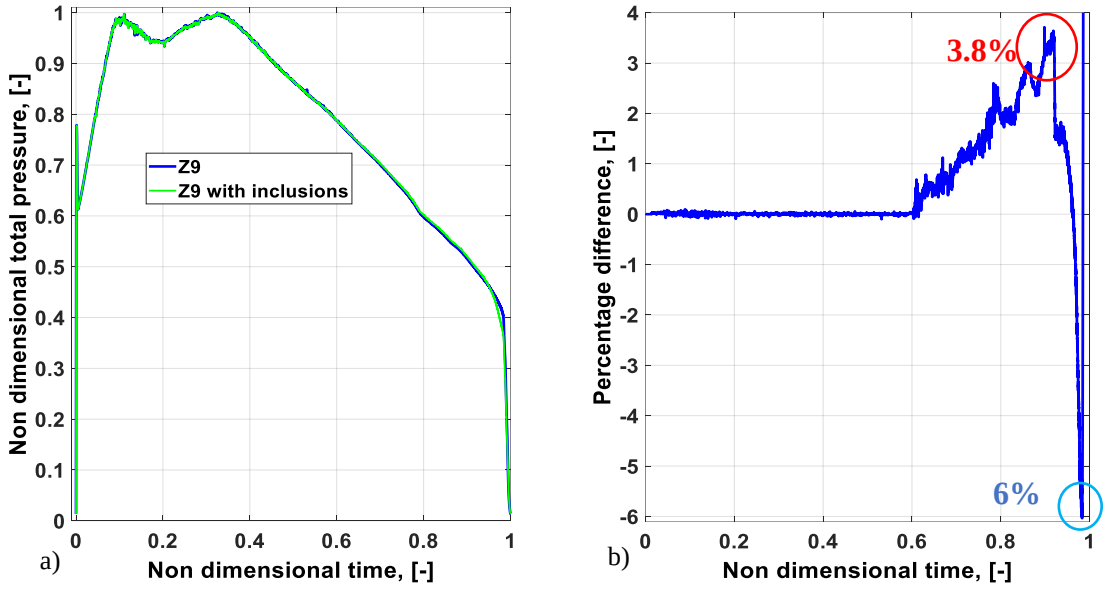

Figure 41: Combustion chamber pressure comparison.

When inclusions are introduced, an increment of burning surface occurs with a peak of 2% with respect to the standard Z9 simulation (Figure 40b), implying a combustion chamber pressure increasing of 3.8% (Figure 41b). However, because of cavities surface evolution during the regression phenomenon (Figure 39e), the burning surface approaches earlier the case, thus the burning surface decreases faster in time. At 98 % of the burn out time, the burning surface of Z9 with cavities is 4% lower than Z9 without them and the pressure is 6% lower. Hence the pressure variation due to the simulated cavities distribution is quite bounded. On the other hand, case exposition shows a more critical behavior. Figure 42 shows the difference between Z9 exposition time with cavities and the previous Z9 exposition time map (Figure 37). The contour map is linked to how much earlier Z9 case with cavities is exposed to combustion chamber heat. A peak of 5 seconds earlier is reached along

the region where most of the cavities are located: this could give the possibility to perform a theoretical check on the capability of the insulation layer to withstand thermal stresses.

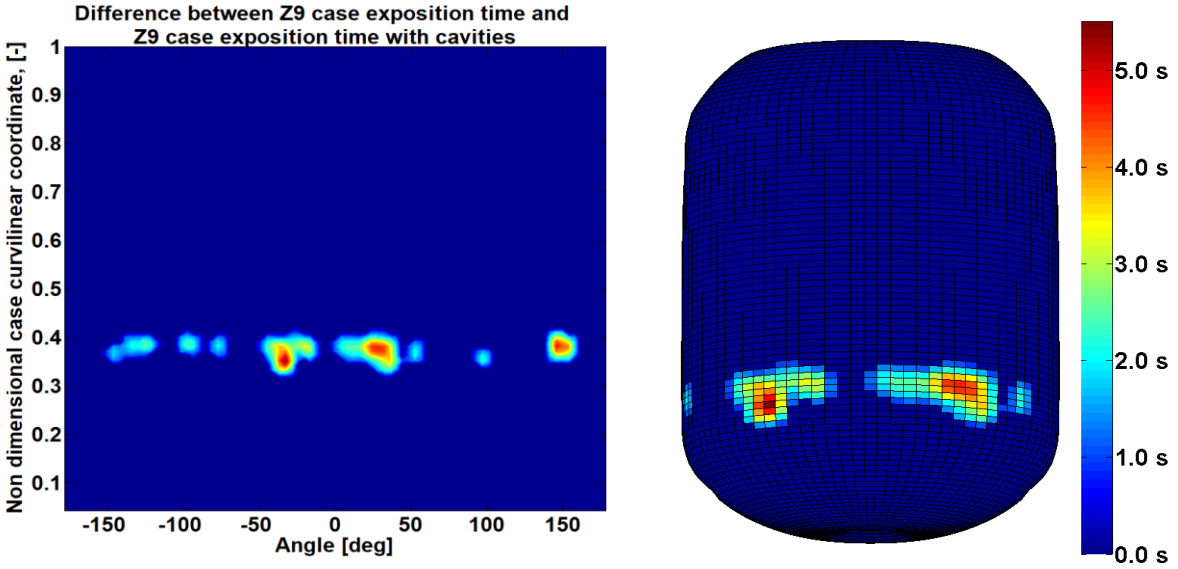

Figure 42: Thermal protection exposure comparison.

Finally, it must be highlighted that, since cavities occurrence within the grain implies an increment of burning surface, a larger cavity size will almost certainly further increase the burning surface leading to a larger pressure rise and case thermal protection sooner exposure. The final effect could even be rocket failure if the pressure becomes higher than the design pressure or case thermal protection layer is depleted before the end of grain combustion.

3.4.2 Debonding maps

The map generation method explained in the previous chapter has been applied to the third stage of a Vega launcher, namely, ZEFIRO 9 (Z9). Regarding the propellant geometry configuration, it has been designed with a circular section in the fore and central parts, and with a finocyl shaped configuration in the rear part near the nozzle inlet (Figure 43).

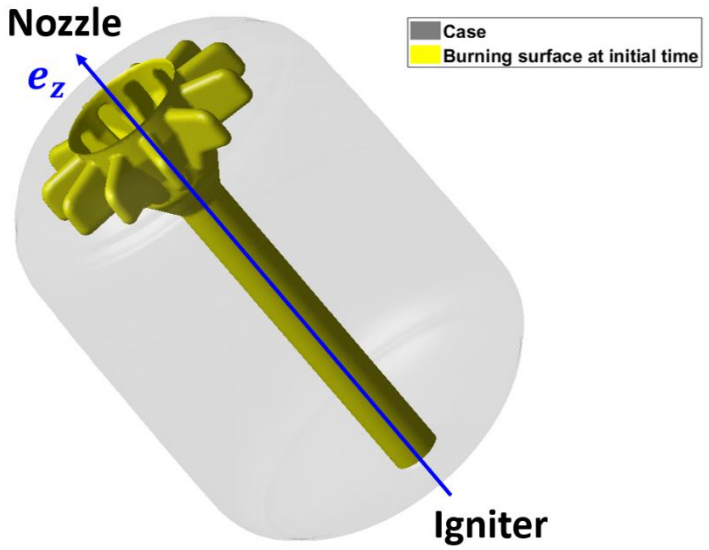

Figure 43: ZEFIRO 9 central bore.

Figure 44a shows the case-insulating thermal protection exposure map of Z9 computed with ROBOOST software. The web exposure has been normalized by dividing all values by the maximum web exposure. The same procedure has been performed for both the curvilinear coordinate x_c and the azimuthal coordinate x_{az}, respectively dividing them with respect to the two maximum values $x_{c_{max}}$ and $x_{az_{max}}$.

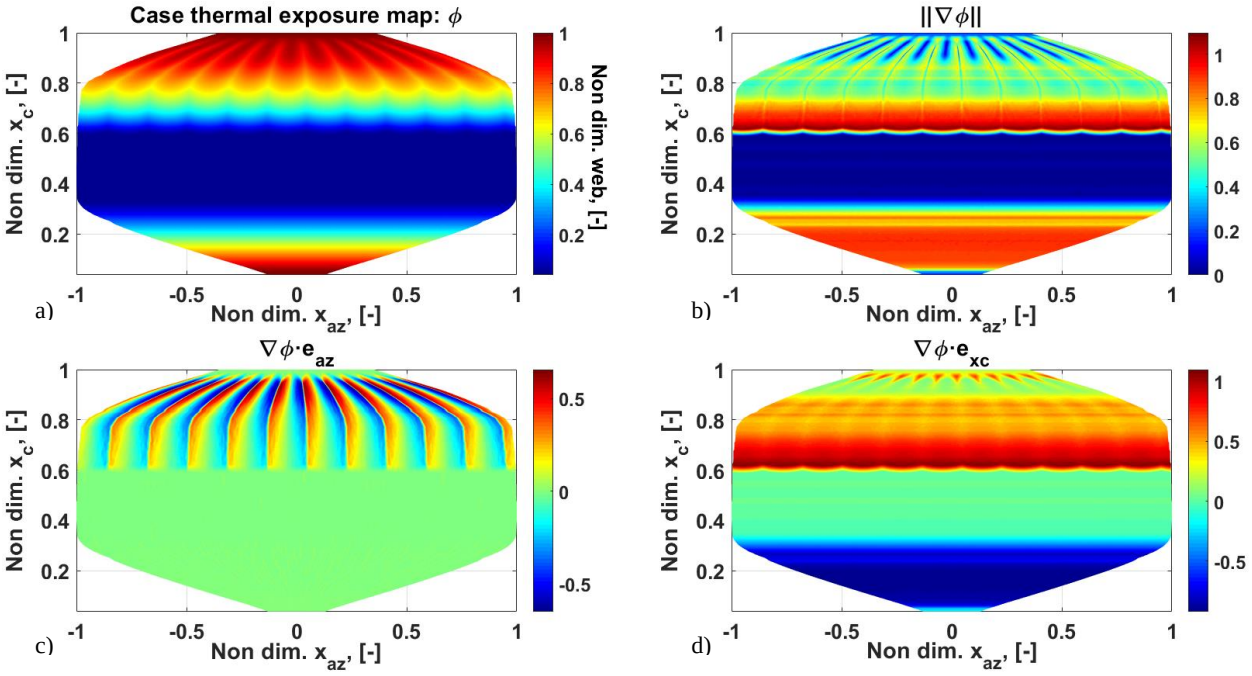

Figure 44: Maps linked to case exposure and case exposure gradient.

The above-mentioned map exhibits the maximum exposure close to the curvilinear coordinate level corresponding to the finocyl region of the burning surface (Figure 43). Indeed, the local distance between each lobe of the finocyl configuration and the case is lower than the distance referred to the burning surface cylindrical region. Thus, it is evident that the case region at the same level of finocyl

shape is sooner exposed to combustion chamber hot gases than the other regions. However, there is another region of the SRM which presents such sooner exposure. These zones correspond to the end of the cylindrical shape and the end of the finocyl respectively in proximity of the igniter and the nozzle. In fact, the burning surface recedes along the case meaning that, during its outward advancement in radial direction with respect to the motor axis, the propellant is gradually depleted causing the local uncovering of the case thermal protection layer. Figure 44c and d are respectively linked with the projection of case exposure map gradient along the azimuthal coordinate direction (e_{az}) and the curvilinear coordinate direction (e_{x_c}). In Figure 44c the green regions correspond to a zero-value gradient implying that a low impact on thermal exposure occurs for debondings mainly elongated along the azimuthal coordinate. The above-mentioned statement can be explained in accordance with the burning surface motion toward the case, indicating that the burning surface reaches the case remaining parallel to it. The same considerations are valid for green regions in Figure 44d, where the gradient trend is linked to debondings mainly elongated along the curvilinear coordinate direction. On the other hand, regions with high gradient values (dark red and dark blue regions) regards case portions, where the possible presence of debondings could significatively impact the thermal protection exposition in terms of web exposure anticipation. Finally, Figure 44b displays the gradient norm regarding the exposure influence of debondings whose aspect ratio, computed by dividing its azimuthal coordinate and curvilinear coordinate elongation, is close to 1. Highly critical locations are depicted with red color, nearly zero gradient zones with blue color. According to the local reference frame directions (red reference frame in Figure 30), two set of debondings are evaluated: the first set is characterized by the main elongation along the azimuthal coordinate, the second set is linked to curvilinear coordinate elongation. Subsequently, it has been considered a debonding shaped with the curvilinear coordinate length in the same order of magnitude with respect to the azimuthal coordinate extension to prove the effectiveness of the overall procedure.

First set of debonding

The length of the main dimension of the flaw has been chosen equal to $207\ mm$. The reason of this choice is associated with the evaluation of the minimum distance between two zero level regions containing the maximum absolute peak (positive or negative) in Figure 44c. This extension of the flaw is in fact capable to generate the highest thermal protection exposure increment in the azimuthal direction and it is, for this reason, particularly interesting.

Based on this choice the first set of debonding has the following dimensions: $L_{az} = 207\ mm$, $L_{x_c} = 10\ mm$ and $L_{x_n} = 5\ mm$. L_{x_c} and L_{x_n} have been set respectively to $10\ mm$ and $5\ mm$ with the aim of obtaining a debonding mainly extended along e_{az}.

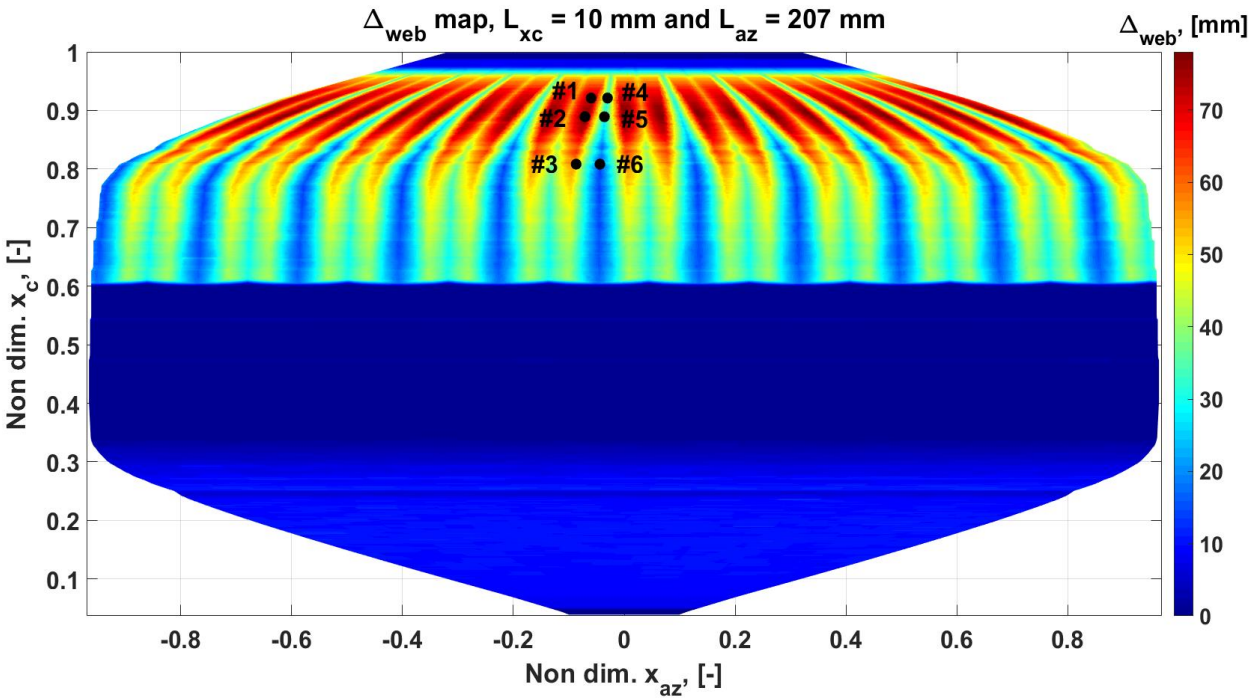

Figure 45: Debonding influence map regarding debonding elongation along e_{az}

Exposure increase map shown in Figure 45 is obtained following the procedure outlined in the previous section for the first set of flaws. Each point on the map represents the exposure increase that would be generated by a debonding characterized by the pre-defined geometry and centered on that point, with respect to the nominal motor. Eleven green-to-red colored regions are shown in the higher portion of Figure 45: each region corresponds to an evenly spaced lobe associated with the propellant finocyl configuration of Z9. Each of the identified regions contains two light red strips, each on them characterized by a dark red spot. The location of that spot corresponds to the maximum exposure increase ($76\ mm$) and coincides with the maximum gradient position in Figure 44c.

In order to validate the obtained results, six debonding positions (black dots in Figure 45, marked from 1 to 6) have been chosen, located at 3 levels of x_c and 2 levels of $x_{az,\theta}$ ($x_{az,\theta} = -16.55°$ and $x_{az,\theta} = -8°$): in particular debonding $1, 2, 3$ belong to level $x_{az,\theta} = -16.55°$, while debonding $4, 5, 6$ belongs to level $x_{az,\theta} = -8°$.

Each position is subsequently implemented inside the tool ROBOOST to perform a complete regression simulation, obtaining the corresponding 3D evolution of the burning surface. Once the simulations have been run it is possible to determine the web exposure map, following the approach already explained in the previous paragraphs and schematized also in Figure 27. The web exposure maps with and without the debonding are now compared, and the differences are shown in Figure 46: results obtained for the different positions investigated have been reported for the sake of compactness on the same figure, each of them represented within a box, while in the remaining thermal protection surface there is not any effect and the exposure difference is equal to 0 (blue background). Each of the boxes is connected to a white dot, marking the real position where the content of the box should be located, and contains the exposure increase generated by each debonding position, together with the corresponding color scale ranging from 0 to the maximum value observed. Within each box the blue regions are associated with an exposure increase that is equal to 0, while the surfaces affected by the debonding are marked by other colors, with the dark red associated with the highest value.

The shape of the regions affected by the debonding is significatively different as it can be seen comparing the content of the boxes. The debonding set at $x_{az,\theta} = -16.55°$ (debonding 1, 2 and 3)

presents only one influenced region for each debonding, while debonding set at $x_{az,\theta} = -8°$ (debonding 4, 5 and 6) are characterized by the presence of two (almost symmetrical) influenced regions. This difference is due to the fact that for positions 1, 2 and 3 the combustion surface reaches the debonded surface on one of the two sides of the, while for positions 4, 5 and 6 the combustion surface intersects the debonded surface at its midpoint and from that condition on, two combustion-regression fronts simultaneously spread from the above-mentioned midpoint towards debonding side points.

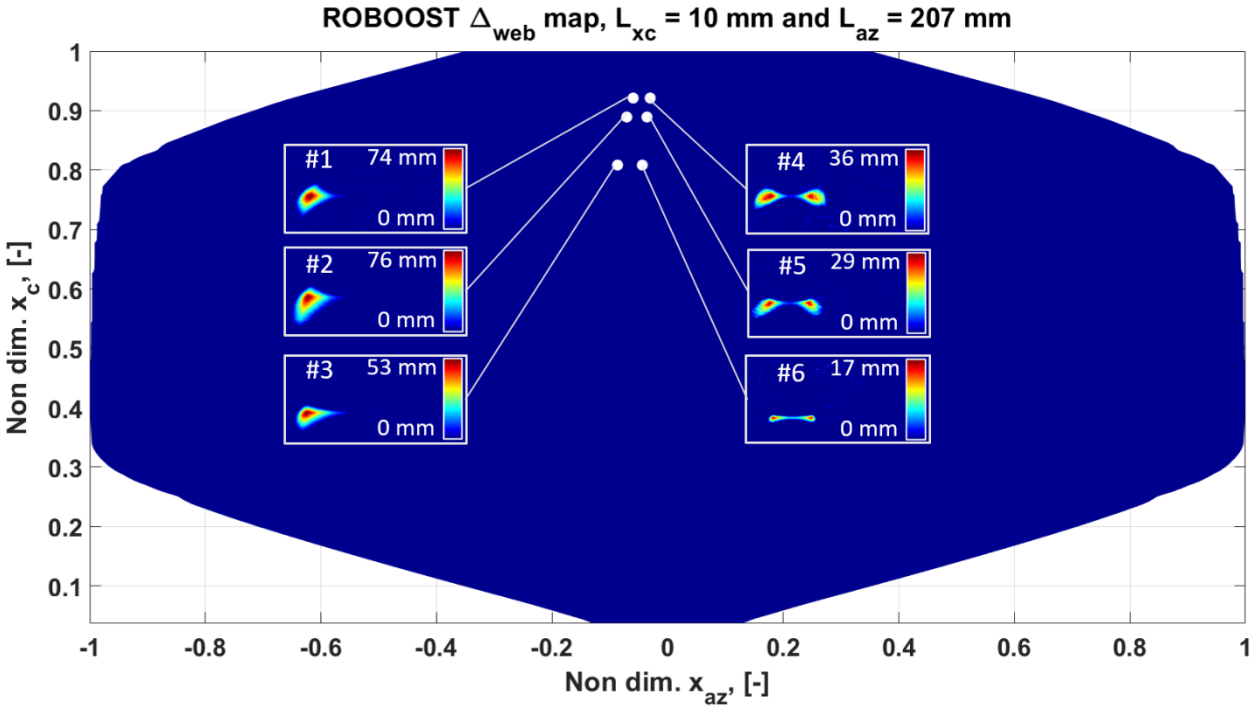

Figure 46: ROBOOST simulations regarding debondings elongated along azimuthal direction.

The maximum exposure increase obtained for each simulation can now be compared with the value that has been determined with the geometrical approach developed in this work, as shown in Figure 47. Solid curves are obtained by representing the exposure increase map (Figure 44) at fixed values of angular azimuthal coordinate ($x_{az,\theta} = -16.55°$ and $x_{az,\theta} = -8°$ for simulations 1, 2, 3 and 4, 5, 6 respectively).

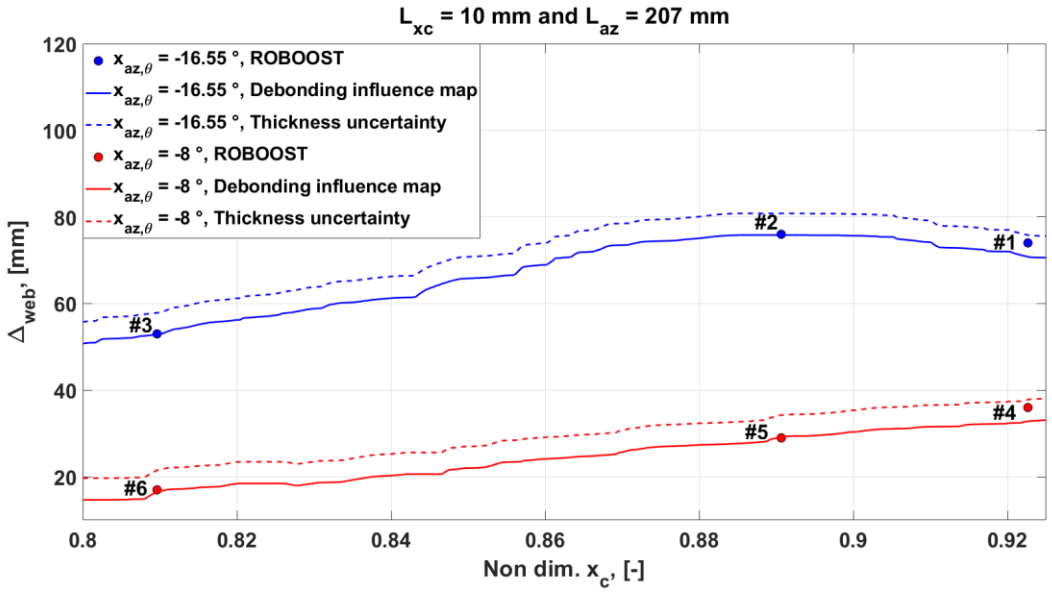

Figure 47: Comparison between ROBOOT results and debonding influence map with debonding main elongation along e_{az}

Figure 47 shows a good agreement between the estimation of the debonding effects evaluated through the methodology developed in this chapter and the exposure increase determined for the 6 simulations run with ROBOOST

Second set of debonding

The same analysis has been performed in the interest of investigating the effect due to debonding elongation along curvilinear coordinate. At this point, the same debonding discussed before is reversed such that $L_{x_c} = 207\ mm$ and $L_{az} = 10\ mm$. On the contrary, the thickness $L_{x_n} = 5\ mm$ is unchanged as well as the angular azimuthal coordinate position ($x_{az,\theta} = -8°$). The debonding influence map (Figure 49) concerning debonding elongation along e_{x_c} is different from the previous one (Figure 45). More in detail, it marks out higher web difference exposure values up to nearly 220 mm with respect to 76 mm of the maximum exposure linked to Error! Reference source not found., meaning that a debonding with $L_{x_c} \gg L_{az}$ is more critical than a debonding with $L_{x_c} \ll L_{az}$ in the case regions of maximum exposure. In Figure 50, since debondings 7,8,10 do not lay on the blue solid curve, they are affected by thickness effect signifying that at those positions the angle between the burning surface and the case is low. However, as discussed before, a conservative prediction can be obtained by simply drifting upward the blue trend of the debonding thickness amount (blue dotted line in Figure 50). Conversely, no thickness effect must be hold for debonding 9, since it belongs to the blue solid curve in a quite satisfactory way.

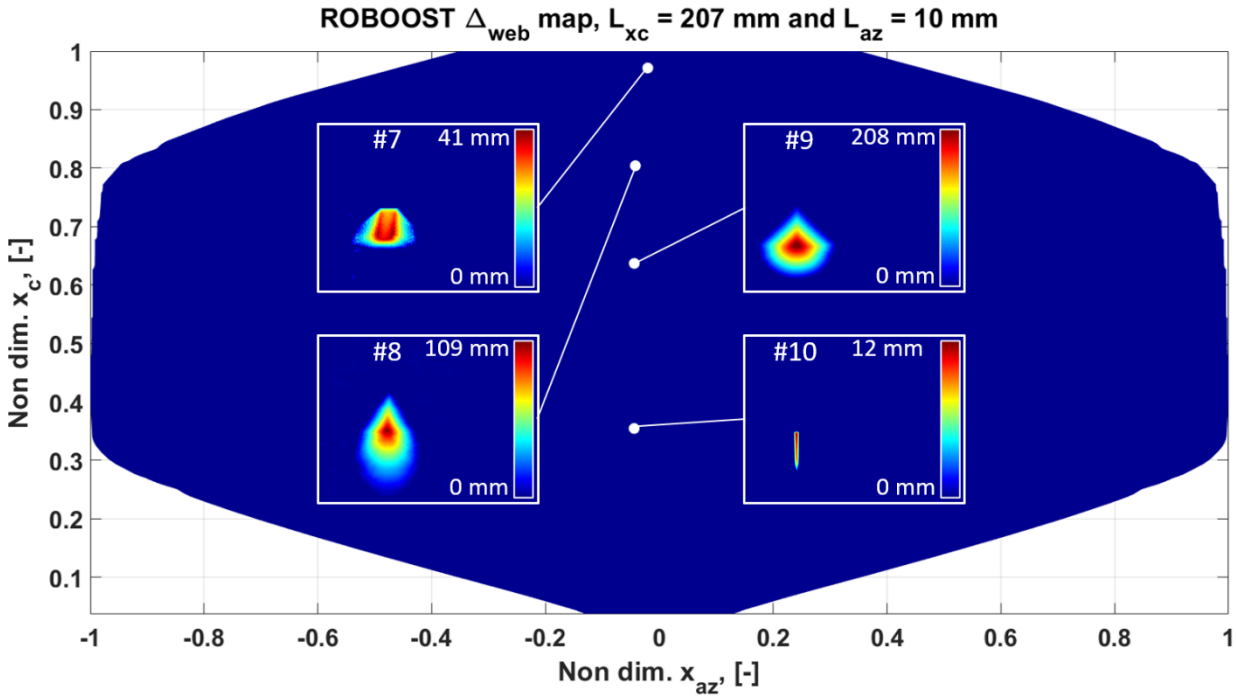

Figure 48: ROBOOST simulations regarding debondings elongated along curvilinear coordinate direction

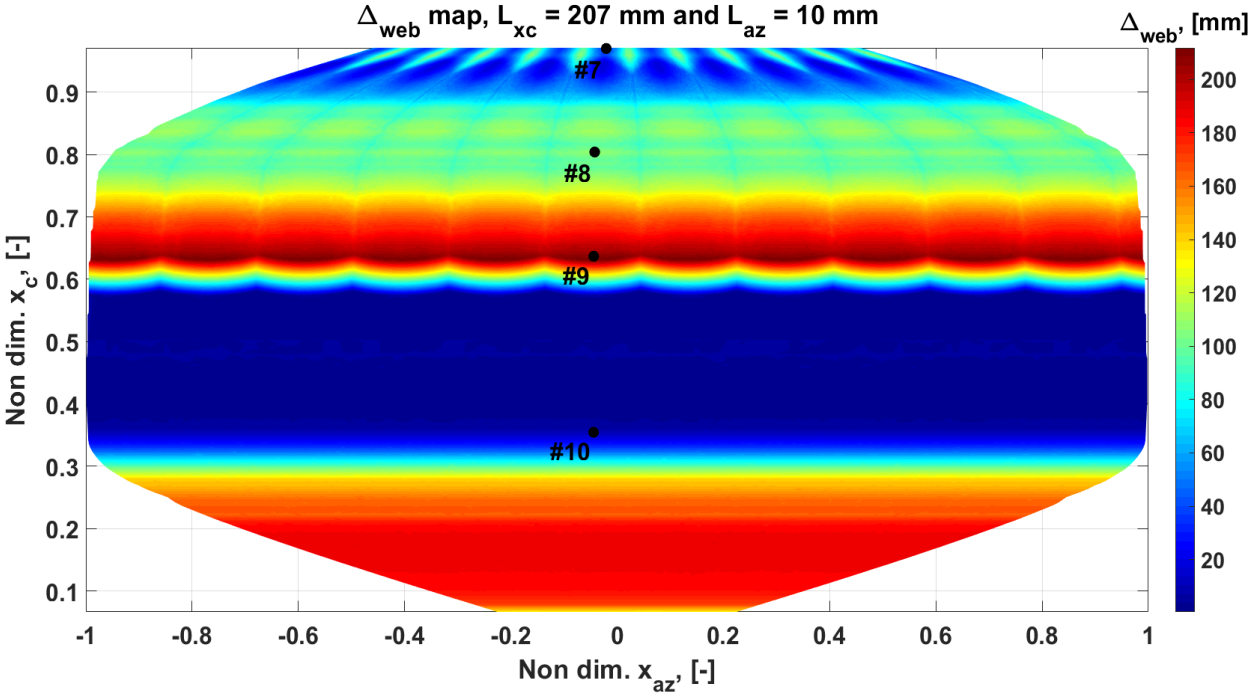

Figure 49: Debonding influence map regarding debonding elongation along e_{x_c}

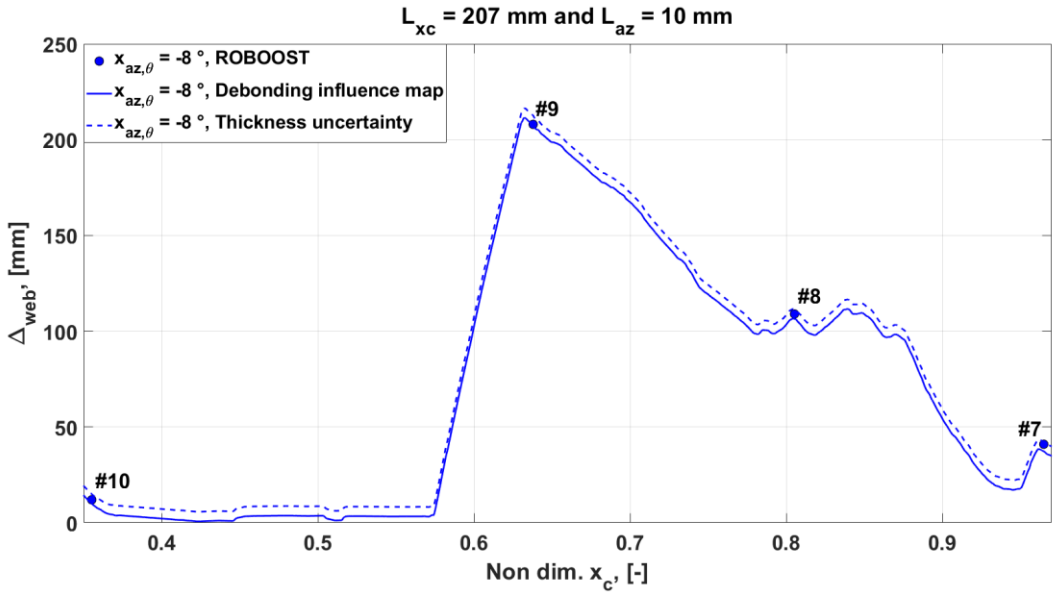

Figure 50: Comparison between ROBOOT results and debonding influence map with debonding main elongation along e_{x_c}

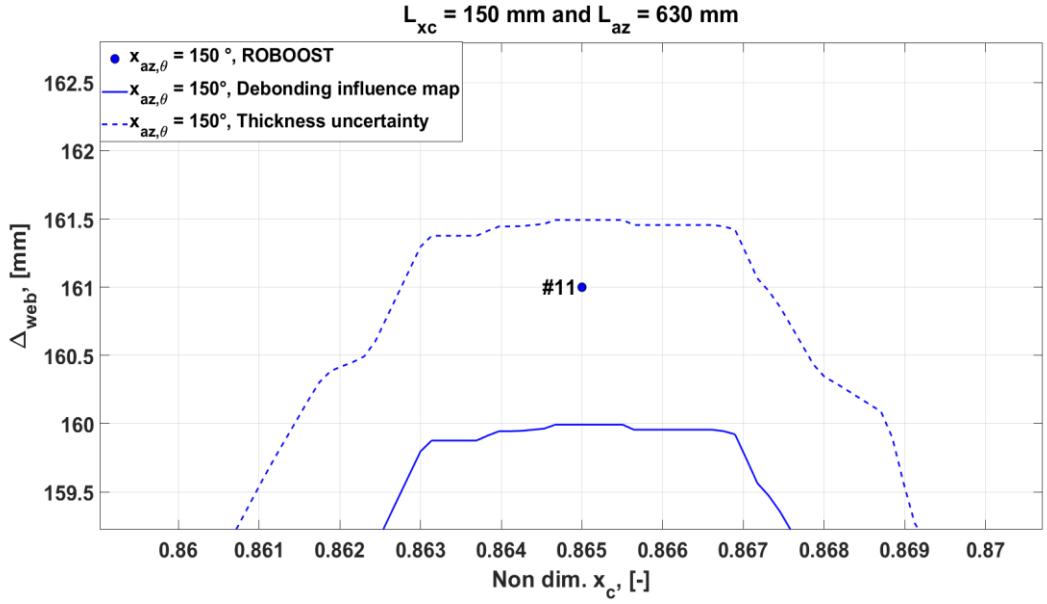

Figure 51: Comparison between ROBOOST result and debonding influence map with debonding elongation along e_{x_c} and e_{az}.

Previous debondings are respectively identified by $L_{x_c}/L_{az} = 0.05$ for the debonding elongated along azimuthal direction and $L_{x_c}/L_{az} = 20.7$. for the debonding developed along the curvilinear coordinate. However, the above-mentioned strategy is also valid for debondings with aspect ratio in between the two limits.Figure 51 regards a debonding with the following dimensions: $L_{x_c} = 150\ mm$, $L_{az} = 630\ mm$ and $L_{x_n} = 1.5\ mm$. The aspect ratio is $L_{x_c}/L_{az} = 0.24$. Since the dotted line and the blue line include the web difference exposure computed with ROBOOST, the novel procedure has been proven to be suitable for the investigation of debondings with different size.

All results previously discussed have been carried out with ROBOOST software installed on a calculator with the following features: 16 Gb RAM, Intel Core i7-7th generation CPU machine with 3.10 GHz and NVIDIA Quadro M1200 graphic card. ROBOOST simulations lasted 24 hours each one., instead debonding influence maps lasted 1 hour each one.

3.5 Conclusions

An original Computer Graphic procedure has been developed with the aim of investigating the influence of cavities and debondings occurrence on SRMs.
First, by means of self-intersection removal algorithm, ROBOOST can produce estimations regarding both pressure variations due to grain cavities and case time exposure of a generically shaped solid rocket motor. First the simulator provided with the abovementioned algorithm has been validated with Z9 SRM, comparing simulated results with experimental data. A quite appreciable error in the range of ±2% is obtained. This allows to evaluate the impact of an assumed cavities distribution on Z9 as combustion chamber pressure variations and case early exposition.
Second, a novel procedure has been introduced to examine the effect of debondings on case-insulating thermal protection material in terms of web difference exposure. Debonding influence maps are obtained from Z9 case exposure map without debondings, generated by ROBOOST. Then, those maps are validated by comparing map results with ROBOOST debonding simulations. Subsequently, debondings elongated along azimuthal direction are analyzed, then debondings extended along curvilinear coordinate direction. It has been shown that the elongation along curvilinear coordinate direction has a larger impact on web difference exposure with respect to elongation along azimuthal coordinate. In the interest of proving the effectiveness and the reliability of the procedure, both the debonding thickness effect and the debonding aspect ratio variation have been evaluated.
Future developments will be focused on the computation of the dihedral angle between the burning surface approaching the case and the case itself with the aim of improving the prediction of debonding thickness influence on web exposure.

References

[1] Sutton, G., P., and Biblarz, O., “Rocket Propulsion Elements,” 7th ed., John Wiley & Sons Inc., New York, 2010

[2] Hoffmann, L. F. S., Bizairra, F., C., P., and Bizairra, J., W., P., “Applied Algorithm in the Liner Inspection of Solid Rocket Motors,” *Optics and Lasers Engineering*, Vol. 102, 2018, pp. 143-153.
https://doi.org/10.1016/j.optlaseng.2017.11.006

[3] Yildirim, H., C., and Ozupek, S., "Structural assessment of a solid propellant rocket motor: Effects of aging and damage," *Aerospace Science and Technology,* Vol. 15, No. 8, 2011, pp. 635-641.
https://doi.org/10.1016/j.ast.2011.01.002

[4] Dhital, D., Lee, J., R., Farrar, C., and Mascarenas, D., "A review of flaws and damage in space launch vehicles: Motors and engines," *Journal of Intelligent Material Systems and Structures,* vol. 25, no. 5, 2013, pp. 524-540.
https://doi.org/10.1177/1045389X13493360

[5] Jan, D., L., Davidson, B., D., and Moore, N., R., "Probabilistic Failure Assessment with Application to Solid Rocket Motors," NASA 19910000996, March 1990.

[6] Wu, S., Lu, Y., Kuo, K., Yang, V., "Anomalous Combustion of Solid Propellant in a Propagating Debond Cavity," AIAA Paper 1992-770, January 1992.

https://doi.org/10.2514/6.1992-770

[7] Andoh, E., "Effect of pressure, initial temperature and propellant ingredients on flame-spreading into a hole," *Combustion and Flame*, Vol. 108, No. 4, 1997, pp. 397-407. https://doi.org/10.1016/S0010-2180(97)81403-4

[8] Hill, P., G., and Peterson, C., R., "Mechanics and Thermodynamics of Propulsion," *Solid Propellant Combustion Chambers*, 2nd ed., Addison Wesley, New York, 1992, pp. 598-600.

[9] Jung, W., Shin, H. and Choi, B., "Self-intersection removal in triangular mesh offsetting", Computer-Aided Design and Applications, vol. 1, n. 1, 2004, pp. 477-484. https://doi.org/10.1080/16864360.2004.10738290

[10] Moller, T., "A Fast Triangle-Triangle Intersection Test", Journal of graphic tools, vol. 2, n. 2, 1997, pp. 25-30. https://doi.org/10.1080/10867651.1997.10487472

[11] Geuzaine, C., and Remacle, J., F., "Gmsh: a three-dimensional finite element mesh generator with built-in pre- and post-processing facilities", International Journal for Numerical Methods in engineering, vol. 79, n. 11, 2009, pp. 1309-1331. https://doi.org/10.1002/nme.2579

[12] Ponti, F., Souhair, N., Mini, S., and Annovazzi, A., "0D Unsteady - 1D Quasi-Stationary Internal Ballistic coupling for ROBOOST simulation tool", AIAA Paper 2019-4140, August 2019. https://doi.org/10.2514/6.2019-4140

[13] Bertacin, R., Ponti, F., and Annovazzi, A., "A New Three-Dimensional Ballistic Model for Solid Rocket Motor Non-Homogeneous Combustion", AIAA Paper 2012-3974, August 2012. https://doi.org/10.2514/6.2012-3974

[14] . Schoner, R., J., "User's Manual Aerotherm Charring Material Thermal Response and Ablation Program," Air Force Rocket Propulsion Laboratory, AFRPL-TR-70-92, April 1970

[15] Moyer, C., B., and Rindal, R., A., "An analysis of the coupled chemically reacting boundary layer and charring ablator. Part 2- Finite difference solution for the in-depth response of charring materials considering surface chemical and energy balances," NASA CR-1061, June 1968

[16] Viganò, D., Annovazzi, A., and Maggi, F., "Monte Carlo Uncertainty Quantification Using Quasi-1D SRM Ballistic Model", International Journal of Aerospace Engineering, vol. 2016, 2016, pp. 1-8. https://doi.org/10.1155/2016/3765796

[17] Ponti, F., Mini, S., and Annovazzi, A., "Numerical Evaluation of the Effects of Inclusions on Solid Rocket Motor Performance," AIAA Journal, Vol. 58, No. 9, 2020, pp. 4028-4036. https://doi.org/10.2514/1.J058735

Chapter 4

4 Investigation of Friedman curl effect

Nomenclature

Latin

a	=	burn rate experimental factor, $\frac{m}{s \cdot bar^n}$
c	=	specific heat, $J/kg \cdot K$
c_p	=	hot gas constant pressure specific heat, $J/kg \cdot K$
D_h	=	hydraulic diameter, m
$F(x)$	=	burning rate increment due to Friedman Curl effect, $[-]$
h_c	=	convective heat coefficient, $W/m^2 \cdot K$
L	=	grain web length, m
N_u	=	Nusselt number, $[-]$
n	=	burn rate experimental exponent, $[-]$
n_x	=	number of spatial points, $[-]$
P_r	=	Prandtl number, $[-]$
p_0	=	combustion chamber pressure, Pa
$\dot{Q}$	=	solid phase reaction specific power, W/m^2
$\dot{q}_{cond}$	=	conductive specific power through propellant, W/m^2
$\dot{q}_{conv}$	=	convective specific power through hot gases, W/m^2
$\dot{q}_{out}$	=	conductive specific power through motor case, W/m^2
r_b	=	propellant burning rate, m/s
$r_{b,ref}$	=	numerically computed average propellant burning rate, m/s
$r_{b,exp}$	=	experimentally determined average propellant burning rate, m/s
T_A	=	propellant activation temperature, K
T_{gas}	=	combustion chamber hot gas temperature, K
T_{PI}	=	initial propellant temperature, K
t	=	time coordinate, s
th_{layer}	=	thickness of low solid particles content layer, $[m]$
tr_{layer}	=	percentual reduction of AP presence in HTPB rich layer, $[-]$
x	=	space coordinate, m
x_{case}	=	case position, m
x_{bs}	=	burning surface position, m

Greek

α	=	thermal diffusivity, m^2/s
α_{HTPB}	=	Hydroxyl-terminated-polybutadiene thermal diffusivity, m^2/s
α_{prop}	=	propellant thermal diffusivity, m^2/s
λ	=	thermal conductivity, $W/m \cdot K$
λ_{CASE}	=	case thermal conductivity, $W/m \cdot K$
λ_{PR}	=	propellant thermal conductivity, $W/m \cdot K$
μ	=	hot gas dynamic viscosity, $Pa \cdot s$

ρ = density, kg/m^3
Φ_{PR} = propellant temperature, K

4.1 Introduction

During tail-off phase of some SRMs, close to the end of the grain combustion, a peculiar phenomenon can be observed: a pressure peak occurs nearly at the end of the combustion process when the burning surface approaches the motor case and just before the sudden drop of the rocket combustion chamber pressure.

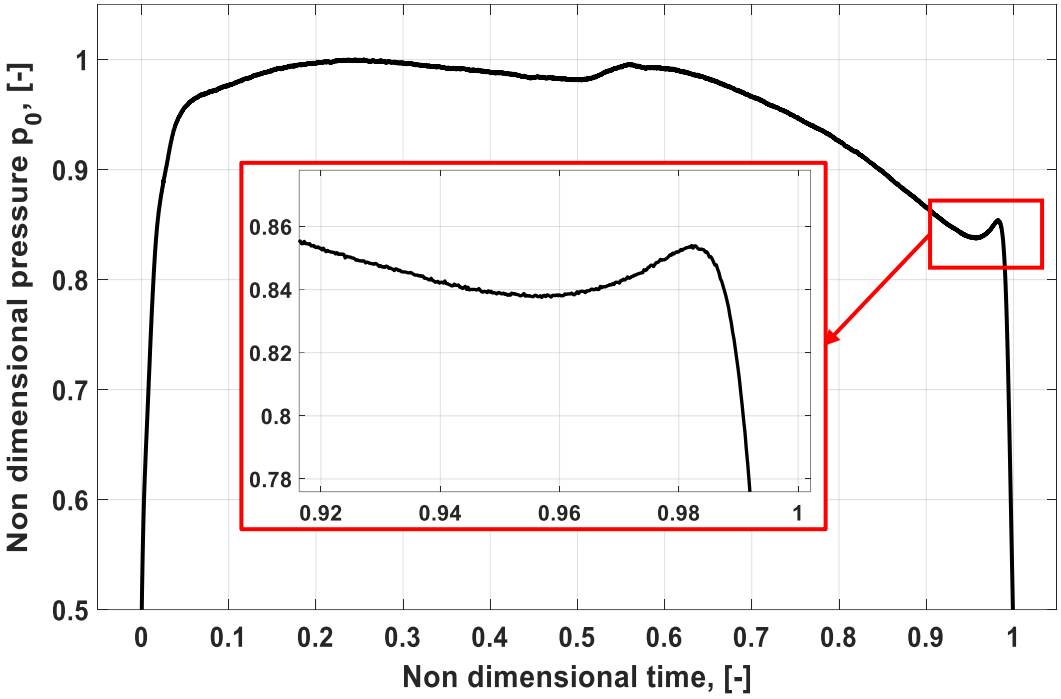

Figure 52: Friedman Curl effect.

The abovementioned peak is the so-called Friedman Curl effect [1], and it is probably caused by a fast increasing of propellant gases mass flow rate. However, in the knowledge of the author, no exhaustive explanation of this phenomenon has been found in literature. The only evidence is that the Friedman Curl effect seems to be linked to burning rate increase due to heat accumulation. That accumulation implies an acceleration of the combustion process because of a local temperature rise [2]. Besides that, a possible motivation leading to heat accumulation can be detected in the thermal diffusivity variation occurring in proximity of the case: indeed, thermal properties change from grain to thermal protection material (or to the liner) or from grain to the metallic case (when case-insulating thermal protections are not used). Specifically, this happens for small-scale test SRMs. More in detail, thermal diffusivity decreases in the radial direction toward the case, affecting the amount of heat propagating through the propellant. The main consequence is a heat redistribution opposite to burning surface regression leading to a burning rate increment. Hence, before the grain is all burned, a combustion acceleration arises implying the manifestation of the Friedman Curl pressure peak before the burn-out pressure drop. That phenomenon also depends on the motor geometry: the pressure rise is exacerbated by a cylindrical geometry with respect to conical one. Theoretically, regarding the former geometry, the grain is all burned out at the same time: this means that all the combustion power produced enhances the intensity of the pressure rise. Concerning the latter, the burn-out time of the combustion depends on the considered section along the motor axis since the burning surface approaches the case in different time instants according to the conical-shaped geometry. Furthermore,

Friedman Curl pressure peak is linked to propellant casting process. Two different cases are considered. First, when the desired propellant configuration geometry is achieved by pushing a mandrel into the case after its filling, there is an evident occurrence of Friedman Curl in experimental pressure profiles [3-4]. Second, when the casting process is obtained by means of simply filling the SRM case after the mandrel has been positioned within the case itself, experimental data do not show any evidence of the pressure peak. The aabove-mentioned statements are even more visible for small-scale motors aimed to model propellant Vieille Law [3-7]. Therefore, in order to perform a more effective characterization of grain burning law, among the other combustion instabilities [5-6], pressure peak influence on the averaged-burning rate procedure should be conveniently compensated. More in detail, Figure 52 shows the combustion chamber pressure profile of a small-scale test motor with a cylindrical shape defining both the external metallic case and the internal grain configuration (Figure 56). No case-insulating thermal protection material, nor liner is used in the SRM manufacturing process: the grain is directly in contact with the metallic case.
In view of the abovementioned description, the present study is aimed to provide a simplified physical model to predict the Friedman Curl effect, analyzing all the influencing factors involved. To achieve that result, the effect of inhomogeneous grain properties next to the case is investigated with the aim of accessing the link between propellant local composition and the local regression rate. Therefore, a 3D model of the burning rate law is required, meaning the possibility to vary the displacement of each point belonging to the burning surface. In past literature, some works show that the burning surface has been discretized as a 2D triangular mesh [8]. Another common approach is the handling of the burning surface using a level-set-method strategy [9-10]. It consists of describing the generic grain cross section with an interface computed as the intersection between a multi-dimensional function, namely level-set function, and a plane. All those methods, although are convenient in terms of computational time, seem to be unsuitable for the following study. A 2D triangular mesh allows the independent motion of burning surface points, but a 3D analysis is required. On the contrary, level set methods are 3D, but they are not able to deal with a point-by-point motion controllability. All those limitations are overcome by ROBOOST (Rocket BOOst Simulation Tool), an internal ballistics simulation software developed in [11]. It relies on a dynamic 3D triangular mesh discretization concerning the SRM burning surface. This allows to evaluate the internal ballistics effect of grain non-uniformities, including ignition transient [15] and tail-off phase [16]. Specifically, the burning rate anisotropy originated by the Friedman Curl effect is applied independently on each mesh point displacement as a variation with respect to the combustion chamber average burning rate.

4.2 Mathematical-physical model

Past literature works have shown how the Friedman Curl effect is strictly coupled to the SRM combustion chamber ballistics [12-14]. In the following, those two parts are firstly introduced separately and only at the end linked together.
In pursuance of modelling the heat conduction across the grain, the following assumptions are established:

- The propellant temperature (ϕ_{PR}) is a function of time (t) and space (x) coordinate only. In particular, the space coordinate is computed as the distance from the initial burning surface position ($x_{bs}(t=0)$).
- Solid phase reaction heat per unit time ($\dot{Q}$) is considered negligible in a first-order approximation [17].
- Material thermal diffusivity (α) depends on spatial coordinate (x) only. No dependance with respect to time or grain temperature is considered.
- At the interface between the SRM combustion chamber and the burning surface the following heat transfer phenomena are considered: heat convection ($\dot{q}_{conv}$) driven by combustion

chamber hot gases temperature, and conduction ($\dot{q}_{cond}$) involving the heat spread through the grain.

- Combustion chamber hot gases temperature (T_{gas}) is considered constant in time and space.
- Radiative heat transfer from combustion chamber to burning surface is neglected.
- Thermal diffusivity is isotropic but non-homogeneous in space.

The abovementioned hypotheses validate the usage of the heat equation (Eq. (1)) in its classical expression.

$$\frac{\partial \phi_{PR}(t,x)}{\partial t} = \alpha(x)\frac{\partial^2 \phi_{PR}(t,x)}{\partial x^2} + \frac{\partial \alpha(x)}{\partial x}\frac{\partial \phi_{PR}(t,x)}{\partial x} + \dot{Q}, \qquad \alpha(x) = \frac{\lambda}{\rho \cdot c} \tag{1}$$

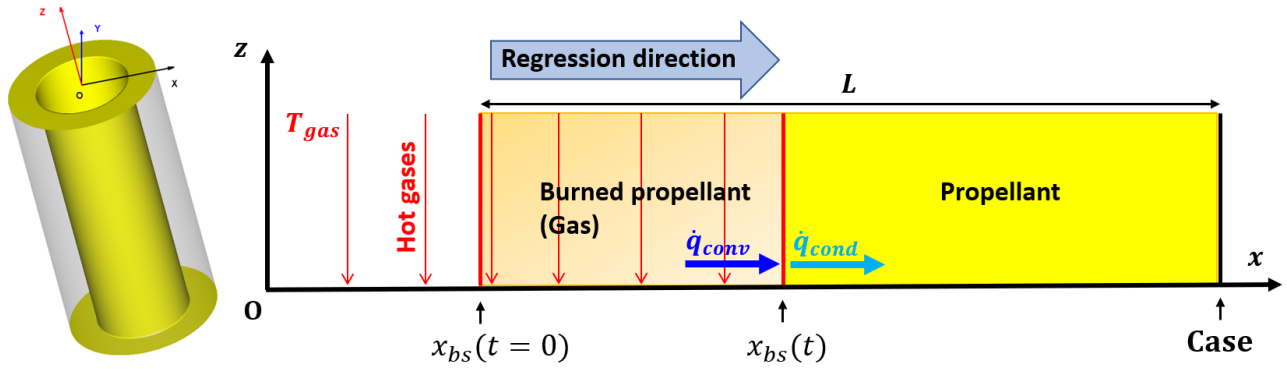

Figure 53: Grain heat transfer model.

Figure 53 focuses on the theoretical model used in the present work. At the initial time instant ($t = 0$), the hot gases, produced by the igniter, are considered at their stationary maximum temperature (T_{gas}) which is in the same order of magnitude of the one linked to grain combustion gases. When the propellant ignition process is completed, the burning surface starts its recession motion, shifting from the initial position $x_{bs}(t=0)$ to the new position $x_{bs}(t)$ at time instant t. The distance displaced by the burning surface depends essentially on two phenomena. First, the amount of convective power ($\dot{q}_{conv}$) produced by the hot gases flowing near the burning surface is the primary driver of the propellant depletion, since the more is the convection heat transferred to the grain, the more is the increase of the burning rate. Second, there is a link with the propellant local combustion layer. Indeed, three different zones develop, each one identified by its specific propellant thermal state. Starting from the virgin grain proceeding in the direction of the burning surface, a first solid region occurs where a progressive degradation of grain components takes place due to the action of exothermic reactions. An intermediate layer, between the previous one and the closest region to the burning surface, consists of a two-phase mixture between liquid melted propellant and evaporated gas compounds. Finally, the third layer next to the burning surface is a gaseous-phase region where chemical reactions develop decomposing gas species into other gaseous compounds according to the incoming convective power. Only heterogeneous models are able to deal with the abovementioned grain combustion stratification; however, they imply a high degree of complexity, and hence a large amount of computational time since all reactions need to be modelled and chemical products concentrations to be tracked [18]. The present work considers a simplified combustion model (Eq. (2)) based on grain activation temperature (T_A) as a threshold intended to determine propellant layer ignition.

$$\phi_{PR} = \begin{cases} \phi_{PR}, & \phi_{PR} < T_A \\ T_{gas}, & \phi_{PR} \geq T_A \end{cases} \tag{2}$$

By means of Eq. (2), combustion is modelled as an instantaneous propellant gasification once activation temperature is reached. Hence, combustion products are immediately brought to the same temperature of combustion chamber hot gases. Furthermore, Eq. (2) has another important implication: since the propellant combustion zones and the gas region are not involved in the model, Eq. (1) applies only to the propellant domain, without regarding of the combustion chamber except for the convective heat exchange. Besides that, to obtain the numerical solution of Eq. (1), one initial condition (Eq. (3)) and two boundary conditions (Eqs. (4-5)) are fundamental since Eq. (1) is a parabolic PDE (Partial Differential Equation).

$$\phi_{PR}(t = 0, x) = T_{PI} \tag{3}$$

$$h_c \left(T_{gas} - \phi_{PR}\big(t, x = x_{BS}(t)\big)\right) = -\lambda_{PR} \left.\frac{\partial \phi_{PR}}{\partial x}\right|_{t, x = x_{bs}(t)} \tag{4}$$

$$\dot{q}_{out} = -\lambda_{CASE} \left.\frac{\partial \phi_{PR}}{\partial x}\right|_{t, x = L} \tag{5}$$

Regarding Eq. (4), the left -hand side term models the convective power ($\dot{q}_{conv}$) transferred from combustion chamber hot gases to the grain burning surface. It must be highlighted that the burning surface position (x_{BS}) varies with time, therefore implying a dependance of convective power from burning surface position too. Indeed, Eq. (4) is a Robin boundary condition moving along space direction x: the grain depletion can be considered the main factor leading to the burning surface moving in time along x. Furthermore, the right-hand side term is linked to the conductive power ($\dot{q}_{cond}$) through the propellant. The balance between the convective and the conductive power drives the rise of the grain layer temperature at the interface with the combustion chamber: once it reaches a value larger than the activation temperature (Eq. (2)), the layer gasifies at a temperature in the same order of magnitude of the temperature characterizing the hot gases. Equation (5), namely a Neumann-type boundary condition, applies to the power exchange between the grain and the SRM metal case. More in detail, the external environment exchanging heat with the case, is considered at standard temperature level. Finally, Eq. (6) is the direct consequence of the burning surface motion in time: the burning rate is conveniently computed as the instantaneous velocity of the moving interface.

$$r_b = \frac{dx_{BS}}{dt} \tag{6}$$

To sum up, Eq (1) to Eq (6) represent the mathematical core of the "simplified" procedure to estimate the Friedman Curl effect. However, a deeper attention is needed in the direction of obtain the solution in terms of propellant temperature maps varying in time and space, and in terms of burn rate distribution along x direction. Figure 54 shows the heat equation model flowchart to determine the abovementioned solutions. Since no experimental data are normally available regarding heat transfer convective coefficient values (h_c), an iterative procedure is established to estimate such values.

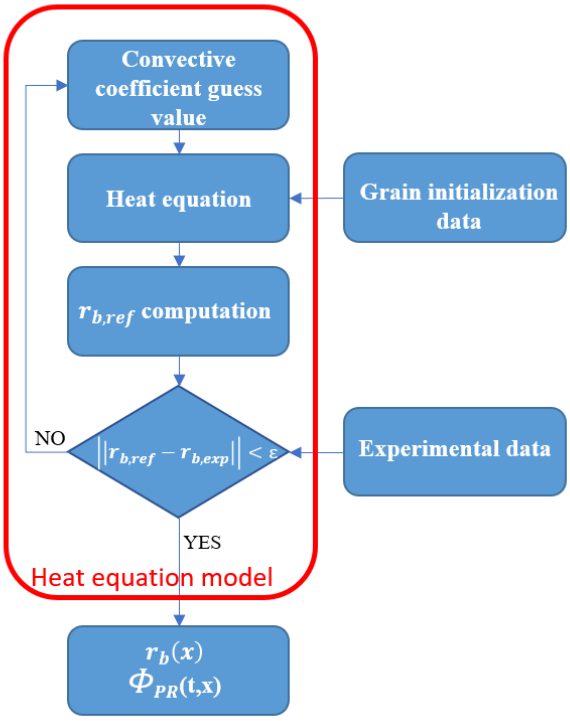

Figure 54: Heat equation model flowchart.

As a first step, an initial guess value is introduced. Then, the equations system (Eq. (1) to Eq. (6)) is correctly initialized with grain thermal properties values (HTPB and grain thermal diffusivity, grain thermal conductivity, HTPB layer thickness, grain activation temperature, grain initial temperature, combustion chamber hot gases temperature), and hence it is numerically solved computing the average burning rate ($r_{b,ref}$). If that value is equal to the experimental average burning rate (the experimental average burning rate corresponds to the burning rate averaged within the quasi-steady state phase of combustion) less than a user-defined tolerance ε, the convergence criterion is satisfied, and the solution is considered acceptable. On the contrary, if the match between the two burning rates values is not enough accurate with respect to the tolerance ε,the entire procedure is repeated. However, it must be highlighted that up to now h_c evaluation relies on the convergence to experimental burning rate. Thus, an acceptance test is needed in the interest of checking the consistency with the numerical solution and the estimation from literature formulas. To this aim, the following empirical relation (Eq. (7)) has been chosen [19]:

$$h_c = \mu \frac{c_p \cdot N_u}{P_r \cdot D_h} \tag{7}$$

Equation (1) is evaluated using the finite difference technique. Space derivatives are discretized with a centered three-point stencil with an accuracy of the 2nd order (Figure 55a, where $m-1$index identifies the position of the present time instant).For equations (4) and (5) a forward (Figure 55c) and backward (Figure 55b) three-point scheme is respectively established, since the two boundary conditions subsist at the borders of the space domain implying that a centered stencil is no longer directly exploitable. On the other hand, time derivatives are modelled using an intermediate approach between Backward Euler approximation (1st order accuracy) and Crank-Nicholson procedure (2nd order accuracy) (respectively visible in Figure 55). That strategy consists of exploiting the Theta

method [20], where the Theta parameter, varying between 0 and 1, let the user control the numerical accuracy moving from the 1st order accuracy of the Backward Euler procedure

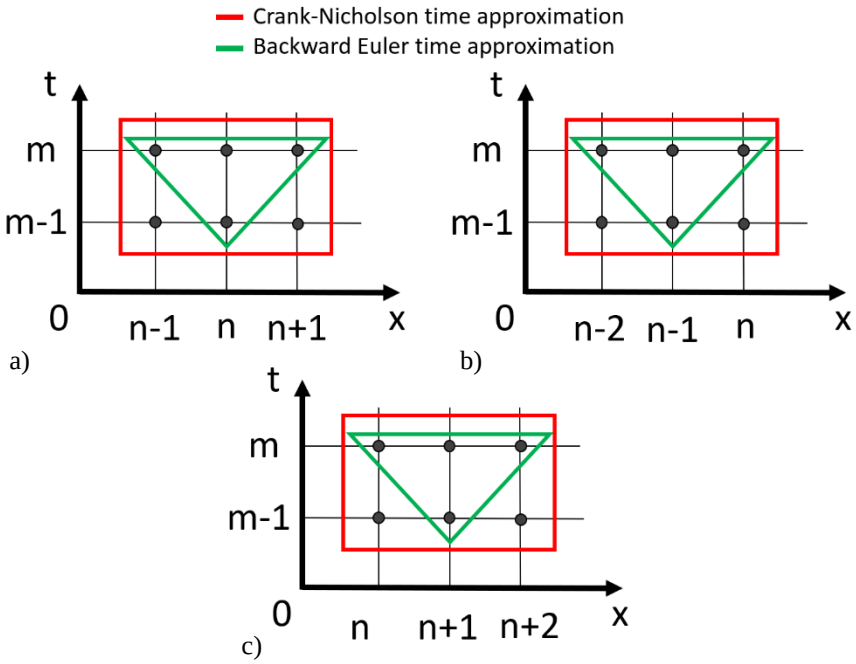

Figure 55: Finite difference stencil.

to the 2nd order accuracy of the Crank-Nicholson one. The main advantage is the capability to overcome numerical instabilities arising from the occurrence of some eigenvalues in the unstable region but maintaining the solving scheme as much as possible close to a high degree of accuracy. The time step selected is $7.5 \cdot 10^{-6} s$. The spatial step value and convergence will be discussed in Subchapter 4.3.

As mentioned at the beginning of Subchapter 4.1, Friedman Curl effect is essentially driven by the SRM internal ballistics. Thus, the abovementioned heat equation model must be coupled to the grain combustion main law, namely the empirical Vieille correlation [21]. In view of that, a coefficient ($F(x)$) regarding grain heat propagation process only, is assumed as a correction value of the Vieille law (Eq. (8)).

$$r_b = a \cdot p_0^n \cdot F(x) \tag{8}$$

That coefficient is defined as the ratio between the local burning rate (computed through the heat equation model) and the average one ($r_{b,ref}$). To sum up, the overall burning rate now depends both on the effect of the combustion chamber pressure (p_0) and on the burning rate increase due to heat accumulation ($F(x)$). That correction is included in ROBOOST for each burning surface mesh vertex: indeed, ROBOOST software is based on mesh point-by-point motion which lets the association of the propellant local heating process to the different pressure values within the motor combustion chamber.

4.3 Numerical results

Simulations aimed to evaluate Friedman Curl effect are accomplished on three different sets of Baria SRMs (high pressure, medium pressure, and low pressure (Figure 56). In general, Baria are small-scale rockets used to characterize propellant ballistics properties. From a practical perspective,

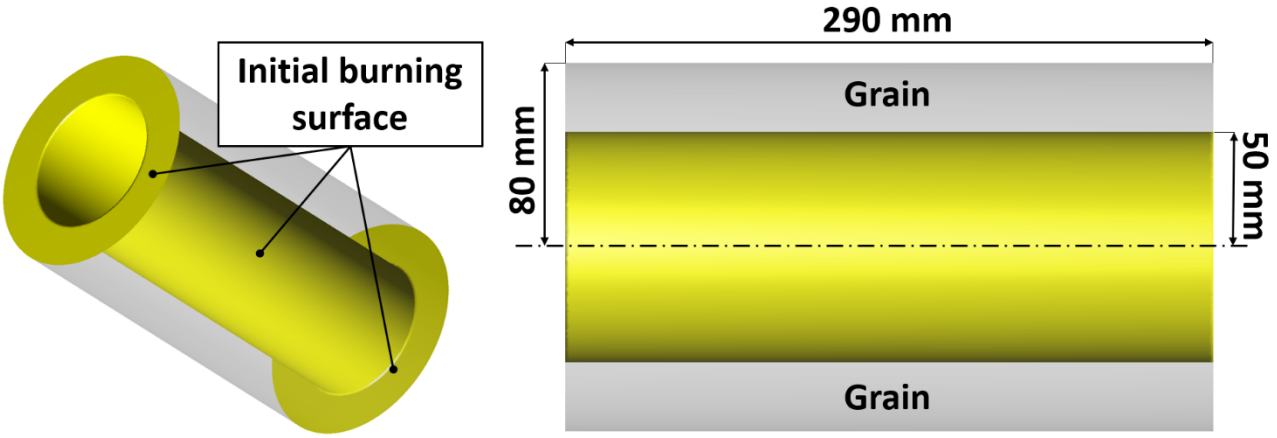

Figure 56: Baria motor, [3].

this corresponds to the determination of the parameters a and n (Eq. (8)) which uniquely identifies the Vieille law for a specific propellant composition. The manufacturing of Baria in terms of propellant casting consists of filling the metallic case with composite propellant (oxidizer: Ammonium Perchlorate (AP); fuel: aluminum powder (Al); binder: Hydroxyl-Terminated-Polybutadiene (HTPB)). Then, a cylindrical-shaped mandrel is pushed in by a piston to obtain a circular propellant geometry configuration. Several sets of Baria are produced to identify each batch of propellant. In view of that, it must be highlighted that Barias of each set are the same except for the throat diameter which represents the only element of difference. In fact, different throat diameters lead to different pressure values in the combustion chamber, and therefore different burning rates for the same propellant composition. By graphing each set pair combustion chamber pressure – burning rate, Vieille parameters a and n are unequivocally determined. In the present study, it has been chosen a propellant composition such that $a = 0.004102\ \frac{m}{s \cdot bar^n}$ and $n = 0.39$ [3]. From a theoretical perspective, BARIA propellant casting process relies on a double-phase fluid dynamics, where the binder (HTPB) represents the liquid part while the oxidizer (AP) together with the fuel (Al powder) are solid particles. The propellant macroscopic behavior, characterized by a different distribution of shear stresses along grain spatial directions [22], is analogous to a shear thinning flow [23]. When the mandrel is pushed in, shear stresses increase near the wall, implying a rapid decrease of the flow dynamic viscosity and affecting the velocity field. The main macroscopic consequence is the propellant rise in the regions next to the metallic case [24]. On the other hand, from a microscopic point of view, solid particles of ammonium perchlorate and aluminum powder show the tendency to migrate in the direction of low shear stress regions of the flow domain, resulting in a particle segregation phenomenon. Because of high stress region close to the case wall, a HTPB rich layer occurs next to the case [23].

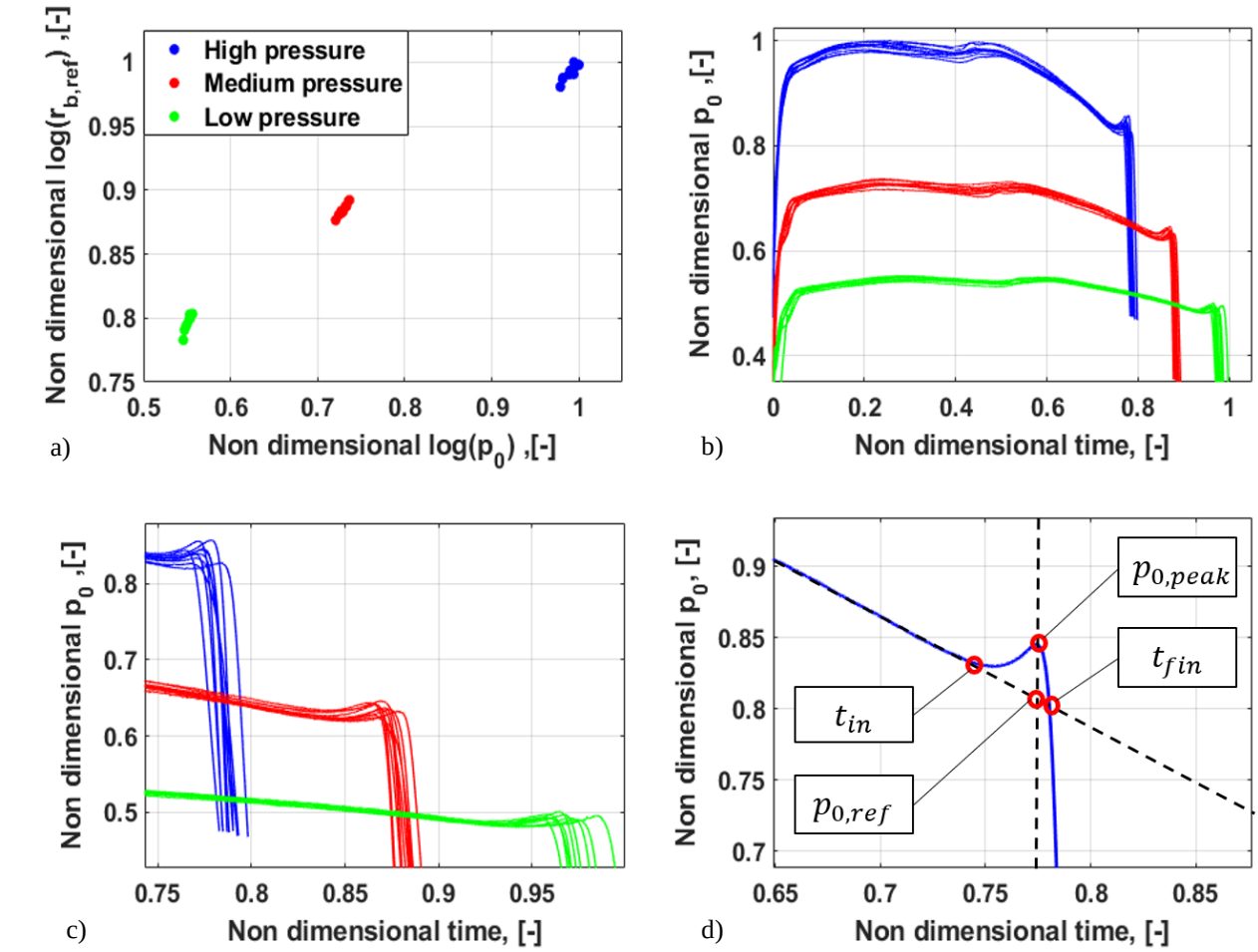

Figure 57: Experimental data.

Figure 57 collects experimental data of three BARIA sets, where the Friedman Curl pressure peak is visible in the tail-off phase (Figure 57b, c). Since, as marked before, high stresses close to the case give rise to large solid particles migration, it is assumed the presence of a HTPB layer separating the case from the propellant with homogeneous composition, while the binder is still liquid. Subsequently this configuration is "frozen" once the binder vulcanization process has been completed. Hence, in the radial direction from the motor axis to the case, material properties change from those associated to the propellant homogeneous in its composition to a propellant with a lower content of AP solid particles. This properties variation is described in the following study by introducing two parameters: th_{layer} (thickness of low solid particles content layer) and tr_{layer} (percentual reduction of AP presence close to the motor case). The fundamental implication is the variation of propellant thermal properties along the spatial direction x. More in detail, material thermal diffusivity assumes propellant typical values far from the case while values regarding low AP propellant next to the case. In consideration of the fact that propellant and pure HTPB have respectively their own diffusivity (α_{prop} and α_{HTPB}), close to the BARIA wall the thermal diffusivity can be computed as a linear combination of the two aforementioned diffusivities (Eq. (9)).

$$\alpha_{prop}\left(1 - tr_{layer}\right) + \alpha_{HTPB} tr_{layer} \tag{9}$$

The transition from α_{prop} to the new thermal diffusivity value (the one expressed by Eq. (9)) is modelled by considering a second-degree polynomial (Eq. (10)) which guarantees a smooth transition from $x = x_{case} - th_{layer}$ (the point at which the propellant-HTPB transition occurs) to $x = x_{case}$ (the coordinate identifying the case position).

$$\alpha(x) = a_0 + a_1 x + a_2 x^2, \qquad x \in [0, x_{case}] \tag{10}$$

The polynomial coefficients a_0, a_1, and a_2 are computed by means of the following conditions (Eqs. (11) to (13)).

$$\alpha_{prop} = \alpha\left(x = x_{case} - th_{layer}\right) \tag{11}$$

$$\alpha_{prop} - tr_{layer}(\alpha_{prop} - \alpha_{HTPB}) = \alpha(x = x_{case}) \tag{12}$$

$$\left.\frac{d\alpha}{dx}\right|_{x=x_{case}-th_{layer}} = 0 \tag{13}$$

As already mentioned in the present subparagraph, the BARIA propellant involved in this work is a composite propellant of the type AP-HTPB-Al. Specifically, HTPB 1814 composition has been examined. It contains aluminum powder which is influenced by aging of micro and nano aluminum particles([25]). HTPB 1814 consists of 18% of aluminum powder, 14 % of HTPB and 68 % of ammonium perchlorate. All those values are expressed in mass percentages. Moreover, HTPB 1814 has been chosen among the other propellant compositions, since it is used to investigate Ariane 5 boosters behavior in subscale testing, thus corresponding to the propellant of experimental curves (Figure 57). With the aim of determining grain thermal properties, HTPB and AP diffusivities are obtained through temperature-varying curves ([26]), by fixing the same reference temperature for both the cases. Concerning aluminum powder, since the presence of an oxide layer decreases on micro-seized particles surface decreases the overall aluminum conductivity [27], the right conductivity value that must be accounted for is 47 $^{W}/_{m \cdot K}$, far from the regular aluminum conductivity of 237 $^{W}/_{m \cdot K}$. Aluminum specific heat has been established equal to 900 $^{J}/_{kg \cdot K}$, since the specific heat is minimally affected by the occurrence of oxide. Mixture properties, grain thermal conductivity and specific heat, are carried out by volume averaging the appropriate value for each grain component [28, 29]. Densities of aluminum, ammonium perchlorate and HTPB are respectively the following ones: 2700 $^{kg}/_{m^3}$, 1950 $^{kg}/_{m^3}$ and 920 $^{kg}/_{m^3}$. Starting from those density values, overall grain density is also estimated using volume fraction average approach, in coherence with all other mixture grain properties. The final outcome linked to grain properties results is 5.7 $^{W}/_{m \cdot K}$ for thermal conductivity, 2000 $^{J}/_{kg \cdot K}$ for specific heat, 1760 $^{kg}/_{m^3}$ for the overall density, and $1.6 \cdot 10^{-6}$ $^{m^2}/_{s}$ for the thermal diffusivity (Eq. (1)). Considering that thermal diffusivity is directly linked with the heat spreading rate within the material and that HTPB diffusivity is in the order of $5.4 \cdot 10^{-8}$ $^{m^2}/_{s}$, heat spreads slower in the HTPB rich layer than in the other regular-composition propellant regions. Thus, heat accumulation occurs near the metallic case zone because of the large difference between grain thermal diffusivity and HTPB thermal diffusivity.
Regarding the evaluation of th_{layer} and tr_{layer}, the first step depends on the computation of the average value of the pressure peak and the time window at which Friedman Curl effect appears. Those

value, respectively $^{p_{0,peak}}/_{p_{0,ref}}$ and $^{t_{in}}/_{t_{fin}}$ are carried out from experimental data (Figure 57a,b,c for "high pressure" BARIAs set). Second, an investigation is performed on th effects of variation of th_{layer} and tr_{layer}: for each pair of th_{layer} - tr_{layer}, a pair $^{p_{0,peak}}/_{p_{0,ref}}$ - $^{t_{in}}/_{t_{fin}}$ is determined using the internal ballistics simulator ROBOOST (Figure 58).

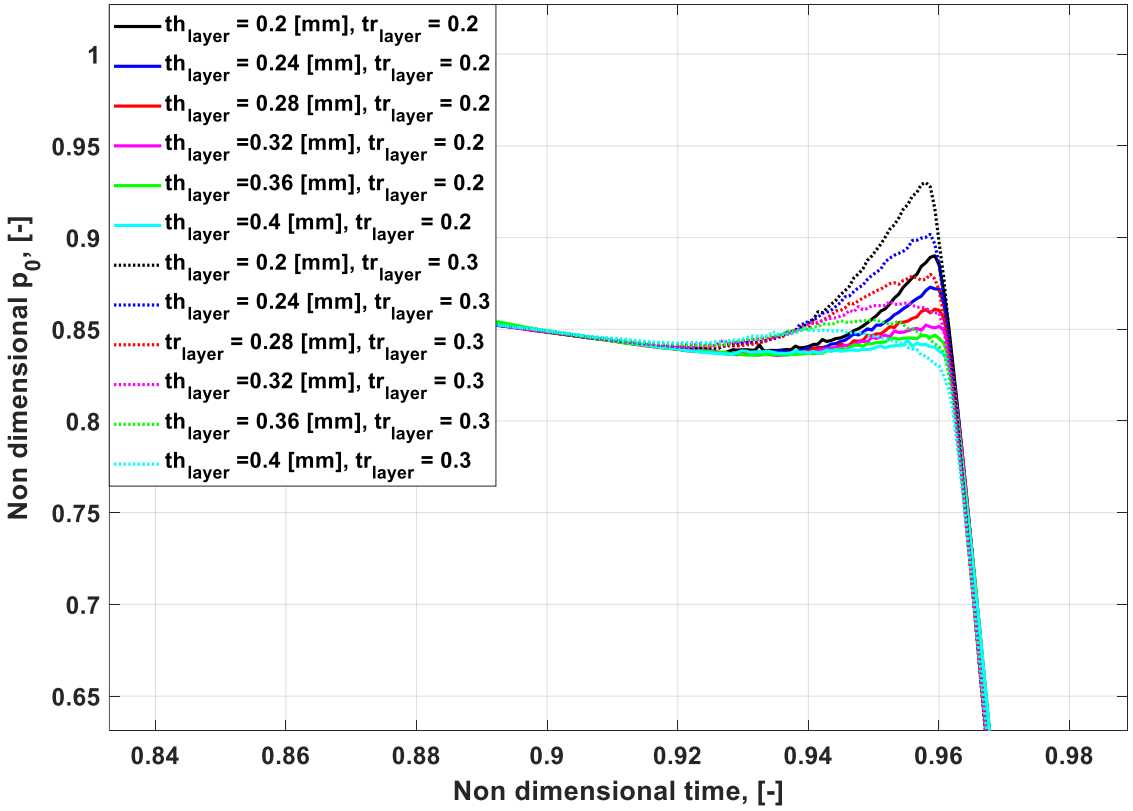

Figure 58: Sensibility analysis on combustion chamber pressure curves.

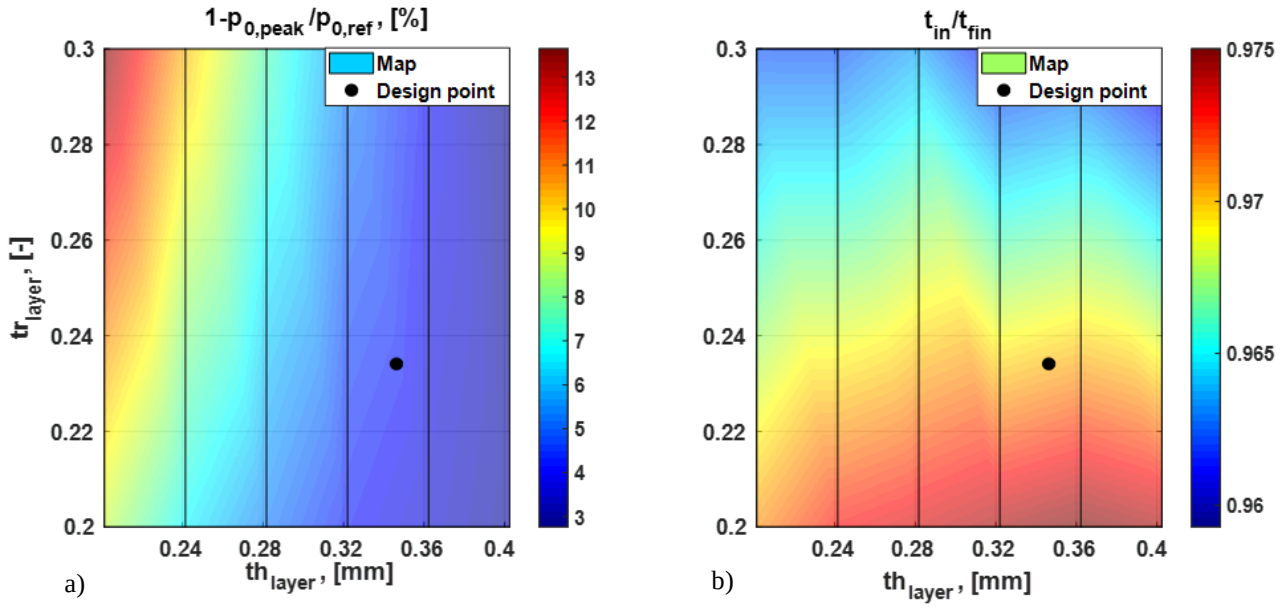

Figure 59: Sensibility analysis maps.

The optimum condition in terms of th_{layer} - tr_{layer} fitting the Friedman Curl pressure peak of "High pressure" Barias set (Figure 57) is: $th_{Layer} = 0.345\ mm$ and $tr_{Layer} = 0.234$ (Figure 59).

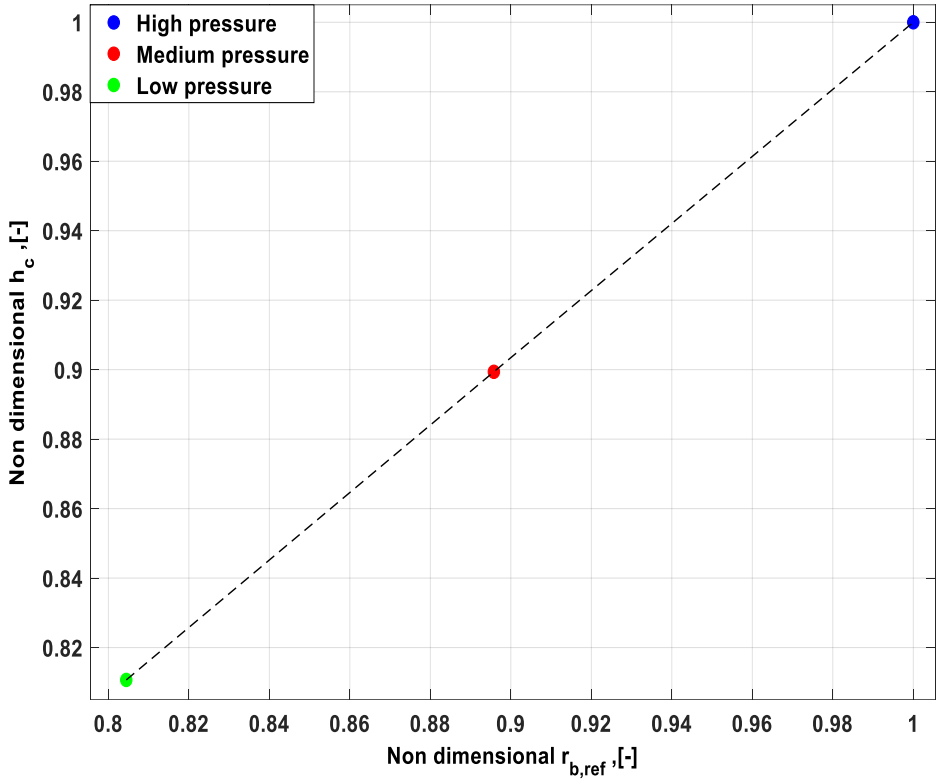

Figure 60: Burning rate - convective heat coefficient for each BARIA pressure level set.

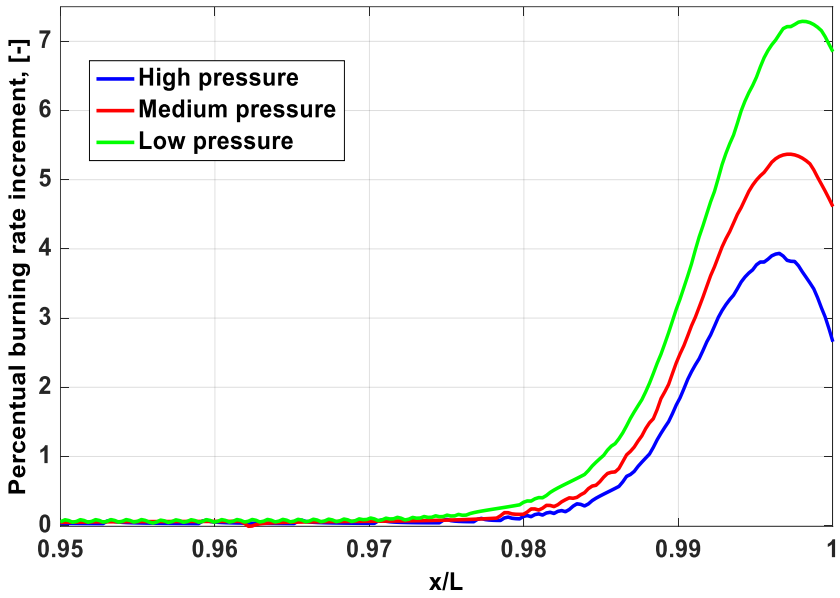

Figure 61: Burning rate increase close to the BARIA case.

At this point, with the same initialization parameters except for the convective heat coefficient (its variation deals with Barias combustion chamber pressure values), the same procedure is applied to each experimental pressure/burn rate condition. With reference to h_c variation, Figure 60 displays the correspondence between Baria burning rate level and its convective coefficient: indeed, the highest h_c is linked to the largest value of burning rate, and therefore of combustion chamber pressure. The trend can be considered acceptable since the grain combustion increases consequently to the amount of heat released by hot gases. For each Baria pressure level set, the percentual burning rate increment starts to rise at $^{x}/_{L} > 0.97$, where due to the higher insulation, the AP poor layer causes a heat accumulation, corresponding to a faster burning (Figure 61).In addition to that, each Baria set burning rate profile reaches a different maximum level: at the same time, at a low burning rate (green curve,Figure 61), the thickness of the unburned propellant is larger with respect to the residual thickness linked to high burning rate (blu curve,Figure 61). Thus, taking into account that the burning surface receeds slowly with a low burning rate, the amount of heat accumulation in the unburned propellant is larger with respect to the heat stored in the case of a larger burning rate. As follows, the low pressure green curve (Figure 61) reaches the maximum level among the three Barias set profiles. After the peak, each of the three colored curves show a quite rapid decreasing: at this point all the pure propellant is burned, so AP poor layer close to the case starts to prevail by lowering the burning rate.

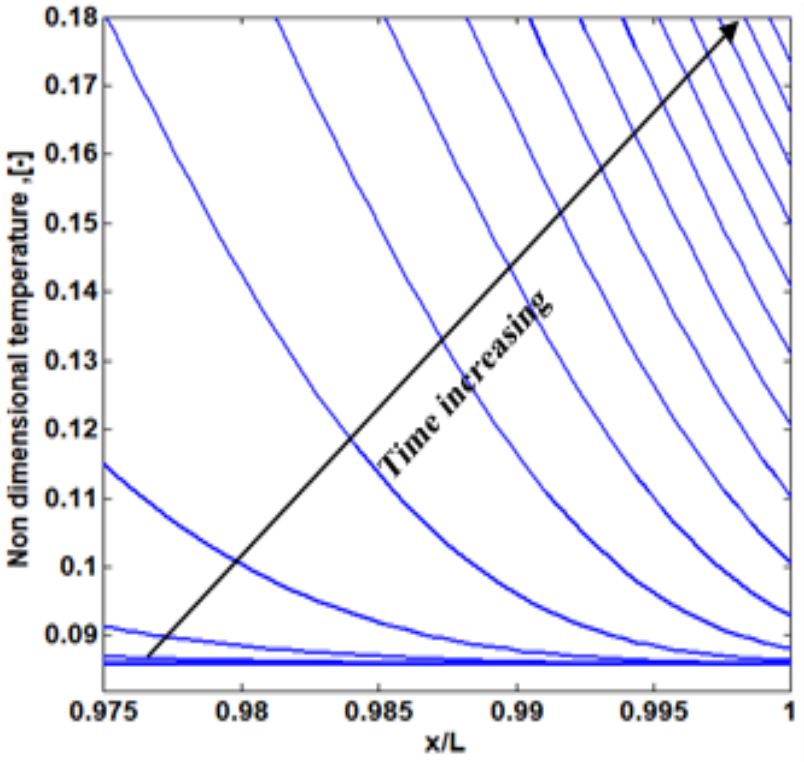

Figure 62: Grain temperature evolution next to the Baria case at high pressure level.

The aforementioned behavior is proved by grain temperature pattern next to the case (Figure 62). Each blue curve (Figure 62) refers to evenly spaced time instants. While the time increases, the burning surface approaches the case: the slope of the temperature pattern increases in time because of thermal diffusivity reduction (HTPB rich layer with a low content of solid particles while approaching the case). In view of that, the burning rate, namely the ratio between space increment and time increment (Eq. (6)) diminishes as marked in the previous paragraph while discussing Figure 61. At the same burning surface position (Figure 63), the high pressure blu curve has the largest slope due to the highest power level transferred to the grain. The opposite is valid for the green curve, where the temperature is identified by a slow increase in time due to the lowest amount of heat driven by the lowest heat transfer convective coefficient value (Figure 60).

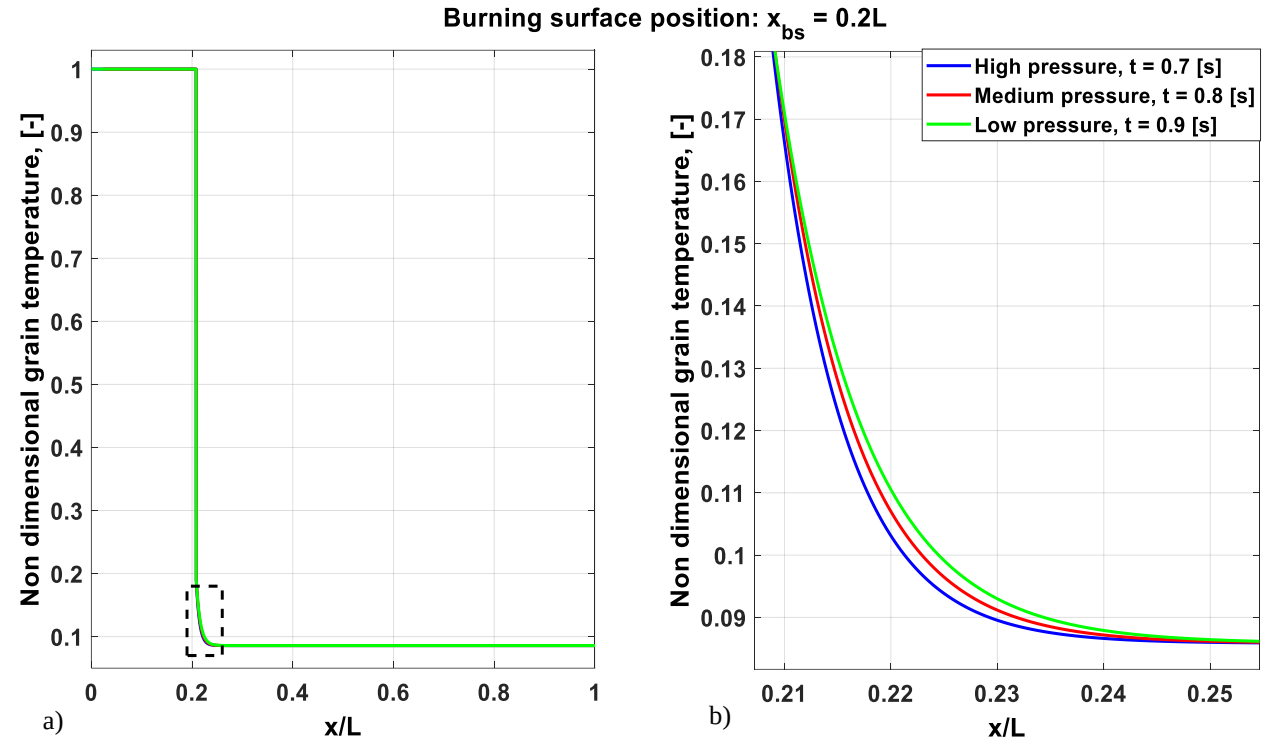

Figure 63: Grain temperature profiles for different pressure conditions.

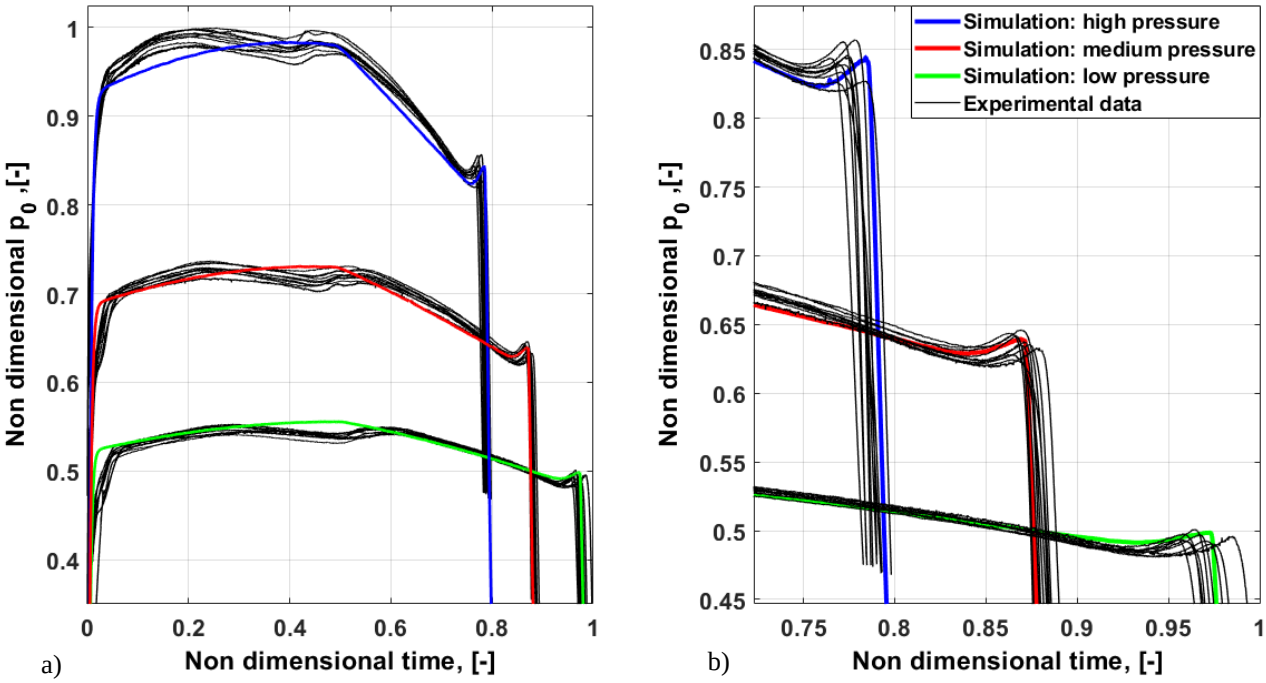

Figure 64: Comparison between simulations and experimental data.

The main result of the present work is displayed by Figure 64. Regarding experimental curves, it is possible to identify a dip in pressure in the range $0.4 \div 0.5$ of the non-dimensional time, and a pressure peak close to tail-off.

The former is due to propellant casting process leading to migration of AP/Al particles toward low shear stress region. Indeed, when the burning surface crosses a grain region characterized by a large amount of such solid particles, the burning rate increases leading to and increment of the combustion chamber pressure (in the range $0.2 \div 0.3$ of the non-dimensional time). Subsequently, a solid particle lean region occurs leading to a decrease of burning rate and consequently of pressure. The above-mentioned statement justifies the pressure dip observed in Figure 64.
The latter is the Friedman Curl pressure peak. The comparison between the experimental Friedman Curl pressure peaks and the simulated ones is quite acceptable for every pressure level condition, meaning that the Friedman Curl effect mainly relies on burning rate increasing in time.
Furthermore, other parameters are needed to numerically solve Eq. (1). Among them, there are initial grain temperature $T_{PI} = 293.15\ K$, combustion chamber hot gases temperature $T_{gas} = 3400\ K$ [14], and grain activation temperature $T_A = 650\ K$ [30]. Spatial grid dependance analysis has been performed (Figure 65) in order to quantify the numerical convergence of the mathematical model.

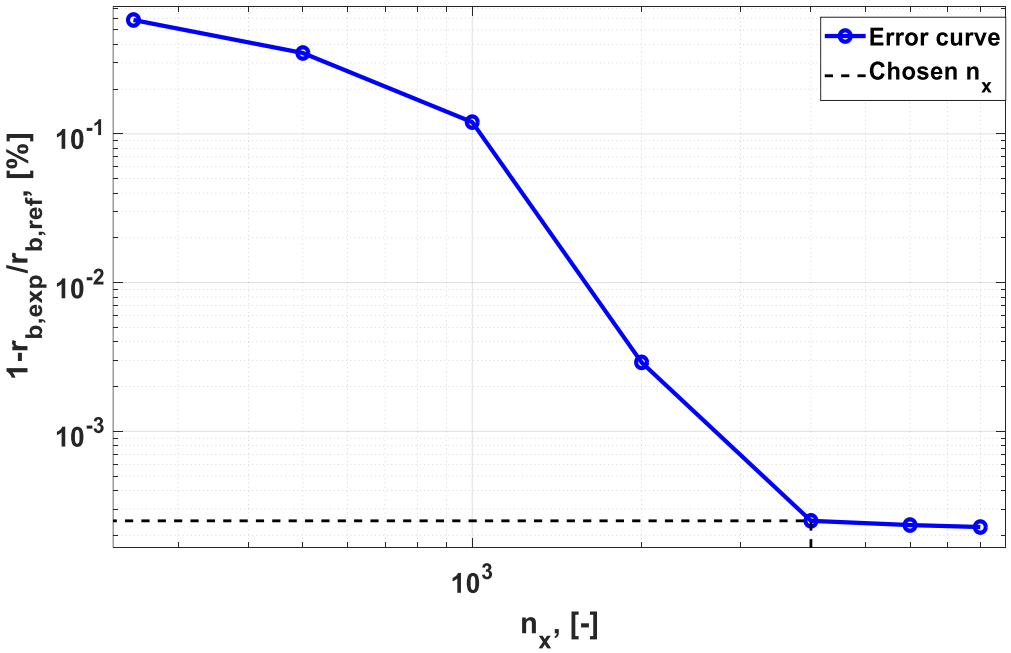

Figure 65: Grid dependance.

More in detail, the convergence profile is computed through seven simulations concerning the same burning rate variation but with different spatial grid level of refinement (n_x). The percentual relative error between simulated burning rate and experimental one, concerning how far $r_{b,ref}$ is from $r_{b,exp}$, has been examined. A grid refinement of $n_x = 4000$, linked to an error of $3 \cdot 10^{-4}\%$ has been considered adequate.
All simulations previously discussed have been carried out with ROBOOST software installed on a computer with the following features: 16 Gb RAM, Intel Core i7-7th generation CPU machine with 3.10 GHz and NVIDIA Quadro M1200 graphic card. Each simulation lasted 1 hour.

4.4 Conclusions

A new simplified approach to explain and predict the combustion chamber pressure peak at the tail off, namely Friedman Curl effect, has been proposed [31]. The physical set of equations, due to its lack of mathematical complexity, has led to the coupling between ROBOOST internal ballistics

model and the Friedman Curl burning rate profile in space. All the developed code has been applied on small-scaled motors, namely Baria, where the Friedman Curl pressure peak is evident at different combustion chamber pressure levels. A quite satisfactory match between simulated pressure peaks and experimental ones has been obtained in all three Baria sets.

References

[1] Fry, R., S., "Solid Propellant Test Motor Scaling," Chemical Propulsion Information Agency (CPIA), CPTR73, Columbia, Maryland, July 2001.

[2] Fry, R., S., "Solid Propellant Subscale Burning Rate Analysis Methods for U.S. and Selected NATO Facilities," Chemical Propulsion Information Agency (CPIA), CPTR73, Columbia, Maryland, January 2002.

[3] Viganò, D., Annovazzi, A., and Maggi, F., "Monte Carlo Uncertainity Quantification Using Quasi-1D SRM Ballistic Model," *International Journal of Aersopace Engineering*, Vol. 2016, April 2016, pp. 1-8. https://doi.org/10.1155/2016/3765796

[4] Fry, R., S., De Luca, L., Frederick, R., Gadiot, G., Strecker, R., Whitehouse, A., Traineau, J. C., Besser, H., L., Ribereau, D., and Reynaud, J. P., "Evaluation of Methods for Solid Propellant Burning Rate Measurement," Advances in Rocket Performance Life and Disposal, September 2002.

[5] N. Lupoglazoff, N., Vuillot, F. and Fabignon, Y., "Numerical simulations of the Unsteady Flow Inside Segmented Solid-Propellant Motors with Burning Aluminum Particles," AIAA Paper 2002-784, January 2002. https://doi.org/10.2514/6.2002-784

[6] Pekkan, K. and Ucer,A., "One-Dimensional Combustion Instability Studies with Moving Boundariws in an End-Burning Test Motor," AIAA Paper 2002-3608, July 2002. https://doi.org/10.2514/6.2002-3608

[7] Esiyok, H. and Cndarli, M., E., "Design of Experiment Approach to the Burning Rate Anomaly of Composite Solid Propellant,", AIAA Paper 2018-4577, July 2018. https://doi.org/10.2514/6.2018-4577

[8] Le Breton, P., Ribereau, D., Godfrov, F., Abgrall, R. and Augoula, S., "SRM performance analysis by coupling bidimensional surface burn back and pressure field computations", AIAA Paper 1998-3968, July 1998. https://doi.org/10.2514/6.1998-3968

[9] Wang, G., Li, D., D., Han, W., Z. and Zhang, Y, "Simulation of Transient Internal Flow Field of Solid Rocket Motor Based on Level-set Method," Binggong Xuebao/Acta Armanetarii, vol. 38, n. 8, 2017, pp. 1520-1531. https://doi.org/10.3969/j.issn.1000-1093.2017.08.009

[10] Wang, G., Li, D., D., Han, W., Z. and Zhang , "Research on grain burning surface regression based on level-set method and minimum distance function," Binggong Xuebao/Acta Armamentarii, vol. 38, n. 2, 2017, pp. 280-291. https://doi.org/10.3969/j.issn.1000-1093.2017.02.011

[11] Bertacin, R., Ponti, F., Corti, E. and Annovazzi, A., "Numerical Simulation of the Zefiro 9 Performance Using a New Dynamic SRM Ballistic Simulator," AIAA Paper 2013-4174, July 2013 https://doi.org/10.2514/6.2013-4174

[12] Yamada, K., Goto and M., Ishikawa, N., “Simulative Study on the Erosive Burning of Solid Rocket Motors,” AIAA Journal, vol. 14, n. 9, September 1976, pp. 1170-1176. https://doi.org/10.2514/3.61451

[13] Hart, R., W., Bird, J., F., Cantrell, R., H. and McClures, F., “Nonlinear Effects in Instability of Solid-Propellant Rocket Motors,” AIAA Journal, vol. 2, n. 7, July 1964, pp. 1270-1273. https://doi.org/10.2514/3.55069

[14] . Sutton, G., P. and Biblarz, O., “Rocket Propulsion Elements”, Thrust and Thrust Coefficient, 7th ed., John Wiley & Sons Inc., New York, 2010, pp.62-64.

[15] Ponti, F., Mini, S., and Annovazzi, A., “Parametric Study on Solid Rocket Motor Ignition Transient Prediction using ROBOOST simulation tool”, AIDAA XXV International Conference, September 2019.

[16] Mini, S., Ponti, F., Annovazzi, A., “Impact of Thermal Protections Insulation Layer on Solid Rocket Motor Performance”, AIAA Paper 2020-3933, August 2020. https://doi.org/10.2514/6.2020-3933

[17] Harrland, A., and I. Johnston, I., “Review of Solid Propellant Ignition Models Relative to the Interior Ballistic Modelling of Gun Systems,” Defense Science and Technology Organization, DSTO-TR-2735, August 2012.

[18] Harrland, A., and I. Johnston, I., “Review of Solid Propellant Ignition Models Relative to the Interior Ballistic Modelling of Gun Systems,” Defence Science and Technology Organisation, DSTO-TR-2735, August 2012

[19] Peretz, A., Kuo, K., and Summerfield, M., “The starting transient of solid-propellant rocket motors with high internal gas velocities,” AIAA Paper 1972-1119, November 1972. https://doi.org/10.2514/6.1972-1119

[20] Smith, G., D., “Numerical Solution of Partial Differential Equations: Finite Difference Methods”, Parabolic Equations: alternative derivation of difference equations and miscellaneous topics, 3rd ed., Clarendon Press, Oxford Clarendon Press, 1986, pp. 111-158

[21] Douglass, H., W., Collins, J., H., Miller, W., H. and Keller, R., B., “Solid Rocket Motor Performance Analysis and Prediction,” NASA SP-8039, May 1971.

[22] Dey, A., Kumar, A., Sikder, A. and Gupta, M., “Chemically Collapsible Mandrel for Solid Rocket Motor Processing,” Journal of Aerospace Technology and Management, vol. 7, n. 3, 2015, pp. 277-284. https://doi.org/10.5028/jatm.v7i3.494

[23] Le Breton, P. and Ribéreau, D., “Casting Process Impact on Small-Scale Solid Rocket Motor Ballistic Performance,” Journal of Propulsion and Power, vol. 18, n. 6, 2002, pp. 1211-1217. https://doi.org/10.2514/2.6055

[24] Shimada, T., Kitagawa, K., Hasegawa, H., and Asakawa,H., “Development of Advanced Computer Science for Solid Rocket Motor Internal Ballistics: ACSSIB,”, International Astronautical Conference, IAC-10.C4.2.6, October 2010.

[25] Paravan, C., Verga, A., Maggi, F., Galfetti, L., “Accelerated ageing of micron- and nano-sized aluminum powders: Metal content, composition and non-isothermal oxidation reactivity,” Acta Astronautica, vol. 158, May 2019, pp. 397-406. https://doi.org/10.1016/j.actaastro.2018.08.001

[26] Bolmshield, F. S. and Osborn, J., R., “Effect of variable solid phase thermal properties on propellant combustion,” Acta Astronautica, vol. 12, n. 12, 1985, pp. 1017-1025. https://doi.org/10.1016/0094-5765(85)90030-X

[27] Vladimir, A. and De Izarra, C., “Measurements of Thermal Conductivity of Aluminum Nanopowders by Photoacoustic Spectroscopy,”, ENS’07, Paper HAL-00202511, December 2007.

[28] Kingery, W., D., “Thermal Conductivity: XIV, Conductivity of Multicomponent Systems,” Journal of the American Ceramic Society, vol. 42, n. 12, 1959, pp. 617-627. https://doi.org/10.1111/j.1151-2916.1959.tb13583.x

[29] Angle, J., P., Wang, Z., Dames, C., and Mecartney, M., L., “Comparison of Two-Phase Thermal Conductivitu Models with Experiments on Dilute Ceramic Composites,” Journal of the American Ceramic Society, vol. 96, n. 9, 2013, pp. 2935-2942. https://doi.org/10.1111/jace.12488

[30] Cai, W., Thakre, P., and Yang, V., “A Model of AP/HTPB Composite Propellant Combustion in Rocket-Motor Enviroments,” Combustion Science and Technology, vol. 18, n. 12, 2008, pp. 2143-2169. https://doi.org/10.1080/00102200802414915

[31] Ponti, F., Mini, S., and Annovazzi, A., “A Simplified Approach to Predict Friedman Curl Effect in a Solid Rocket Motor using ROBOOST Simulation Tool,” AIAA Paper 2019-3959, August 2019. https://doi.org/10.2514/6.2019-3959

Chapter 5

5 Impact of case-insulating thermal protection layer

Nomenclature

Latin

A_{TP} = thermal protections area, m^2
B = Arrhenius constant, $1/s$
c_P = specific heat, $J/kg \cdot K$
E_a = Arrhenius activation energy per unit mole, J/mol
$F_{noz \to TP_i}$ = view factor between nozzle and rocket case section i, $[-]$
h = enthalpy per unit mass, J/kg
$\bar{h}$ = weighted average enthalpy per unit mass, J/kg
h_c = heat transfer convective coefficient, $W/m^2 \cdot K$
k = thermal conductivity, $W/m \cdot K$
L = thermal protections thickness, m
M = mass flow rate per unit surface, $kg/s \cdot m^2$
$\dot{Q}_{abs}$ = thermal power absorbed by ablative material from combustion chamber, W
$\dot{Q}_{cond}$ = thermal conduction power per unit surface, W/m^2
$\dot{Q}_{conv}$ = thermal convective power per unit surface, W/m^2
$\dot{Q}_{in}$ = chemical power per unit surface from in-depth material, W/m^2
$\dot{Q}_{out}$ = nozzle radiative power per unit surface, W/m^2
$\dot{Q}_{out}$ = chemical power per unit surface exiting from the material due to blowing effect, W/m^2
$\dot{Q}_{rad_{in}}$ = radiative power per unit surface entering the material, W/m^2
$\dot{Q}_{rad_{out}}$ = radiative power per unit surface exiting the material, W/m^2
R = universal gas constant, $J/mol \cdot K$
r_b = propellant burning rate, m/s
$\dot{s}$ = char recession rate, m/s
t = time, s
t_0 = reference time instant, s
T = temperature, K
T_I = initial thermal protection temperature, K
T_0 = formation temperature, K
x = spatial coordinate, m

Greek

α = weighted average between virgin material and char specific heats, $J/kg \cdot K$
α_s = ablative material absorptivity, -
β = weighted average virgin material and char specific heats difference, $J/kg \cdot K$

ε = emissivity, -
η = weighted average between virgin material and char thermal conductivities, $W/m \cdot K$
ξ = weighted average virgin material and char conductivities, $W/m \cdot K$
ρ = density, kg/m^3
σ = Stefan-Boltzmann constant, $W/m^2 \cdot K^4$
φ = blowing parameter, -
X = virgin material mass fraction, -
ψ = Arrhenius exponent, -

Subscripts
c = char material
g = pyrolysis gas
gas = combustion chamber hot gases
noz = nozzle region surrounded by the combustion chamber
p = propellant
v = virgin material

Superscript
$'$ = integration variable
o = formation enthalpy

Acronyms
CMA = Charring Material thermal response and Ablation program
$FIAT$ = Fully Implicit Ablation and Thermal analysis program
$PATO$ = Porous material Analysis Toolbox
PDE = Partial Differential Equation
$ROBOOST$ = Rocket BOOst Simulation Tool
SRM = Solid Rocket Motor
$Z9$ = ZEFIRO (Zero First stage ROcket motor) 9
$Z23$ = ZEFIRO (Zero First stage ROcket motor) 23

5.1 Introduction

The scope of the present chapter is the estimation of the influence of case-insulating thermal protection material on SRMs tail-off thrust, where the thermal protection ablation phenomenon is assumed to be mainly caused by the radiative power produced by the nozzle surface. The aforementioned predictions assume a fundamental signification for upper stages SRMs, since the pyrolysis gases mass flow rate, produced by thermal protection material, expanding into a low-pressure environment, generates a not-negligible amount of thrust (residual thrust) able to still accelerate the system at the tail-off phase. Due to its duration period (in the order of tens of seconds after the SRM burn-out time), the residual thrust evaluation is meant to have a design key role in the proper sequencing of stage separation and in managing both interstage wait times and separation systems total impulse. Some past literature works [1-3] have asserted that the pyrolysis gases production because of thermal protection material ablation is sustained by the alumina deposited within the motor case during the grain combustion in the following manner: the amount of alumina, namely molten slug, acts as a radiative power source toward the thermal protection layer even after the complete grain depletion, maintaining the thermal protection material ablation.

The present study is aimed to emphasize the occurrence of another radiative heat source allowing case-insulating thermal protections ablation, and therefore residual thrust production: indeed, while grain is burning, the inner portion of the nozzle (Figure 66d, Figure 67d) within the combustion chamber absorbs the convective and radiative energy released by hot gases generated through grain combustion. Subsequently, when almost all grain is burned, and the thermal protection layer is no longer inhibited, the nozzle behaves as a source of radiative heat permitting the ablation of thermal protection material, in the same manner of the alumina slag discussed in the previous paragraph.

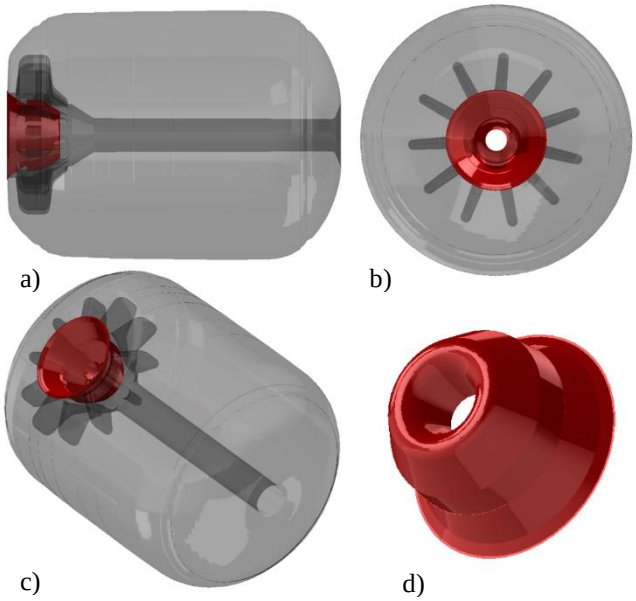

Figure 66: ZEFIRO 9 thrust chamber.

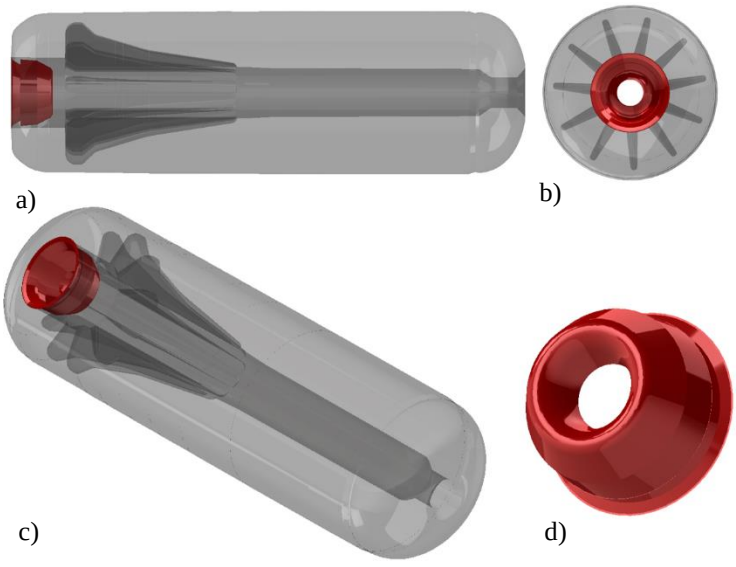

Figure 67: ZEFIRO 23 thrust chamber.

The impact of the case-insulating thermal protection material on residual thrust occurring at the tail-off phase, together with the nozzle radiative power, consists of two phases. First, a mathematical-physical model able to reproduce thermal protection ablation/pyrolysis is settled through specific

assumptions. The main outcome of the previously mentioned model is expressed by the generation of maps where the output quantities are pyrolysis gases mass flow rate and combustion chamber heat power absorbed by thermal protection material through its endothermic reaction of ablation. Those maps are exploited by an internal ballistics simulation software to estimate thrust-time profile of two actual SRMs stages, namely ZEFIRO 9 and ZEFIRO 23, belonging to VEGA launcher. The designated software is ROBOOST (Rocket BOOst Simulation Tool), a MATLAB® based software capable to simulate burning surface regression, combustion chamber fluid dynamics, grain anisotropies/defects [5] and other phenomena arising at thrust tail-off phase [6]. The reason of that choice is that ROBOOST, because of the 3D burning surface regression, is able to compute at each simulation time step the portion of the thermal protection material exposed to combustion chamber hot gases. The assessment of thermal protection exposure is a crucial parameter to estimate first the amount of pyrolysis gases and finally the SRM residual thrust production.

5.2 Literature review

Polymeric composites have been used as ablative thermal protection systems for a variety of military and aerospace applications. Their most important feature relies on ablation which is generally linked to all the physicochemical processes (sublimation, chemical reactions, and erosion) arising at the material interface where solid depletion takes place [7].More specifically, in solid rocket motors, they are aimed to restrain thermal loads coming from thrust chamber hot gases by absorbing most part of thermal power and maintaining the underlying structure (for instance the metallic case or the nozzle throat section) within acceptable temperature limits [8]. To sum up, they behave as a heat sink barrier against a high-temperature environment [9]. Thermal protection composite materials are usually partitioned in two major types [10]: *charring* ablators and *non-charring* ablators. The main difference is that the *charring* material ablation leads to the formation of gaseous products (pyrolysis gases, mainly hydrocarbons-based) and a solid product, namely char, consisting of structured chains of carbonaceous compounds. The aforementioned material decomposition relies on charring material structure: they are marked out by fibrous materials immersed in a resin whose effect is to increase the mechanical strength [11-12]. More in detail, resin decomposition contributes to pyrolysis gas formation, whereas solid fibers are responsible for char formation.

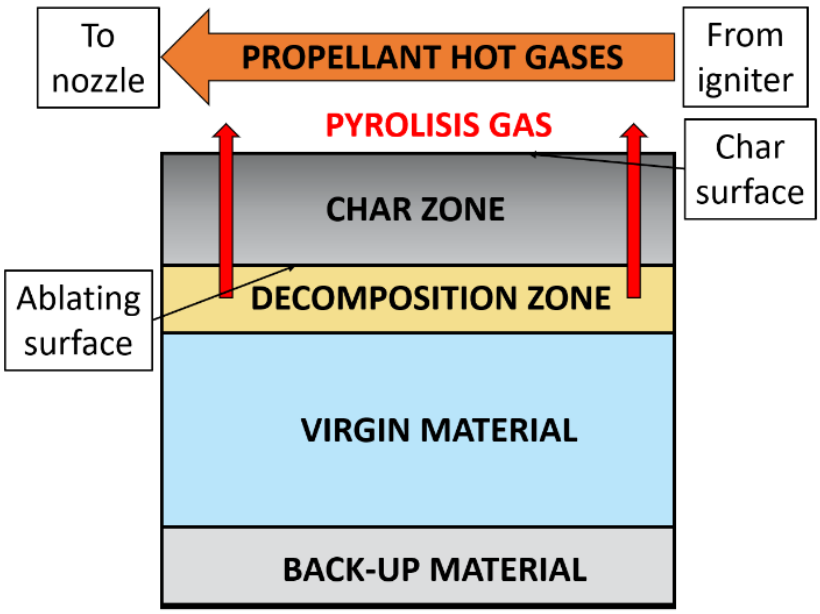

Figure 68: Thermal protection charring material.

Figure 68 displays how *charring* materials behave when are subject to the combustion chamber hot gases heat within a solid rocket motor. Different layers occur, from the char zone close to the combustion chamber to the virgin material near the metallic case. All along grain combustion process, char layer thickness is reduced by two factors: chemical erosion caused by the reactions between interface material and hot gases boundary layer species, and mechanical erosion induced by the flow friction with respect to the char surface (Figure 68). On the contrary, no pyrolysis gases production rises in *non-charring* materials ablation: chemical reactions are completely limited to the material surface [12]. Moreover, the ablative material surface layer (Figure 68) could face melting at certain temperatures: from this perspective, there are *melting* or *subliming* ablators and *non-melting* ablators [14]. For instance, *charring* materials belong to the latter category, since when a certain amount of heat is absorbed by the material itself, they act as a heat sink up to sublimation by producing pyrolysis gases. On the other hand, *non-melting* ablators remove the incoming heat on their surface by melting instead of subliming.

As mentioned before, the aim of the present work is the evaluation of the impact of case-insulating thermal protection layer on SRMs performances. To reach that target, a mathematical-physical model regarding thermal protection material ablation must be established, together with a reliable internal ballistics simulator. The numerical treatment of the tight coupling between the SRM combustion chamber fluid dynamics and the generation of pyrolysis gases plays an important role in the modelling of general heat conditions acting to the interface between the case insulation material and the combustion hot gases. The main relevant program firstly assembled to achieve the previous objective is CMA (Charring Material thermal response and Ablation program) [15]. Its leading technique is a numerical finite difference-based method to solve a set of three equations. Two of them are the mass and energy balance; the third is the Arrhenius relation. It is used to model the density degradation process bringing the virgin unaltered material to char residual. Pyrolysis gases generation are also considered. The mathematical model is 1D unsteady and is applied on an isotropic material, ablating from the front surface. Equations are solved explicitly in time influencing the computation of char recession rate and inducing a quite significative dependance on the choice of simulation time step [16]. This disadvantage has been figured out in FIAT (Fully Implicit Ablation and Thermal Analysis program) software [17-18]. The numerical approach considered is the same adopted in the CMA: finite difference method where the equations derivatives are expressed in a moving grid system. The key difference between the two codes resides in the fully implicit solution of the mathematical model. The finite difference technique is not the only numerical strategy used to determine the problem solution: indeed, the authors of [11-12] have pointed out the possibility of using finite element method provided with first and second time implicit integrators to solve thermal equilibrium for porous reactive materials subjected to high temperatures. In recent past, both finite element and finite volume discretization have been merged to efficiently deal with the tight coupling between hypersonic aerodynamic heating and the material consumption of re-entry vehicle shields. This goal has been achieved by PATO (Porous Material Analysis Toolbox) [19-21] where a three-dimensional fluid-structural method is established with the purpose of give detailed predictions of re-entry vehicles material depletion. Ultimately, among thermal protections simulation codes panorama, there are commercial programs [22-23] where the material decomposition into gas phase/solid residual is not considered. In general, they are based on finite element approach.

The present study deals with case-insulating thermal protection layer of SRMs with an axisymmetric quasi-cylindrical shape (Figure 66, Figure 67). Therefore, 2D or 3D ablation models do not provide any not-negligible advantage in SRM performance evaluation concerning the impact of case material ablation; this is primarily due to the elementary SRM case geometry. Differently, multi-dimensional models are fundamental for more complex geometries like the ones representing heat shields of re-entry vehicles. In the above-mentioned cases 2D or 3D contributions are no longer negligible.

According to the previous explanation, a 1D unsteady model has been considered to describe the ablation phenomenon in this work. Equations are discretized by means of finite difference numerical technique: indeed, it is more effective on simple geometries than other methods, like finite volume or finite elements [25]. A particular disadvantage of the finite difference method is the number of spatial nodes considered in the domain discretization especially for complex geometries, therefore implying a considerable increase of computational efforts.

5.3 Mathematical-physical model

The mathematical-physical model regarding the case-insulating thermal protection material is based on the following assumptions [26]:

- Thermal protection and pyrolysis gases are modeled as a *continuum*, allowing the description of physical quantities by means of continuous functions.
- Heat propagation across the material is considered a 1D unsteady phenomenon. The direction of propagation is perpendicular to the material surface (gray surface in Figure 69).
- Pyrolysis gases produced by material ablation are in thermal equilibrium with the char layer.
- No chemical reaction between pyrolysis gases, grain combustion hot gases and char residual occur at the material surface exposed to combustion chamber environment.
- The mixture represented by pyrolysis gases is always in chemical equilibrium.
- Pyrolysis gases are modeled as a Newtonian fluid.
- After the formation of pyrolysis gases, all gaseous chemical compounds are assumed to immediately exit the char layer. This implies a zero-residence time of pyrolysis gases within the char itself.
- Char porosities are neglected.
- Momentum transport of pyrolysis gases is neglected.
- Degradation bringing the original material from virgin to char is driven by Arrhenius-type-of-expression regarding the material density decrease in time and space. Although it is theoretically possible to model the material degradation considering other methods (like considering density simply as a function of temperature or identifying a fixed activation temperature marking the transition from virgin to char material), Arrhenius relation guarantees an accurate representation of the physical phenomenon without leading to a challenging numerical problem and preserving an acceptable computational time [26].

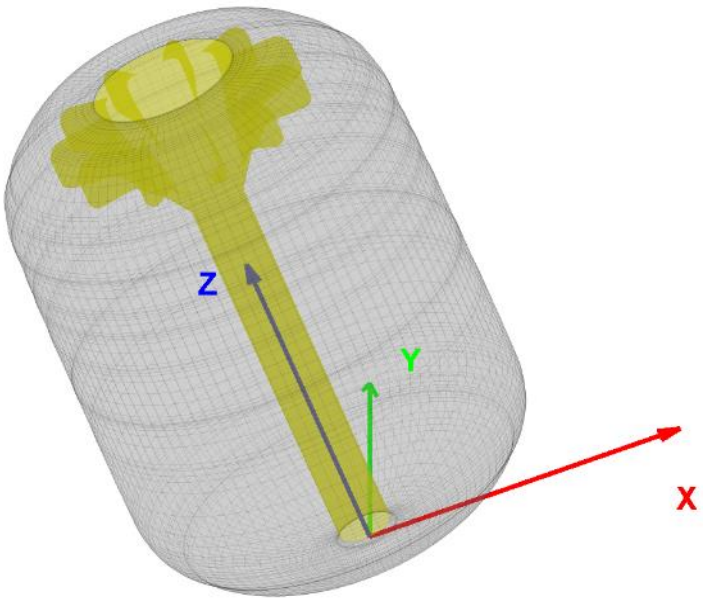

Figure 69: Ablation model global reference frame.

Equations are expressed in a moving reference frame, tied to the material receding surface, namely the char surface (Figure 70) separating the combustion chamber domain with respect to the thermal protection material domain. Each quantity varies along x direction and in time t.

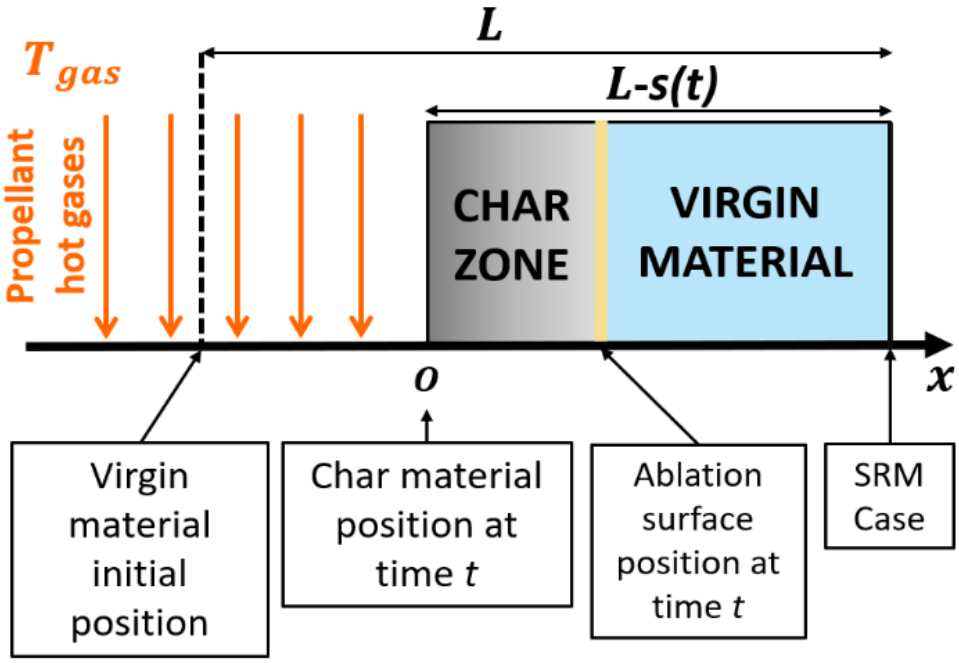

Figure 70: Thermal protection material local reference frame.

The mathematical system consists of three equations (Eq. (1) to Eq. (3)):

$$\frac{\partial \rho}{\partial t} = \dot{s}\frac{\partial \rho}{\partial x} + \frac{\partial M_g}{\partial x} \tag{1}$$

$$\frac{\partial \rho}{\partial t} = \dot{s}\frac{\partial \rho}{\partial x} - B\rho_v e^{-\frac{E_a}{RT}}\left(\frac{\rho - \rho_c}{\rho_v}\right)^{\psi} \tag{2}$$

$$\frac{\partial T}{\partial t} = \frac{1}{\alpha\rho - \beta}\Bigg\{\left(h_g - \bar{h}\right)\frac{\partial M_g}{\partial x} + \left[\dot{s}(\alpha\rho - \beta) + M_g c_{p_g} + \frac{\xi}{\rho^2}\frac{\partial \rho}{\partial x}\right. + \left(\frac{\rho_v}{\rho_v - \rho_c}\left(1 - \frac{\rho_c}{\rho}\right)\left(\frac{\partial k_v}{\partial T} - \frac{\partial k_c}{\partial T}\right) + \frac{\partial k_c}{\partial T}\right)\frac{\partial T}{\partial x}\Bigg]\frac{\partial T}{\partial x} + \left(\eta - \frac{\xi}{\rho}\right)\frac{\partial^2 T}{\partial x^2}\Bigg\} \tag{3}$$

More in detail, Eq. (1) expresses the mass balance, Eq. (3) the energy balance and Eq. (2) Arrhenius expression linked to the material degradation. They marked out the in-depth solution, namely the parameters variation within the material but without the two boundaries (Figure 70). The mathematical solution is expressed by the following functions depending on x and t: material density ρ, pyrolysis gases mass flow rate per unit surface M_g and material temperature T. Besides that, the coefficients α, β, ξ, η, $\bar{h}$, h_g, h_v, h_c, appearing in Eq. (1) to Eq. (3), are:

$$\alpha = \frac{c_{p_v}\rho_v - c_{p_c}\rho_c}{\rho_v - \rho_c} \tag{4}$$

$$\beta = \left(c_{p_v} - c_{p_c}\right)\frac{\rho_v\rho_c}{\rho_v - \rho_c} \tag{5}$$

$$\xi = (k_v - k_c)\frac{\rho_v\rho_c}{\rho_v - \rho_c} \tag{6}$$

$$\eta = \frac{k_v\rho_v - k_c\rho_c}{\rho_v - \rho_c} \tag{7}$$

$$\bar{h} = \frac{\rho_v h_v - \rho_c h_c}{\rho_v - \rho_c} \tag{8}$$

$$h_g = h_g^0 + \int_{T_0}^{T} c_{p_g}(T')dT' \tag{9}$$

$$h_v = h_v^0 + \int_{T_0}^{T} c_{p_v}(T')dT' \tag{10}$$

$$h_c = h_c^0 + \int_{T_0}^{T} c_{p_c}(T')dT' \tag{11}$$

Eq. (4) to Eq. (11) are linked with temperature dependent properties regarding the thermal protection material. Specifically, the thermal conductivity temperature dependence is also evident in Eq. (3) with respect to the terms $\frac{\partial k_v}{\partial T}$ and $\frac{\partial k_c}{\partial T}$. In fact, material properties can locally be conditioned by the heat amount at a specific spatial point. In addition to that, in order to numerically solve the above-mentioned set of PDEs (Partial Differential Equations) initial conditions and boundary conditions are needed. Initial conditions are outlined through Eq. (12) to Eq. (14):

$$\rho(t = 0, x) = \rho_v \tag{12}$$

$$M_g(t = 0, x) = 0 \tag{13}$$

$$T(t = 0, x) = T_I \tag{14}$$

Eq. (1) states that at initial time no ablation occurs: indeed, all the thermal protection material is considered virgin material with density ρ_v. The temperature (Eq. (14)) is at ambient condition (T_I), hence no pyrolysis gas generation occurs (Eq. (13)).
Combustion chamber interface and wall boundary conditions are (Eq. (15) to Eq. (16)):

$$M_g(t, x = L - s) = 0 \tag{15}$$

$$\dot{Q}_{conv} + \dot{Q}_{rad_{in}} - \dot{Q}_{rad_{out}} - \dot{Q}_{out} + \dot{Q}_{in} - \dot{Q}_{cond} = 0 \tag{16}$$

where:

$$s = \int_{o}^{t} \dot{s}(t')dt' \tag{17}$$

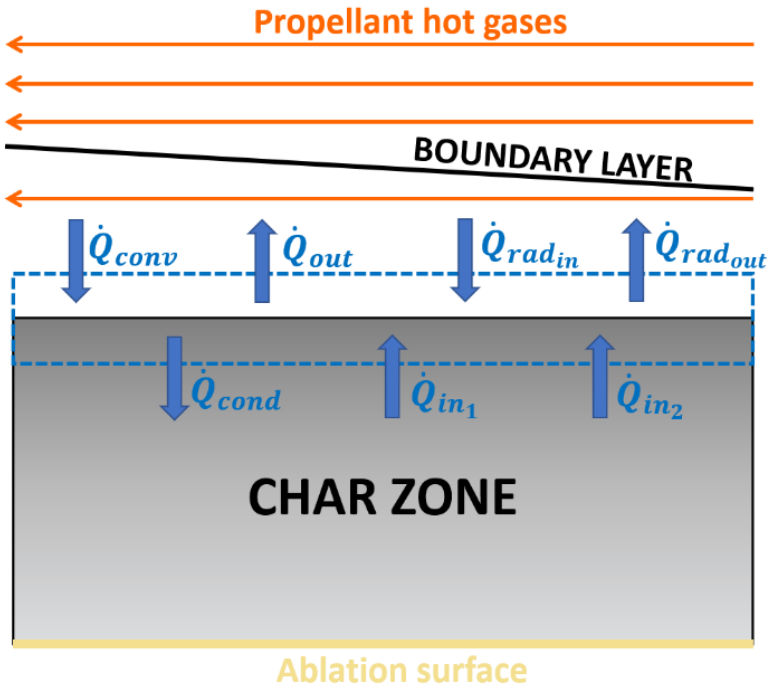

Figure 71: Energy balance at the char recession surface.

First, Eq. (15) is established at the SRM case (Figure 70). No mass transfer takes place at this point. Hence pyrolysis gases mass flow rate per unit surface is zero when the end of the domain ($x = L - s$) is considered for a generic simulation time. It is of fundamental importance to highlight that the chosen reference frame is moving with the char recession surface: the distance displaced by the interface is s, where $\dot{s}$ is the time-dependent char recession rate. Second, Eq. (16) describes the heat balance [26] at the char surface (Figure 71). The multiple contributions are (Eq. (18) to Eq. (26)):

$$\dot{Q}_{conv} = h_c \frac{\varphi}{e^{\varphi} - 1}(T_{gas} - T(t, x = 0)) \tag{18}$$

$$\dot{Q}_{rad_{in}} = \alpha_s \sigma \varepsilon_{gas} T_{gas}^4 + \dot{Q}_{abs(noz)} \tag{19}$$

$$\dot{Q}_{rad_{out}} = \sigma \varepsilon_{TP} T^4(t, x = 0) \tag{20}$$

$$\dot{Q}_{out} = (M_c c_{p_c} + M_g(t, x = 0) c_{p_g}) T(t, x = 0) \tag{21}$$

$$\dot{Q}_{in} = \dot{Q}_{in_1} + \dot{Q}_{in_2} = M_c h_c + M_g(t, x = 0) h_g \tag{22}$$

$$\dot{Q}_{cond} = -k(t, x = 0) \left.\frac{\partial T}{\partial x}\right|_{t,x=0} \tag{23}$$

where:

$$\varphi = \frac{2\lambda(M_c + M_g(t, x = 0)) c_{p_{gas}}}{h_c} \tag{24}$$

$$k(t, x) = \mathrm{X}(t, x) k_v + (1 - \mathrm{X}(t, x)) k_c \tag{25}$$

$$\mathrm{X}(t, x) = \frac{\rho_v}{\rho_v - \rho_c} \left(1 - \frac{\rho_c}{\rho}\right) \tag{26}$$

The convective power transferred between propellant combustion hot gases within the boundary layer and the char surface is modelled through Eq. (18). The term $^{\varphi}/_{e^{\varphi} - 1}$ refers to the blowing effect linked to the boundary layer (Figure 72). Since boundary layer streamlines are deflected (orange lines in Figure 72), blowing phenomenon implies a decrease of the heat transfer convective coefficient.

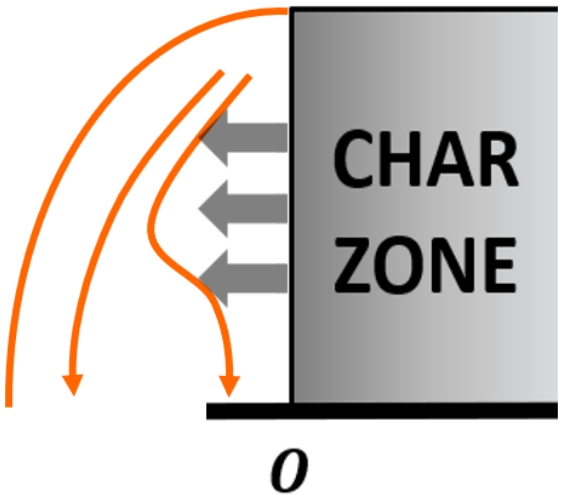

Figure 72: Boundary layer blowing effect.

This decrease can be integrated with the dependance on boundary layer flow regime through the coefficient λ (Eq. (24)). More in detail, λ is obtained by fitting experimental data and it is also aimed

to include microscopic effects such as molecular weight influence. A value of λ=0.4 is chosen to correlate constant-properties turbulent flow data [27]. Equation (19) and Equation (20) respectively concern inward-directed and outward-directed radiative heat transfer. Equation (19) leads to two contributions. First, the radiative power produced by hot gases is included ($\alpha_s \sigma \varepsilon_{gas} T_{gas}^4$). The coefficient α_s is linked to the ablative material absorptivity in a two-phase gas mixture where one phase is gaseous, and the other consists of monodispersed alumina particles [29].
Second, the term $\dot{Q}_{abs(noz)}$ refers to the thermal protection absorbed power coming from the inner region of the nozzle within the combustion chamber (Figure 66). Each case of the two solid rocket motors analyzed in this work is split into N sections perpendicular to the motor axis z (Figure 73).

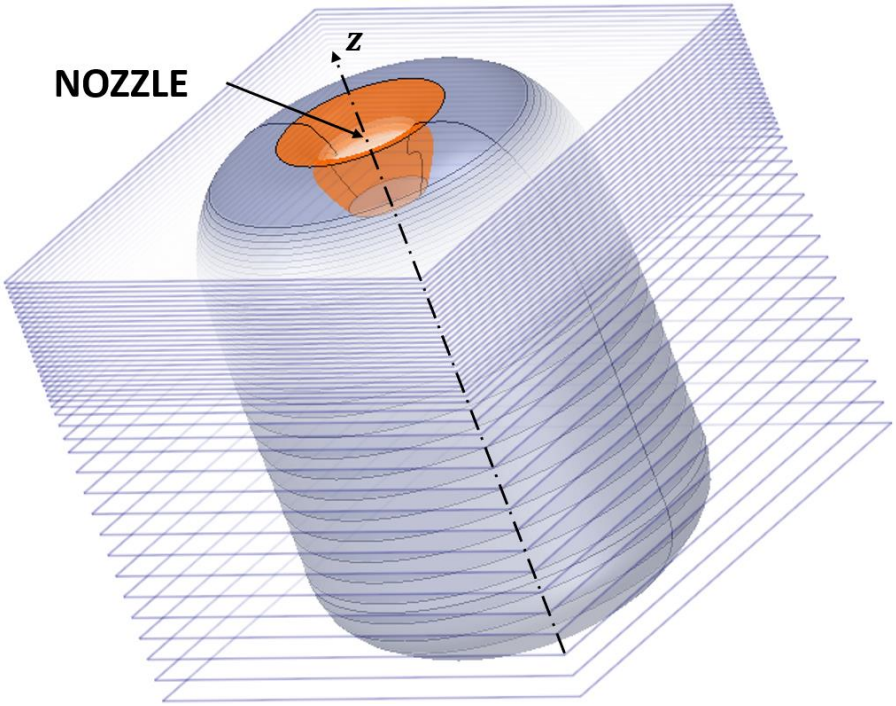

Figure 73: Z9 case partition.

A finer discretization has been considered in proximity of the finocyl-shaped combustion chamber in order to better reproduce the effect of the star in the view factor computation. For each case section i, both the thermal protection surface A_{TP_i} and the view factor $F_{noz \to TP_i}$ are obtained (Figure 74, where view factors are normalized with respect to the maximum view factor of Z23).

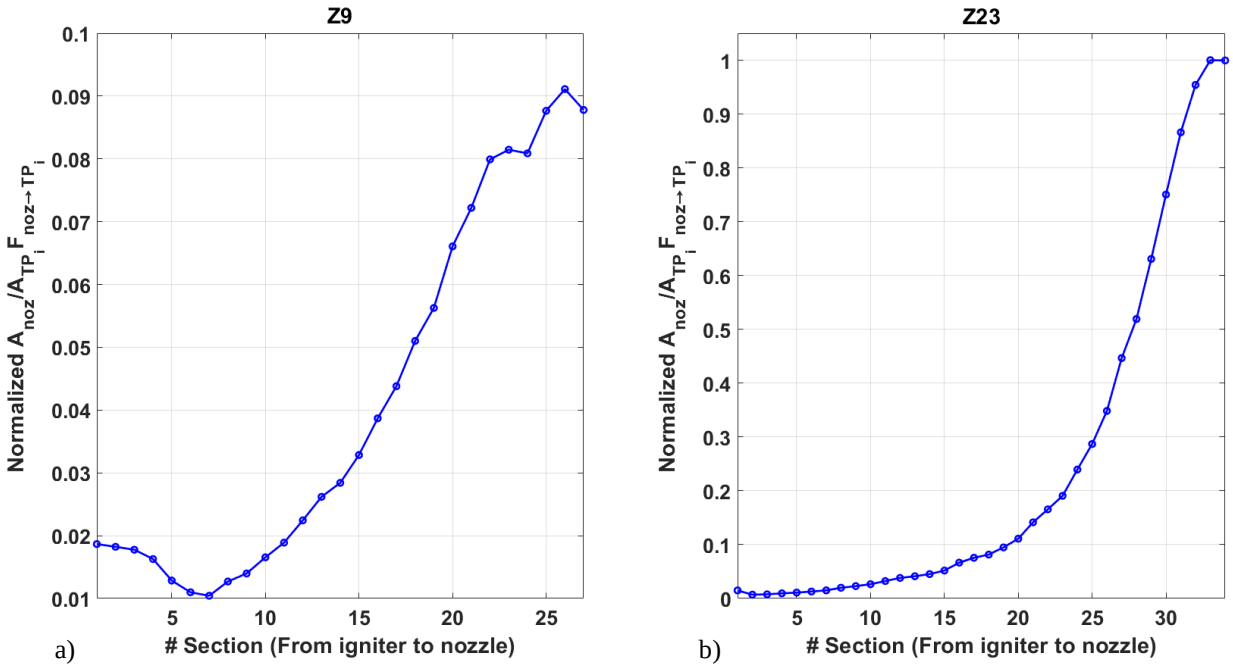

Figure 74: View Factor distribution.

Then, $\dot{Q}_{abs(noz)}$ is obtained though the following formulas (Eq. (27) and Eq. (28)), [28]:

$$\dot{Q}_{abs(noz)_i} = \frac{A_{noz}}{A_{TP_i}} F_{noz\rightarrow TP_i} \sigma \left(T_{noz}^4 - T_{TP_i}^4\right) \tag{27}$$

$$\dot{Q}_{abs(noz)} = \sum_{i=1}^{N} \dot{Q}_{abs,noz_i} \tag{28}$$

From a deeper perspective, because of view factor reciprocity principle, the quantity $\frac{A_{noz}}{A_{TP_i}} F_{noz\rightarrow TP_i}$ is equivalent to $F_{TP_i\rightarrow noz}$, namely the view factor representing the heat amount radiated by the thermal protection and absorbed by the nozzle. It is essential to highlight that for each SRM analyzed, the thermal protection case and the nozzle do not establish an enclosure: indeed, from one side part of the irradiated power is dispersed in the external environment through the nozzle exhaust. On the other, due to the nozzle concave shape, a portion of radiation is absorbed by the nozzle itself. Thus, the view factor summation $\sum_{i=1}^{N} \frac{A_{noz}}{A_{TP_i}} F_{noz\rightarrow TP_i}$ is lower than 1.

The algebraic sum $\dot{Q}_{in} - \dot{Q}_{out}$ represents the net of several fluxes of chemical energies at the surface. More in detail, $\dot{Q}_{in}$ (Eq. (22)) regards the heat flux incident to the char surface from the inner region of the thermal protection material. In addition to that, $\dot{Q}_{out}$ (Eq. (21)) is associated to the power leaving the char surface in the gross motion (blowing) of the gas adjacent to the surface (Figure 71). Finally, the power crossing the solid material is modelled by means of Eq. (23). The thermal conductivity k is expressed by the weighted average (Eq. (25)) between virgin material thermal conductivity, k_v , and char residual thermal conductivity k_c. The average weight considered is X (Eq.

(26)) which represents the mass fraction of the virgin material with respect to the overall material consisting of char residual and virgin material itself. The char recession rate $\dot{s}$ appearing in Eq. (17) is computed from the time integration of the mass conservation equation (Eq. (1)) at the gas-solid interface surface of the pyrolyzing material [30]. Starting from char recession rate definition (Eq. (29)), the integrated mass conservation equation in a moving reference frame is (Eq. (30)).

$$\dot{s} = \frac{M_c}{\rho_c} \tag{29}$$

$$M_c + M_g(t, x = 0) = \rho_v \dot{s} \tag{30}$$

Considering the steady state solution of Eq. (30), then the thickness of the char layer is time independent. By substituting M_c (computed from Eq. (30)) in Eq. (29), the $\dot{s}$ final expression is found (Eq. (31).

$$\dot{s} = \frac{M_g(t, x = 0)}{\rho_v - \rho_c} \tag{31}$$

Equation (31) states a direct proportionality between the char recession rate and the pyrolysis gases mass flow rate per unit surface exiting the material when ablation takes place.
Numerical solutions (ρ, M_g, T) of the in-depth response (Eq. (1) to Eq. (3)) are computed using a finite difference approach. Since for most common materials the density profile with respect to time and space has a steep spatial gradient because of the material degradation from virgin to char occurring at a small spatial thickness, a 4th -order difference formula is needed for the space partial derivatives approximation. However, different stencils are used. Regarding E. (1) and Eq. (2) a 4th order forward difference formula (Figure 75b) has been considered since the information is carried from the left side $(x = 0)$ to the right one $(x = L - s)$ with the velocity $\dot{s}$. On the contrary, in Eq. (3) the heat diffusion is the dominant mechanism in all directions: a 4th order central stencil (Figure 75a) has been selected.

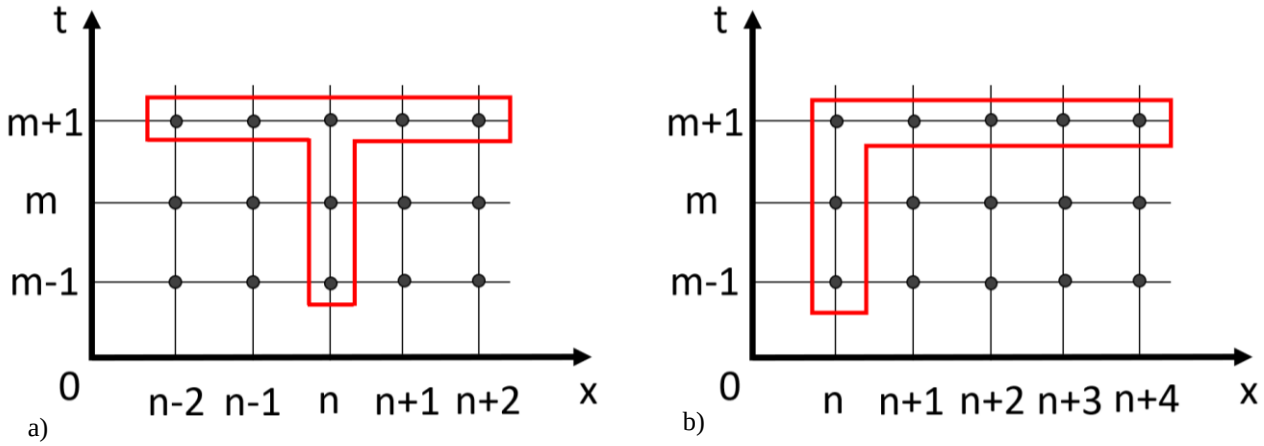

Figure 75: Finite difference stencil.

Boundary condition spatial discretization is the following one: Eq. (15) is discretized with a 4th-order backward scheme, Eq. (16) relies on a numerical computation through a 4th-order forward spatial scheme. Differently, time discretization requires a deeper attention. In fact, the equations (Eq. (1) to Eq. (3)) are strictly coupled and highly nonlinear. To avoid numerical instability given by the stiffness of the problem, a backward difference formula of the 2nd order has been considered. Hence, the estimation of the function at future time instant t_{m+1} is based on the knowledge of the function values at previous time instants t_m and t_{m-1}

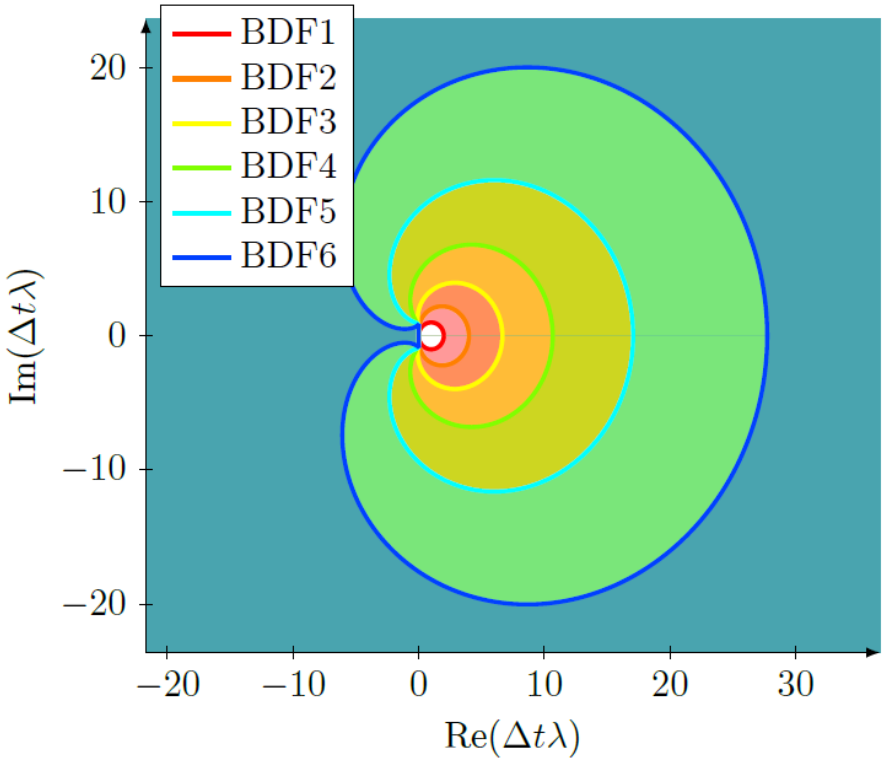

Figure 76: Absolute stability regions for backward difference formulas.

The stability region of the generic-order backward difference formula is depicted with turquoise color in Figure 76. It is evident that, the higher is the accuracy order of the backward difference formula, the higher is the extension of the unstable region (in Figure 76 it is the zone bounded by the colored lines, each one corresponding to a particular order backward difference formula). To maintain an acceptable degree of accuracy without affecting the numerical stability of the solution, the optimum numerical scheme proves to the 2nd order backward difference formula. The above-mentioned statement also validates the numerical approximating formula chosen in the present work.

5.3.1 Thermal protection maps generation

Starting from the solution of Eq. (1) to Eq. (31), thermal protection maps are computed by varying the following input parameters: combustion chamber hot gases temperature (T_{gas}), heat transfer convective coefficient (h_c) and radiative power per unit surface absorbed by case-insulating thermal protection material from the nozzle irradiation ($\dot{Q}_{abs(noz)}$). Each point of the map has four output quantities, namely the char recession rate ($\dot{s}$), the pyrolysis gases mass flow rate per unit surface exiting the solid material ($M_g(t, x = 0)$), the receding surface temperature ($T(t, x = 0)$) and the material absorbed power from the rocket combustion chamber only. For each map set (a map set

involves 4 maps each one linked to the same value of $\dot{Q}_{abs(noz)}$), many simulations are performed varying T_{gas} and h_c. It is important to point out that each map point is evaluated when the solution $\dot{s}$ reaches its steady-state value, after about 15s. In the previous sense, thermal protection maps can be treated as 0D maps.

5.3.2 Maps-ROBOOST coupling procedure

An in-house simulation software, namely ROBOOST (Rocket BOOst Simulation Tool) has been considered to perform internal ballistics simulations. It allows the prediction of the thrust-time profile of a generic-shaped solid rocket motor handling a 1D unsteady fluid dynamics model [31] together with a 3D burning surface regression in space.

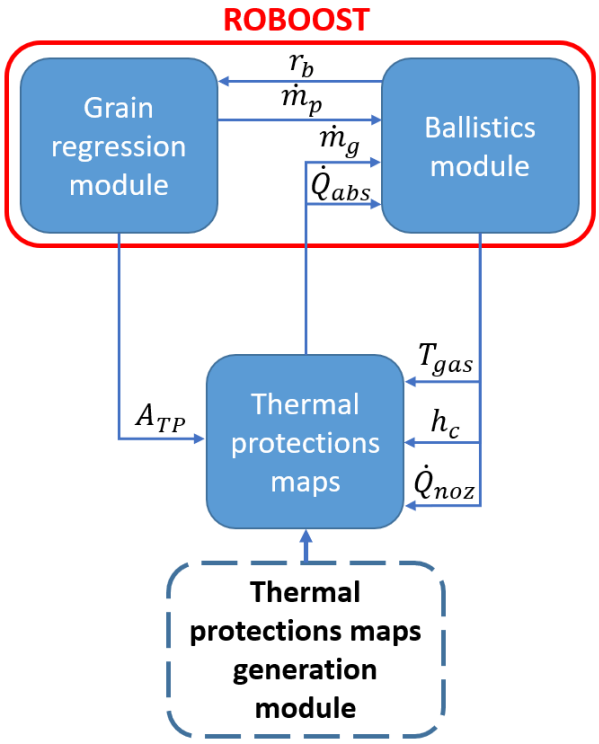

Figure 77: Integration procedure scheme.

The flow chart diagram in Figure 77 shows how ROBOOST simulator interacts with thermal protection maps. First, thermal protection maps are generated with the *Thermal protection maps generation module*. Map generation step is performed before internal ballistics simulation: indeed, map generation implies a larger amount of computational time than the internal ballistics simulations. Then, ROBOOST simulation is run to obtain tail-off thrust curve varying with time. At a certain time instant t the *Grain regression module* estimates both the amount of the burned propellant mass flow rate ($\dot{m}_p$) dumped in the combustion chamber and the thermal protection material surface (A_{TP}) directly exposed to the grain hot gases (Figure 78a). Subsequently, the *Ballistics module* computes the propellant burning rate (r_b) from the burned propellant mass flow rate and the quantities T_{gas}, h_c, $\dot{Q}_{abs(noz)}$ needed to figure out the values of pyrolysis gases mass flow rate ($\dot{m}_g$) and the absorbed power from the combustion chamber ($\dot{Q}_{abs}$) (Figure 78b). Again, the *Grain regression module* estimates $\dot{m}_p$ and A_{TP} with r_b previously obtained. If the new values of $\dot{m}_p$ and A_{TP} are respectively equal to the old ones less than a fixed tolerance, the algorithm convergence at time t is reached and it is possible to move forward to the next iteration at time $t + \Delta t$, where Δt is the simulation time

step. Figure 78c, d are respectively associated to the 2D and 3D visualization of the thermal protection material exposure time projected on Z9 case in terms of percentage burning time. The black lines bound the thermal protection material region exposed to combustion chamber gases at time instant t.

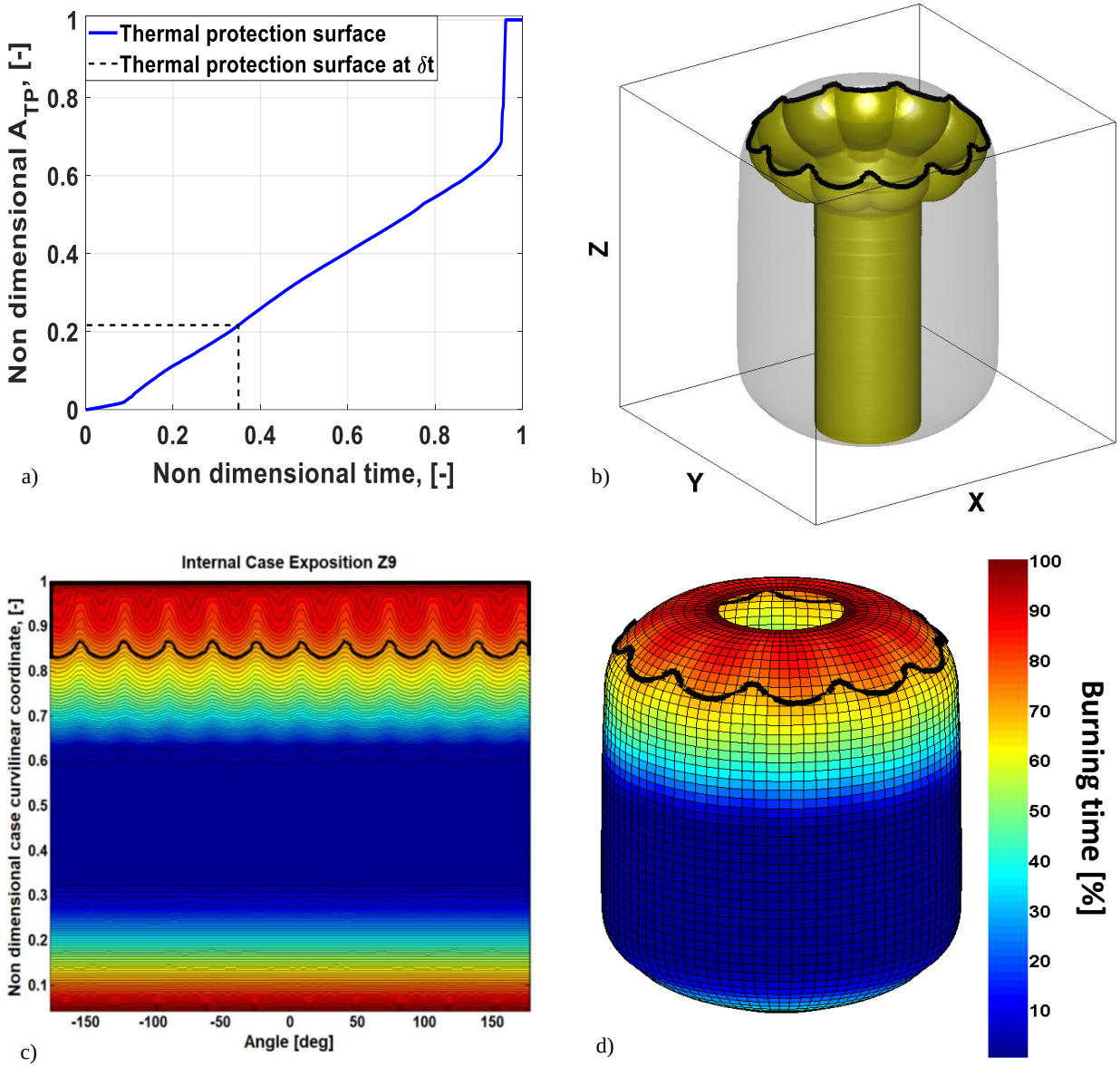

Figure 78: Thermal protection exposure at time *t.*

5.4 Numerical results

Case-insulating thermal protection analysis has been applied on ZEFIRO 23 (Z23) and ZEFIRO 9

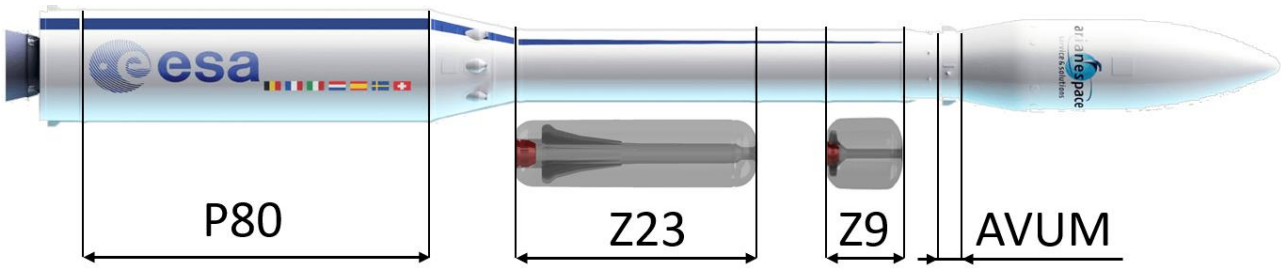

Figure 79: VEGA launcher.

(Z9), respectively the second and third stage of VEGA (European Vector of Advanced Generation) launcher (Figure 79). Vega is a single body launcher manufactured by the aerospace company Avio S.p.A. It is capable to launch a maximum payload mass of 1500 kg up to a low Earth orbit. It consists of three solid rocket motor stages (P80, Z23, Z9) and a fourth liquid engine stage, namely AVUM (Attitude and Vernier Upper Module). The main features of the second and third stages are the following ones (Table 1):

Stage	**Length,** $[\boldsymbol{m}]$	**Diameter,** $[\boldsymbol{m}]$	**Propellant mass,** $[\boldsymbol{kg}]$	**Average thrust,** $[\boldsymbol{kN}]$	**Specific impulse,** $[\boldsymbol{s}]$
Zefiro 23	7.5	1.9	24000	1122	287.5
Zefiro 9	3.9	1.9	10500	314	295.2

Table 1: Z23, Z9 data, [32]

Both Z23 and Z9 thrust chamber rely on a circular cross section grain geometry in the fore and central part, and a finocyl -shaped configuration in the rear part close to the nozzle inlet (Figure 66, Figure 67). The grain is HTPB based, where the other components are the ammonium perchlorate (oxidizer) and the aluminum powder (fuel). In the present study, the thermal protection material involved in the simulations is *X6300*. It is a nylon-phenolic based ablator, whose thermophysical properties are available in [33] and briefly listed in Table 2.

Arrhenius equation parameters		
$\boldsymbol{B}\ [1/s]$	$1.82 \cdot 10^4$	
$\boldsymbol{E_a}\ [J/mol]$	$4.66 \cdot 10^4$	
$\boldsymbol{\psi}\ [-]$	1	
Virgin material properties		
$\boldsymbol{\rho_v}\ [kg/m^3]$	1441.8	
$\boldsymbol{h_v^0}\ [J/kg]$	$-1.4 \cdot 10^6$	
$\boldsymbol{T}\ [K]$	$\boldsymbol{c_{p_v}}\ [J/(kg \cdot K)$	$\boldsymbol{k_v}\ [W/(m \cdot K)]$
300	1038	0.53

Char material properties		
$\boldsymbol{\rho_c}\ [kg/m^3]$	961.2	
$\boldsymbol{h_c^0}\ [J/kg]$	0	
$\boldsymbol{T}\ [K]$	$\boldsymbol{c_{p_c}}\ [J/(kg \cdot K)$	$\boldsymbol{k_c}\ [W/(m \cdot K)]$
370	1080	0.65
820	2235	1.94
Pyrolysis gas properties		
$\boldsymbol{h_g^0}\ [J/kg]$	0	
$\boldsymbol{c_{p_g}}\ [J/(kg \cdot K)]$	1660	
Other parameters		
$\boldsymbol{T_0}\ [K]$	298.15	
$\boldsymbol{T_I}\ [K]$	293	
$\boldsymbol{\varepsilon_{TP}}\ [-]$	0.8	
$\boldsymbol{\alpha_s}\ [-]$	1	
$\boldsymbol{V_F}\ [-]$	0.15	
$\boldsymbol{\lambda}\ [-]$	0.4	
$\boldsymbol{L}\ [m]$	0.01	
Constants		
$\boldsymbol{R}\ [J/(mol \cdot K)]$	8.31	
$\boldsymbol{\sigma}\ [W/(m^2 \cdot K^4)]$	$5.67 \cdot 10^{-8}$	

Table 2: X6300 properties, [33].

Table 2 shows some temperature-varying quantities: a linear interpolation between the temperature and each parameter has been assumed. On the other hand, quantities linked to a single temperature value are assumed constant with respect to temperature variation in time. Initial material temperature (T_I) has been considered equal to 293 K. Thermal protection material maps (Figure 80, Figure 81, Figure 82) are obtained with a time step of $10^{-4}\ s$ and a spatial step of $2 \cdot 10^{-2}\ mm$. More in detail,

Figure 80 and Figure 81 respectively identify two maps at zero level of radiated power from the nozzle and at the maximum level of such power, at time $t = 15s$. Each map is obtained dealing with heat transfer convective coefficient (h_c) and combustion chamber gases temperature (T_{gas}) as independent variables. As already pointed out in the previous subparagraphs, the output variables needed to compute SRM thrust performance are mass flow rate per unit surface of pyrolysis gases (M_g), char recession rate ($\dot{s}$), combustion chamber absorbed power ($\dot{Q}_{abs}$) to sustain the material ablation, and the material interface temperature ($T(t, x = 0)$). Furthermore, the radiative power absorbed by the

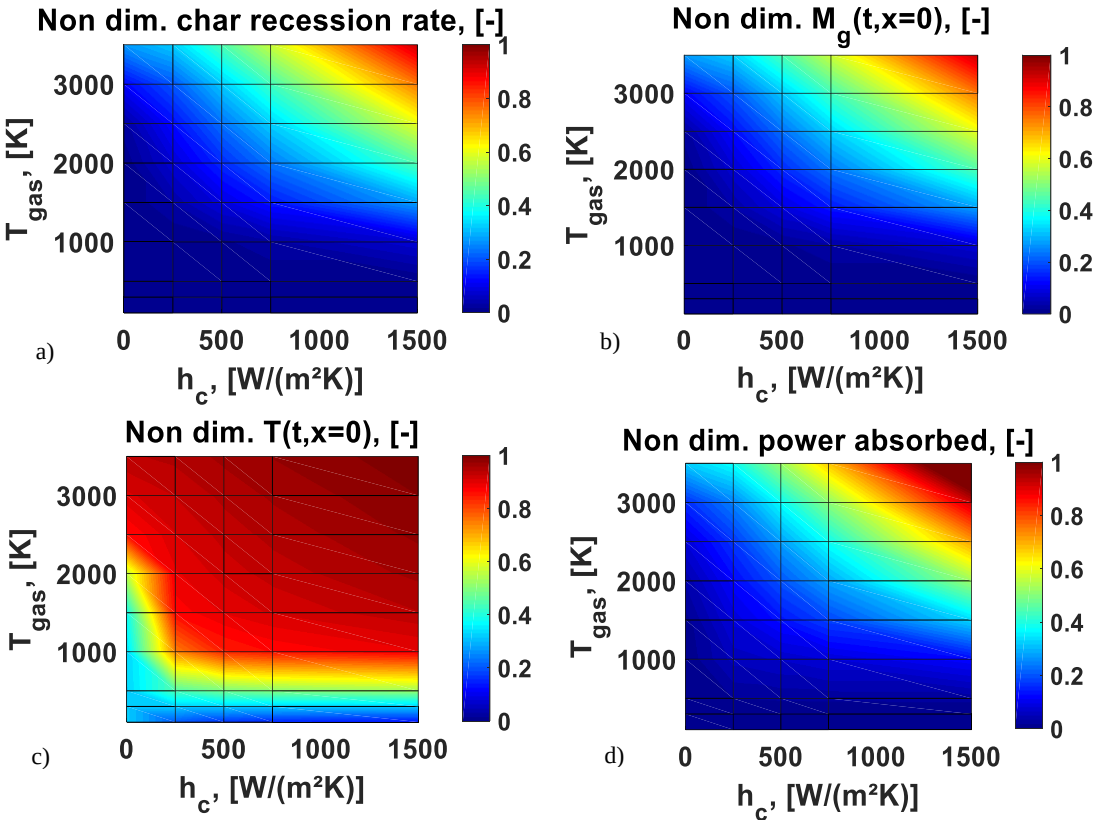

Figure 80: X6300 maps without nozzle radiation.

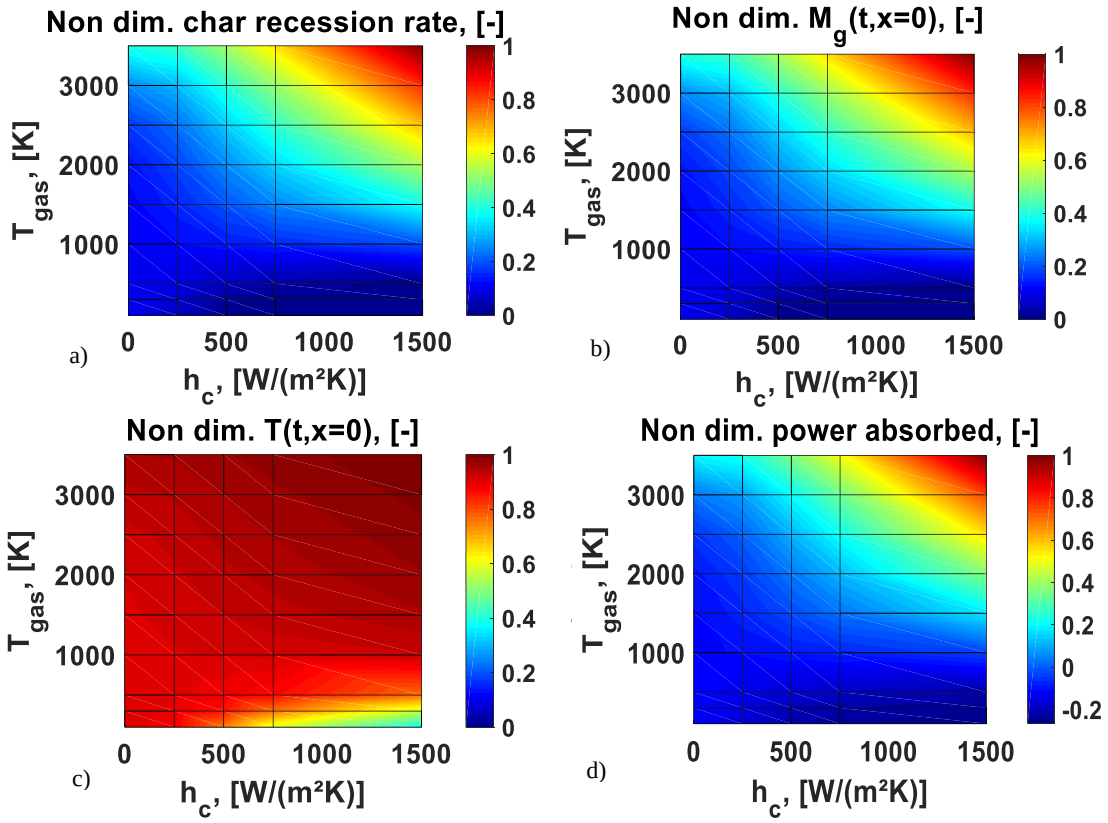

Figure 81: X6300 maps with nozzle radiation.

material from the nozzle is computed through Eq. (27) and Eq. (28) considering the shape influence of the case by means of the view factor trend along each motor axis (Figure 74). However, it must be highlighted that the above-mentioned maps belong to a larger set of maps, where each map is linked to and intermediate level of absorbed radiated power by the nozzle. Regarding such power, not all the power generated by the nozzle is taken in by thermal protection material: indeed, a portion is again absorbed by the nozzle surface due to its concave shape, the other portion is hold by combustion chamber due to their shielding effect. Nonetheless, the amount of heat absorbed by case-insulating material is enough to lead to a char recession rate and pyrolysis gases production increment close to 10 % (Figure 81a, b). That increment is even larger for near-zero value convective coefficient: at this value, the grain combustion process is already completed, thus the combustion chamber flow velocity is close to zero too. The direct consequence is that the combustion chamber convection does no longer occur toward the case-insulating material. Therefore, the only not negligible effect sustaining the thermal protection ablation is the radiation heat from the inner portion of the nozzle. The maps area bounded by $h_c \sim 0$ and $T_{gas} < 2000\ K$(Figure 80a, Figure 81a) proves the previous statement: the char recession rate without the nozzle effect is considerably lower than the char recession rate linked to nozzle radiation. The same occurs for pyrolysis gases mass flow rate per unit surface (Figure 80c, Figure 81c).

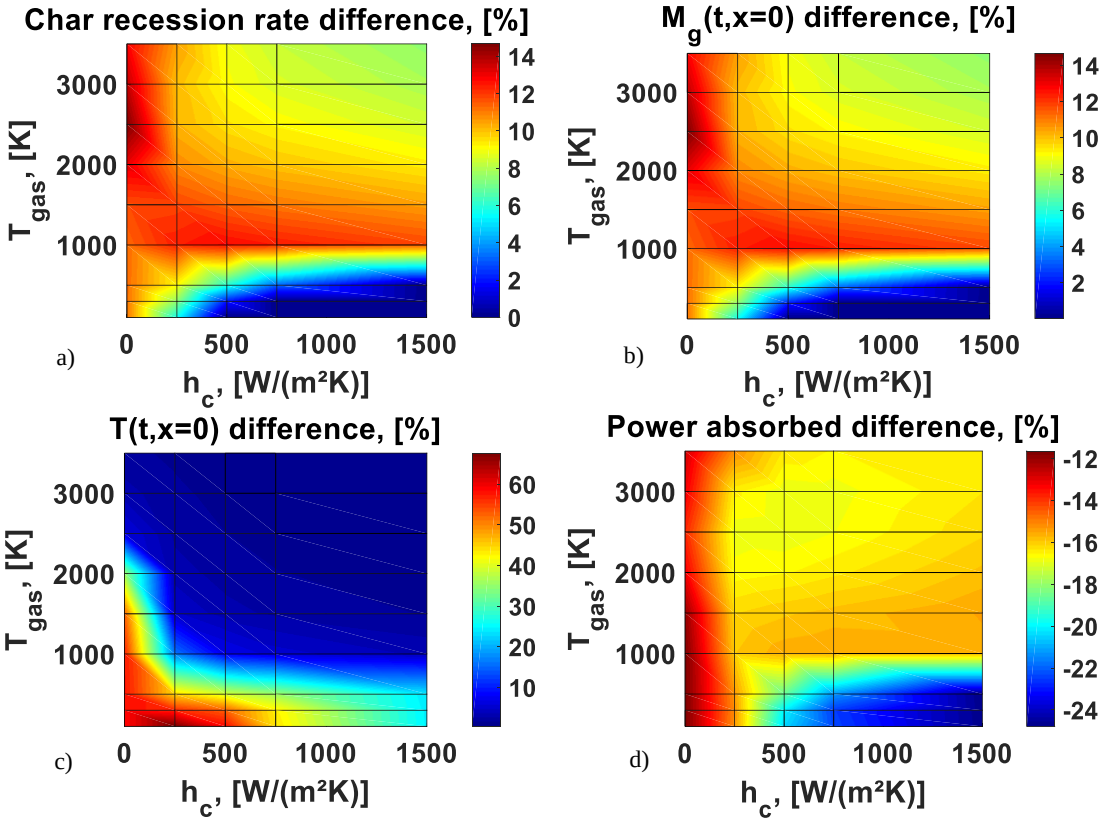

Figure 82: Difference between X6300 maps with and without nozzle radiation.

Another aspect worth to be highlighted is the reason why the absorbed power from the combustion chamber assumes negative values (Figure 81d). As mentioned before, absorbed power represents only the amount of power exchanged between thermal protections and combustion chamber hot gases; at nozzle radiation time window, the power absorbed from hot gases is lower due to the presence of additional amount of heat coming from the nozzle itself that raises thermal protection temperature. If the nozzle radiation is well-sustained and the gas temperature is low (Figure 81a, b, c in the range bounded by $T_{gas} < 500\ K$ and $h_c > 500\ {}^{W}/_{m^2K}$), it can happen that the temperature reached by the thermal protection is higher than $T_{gas}$and for this reason the heat exchange propagates in the opposite direction , thus determining the absorbed power negative value sign. Obviously the previously outlined condition is a limit case that can occur only when propellant combustion is complete and the nozzle is still hot, like for instance after tail-off. In addition to that, Figure 82 highlights the previously mentioned aspects: the maximum difference in terms of char recession rate and pyrolysis gas mass flow rate per unit surface (Figure 82a, b) is located at zero value of h_c indicating that the nozzle radiative power has a fundamental role at burn-out when grain combustion is finished. In addition, the red region in Figure 82c emphasizes the earlier achievement of ablation temperature by thermal protection with nozzle radiation contribution, giving rise to higher amounts of char recession rate.

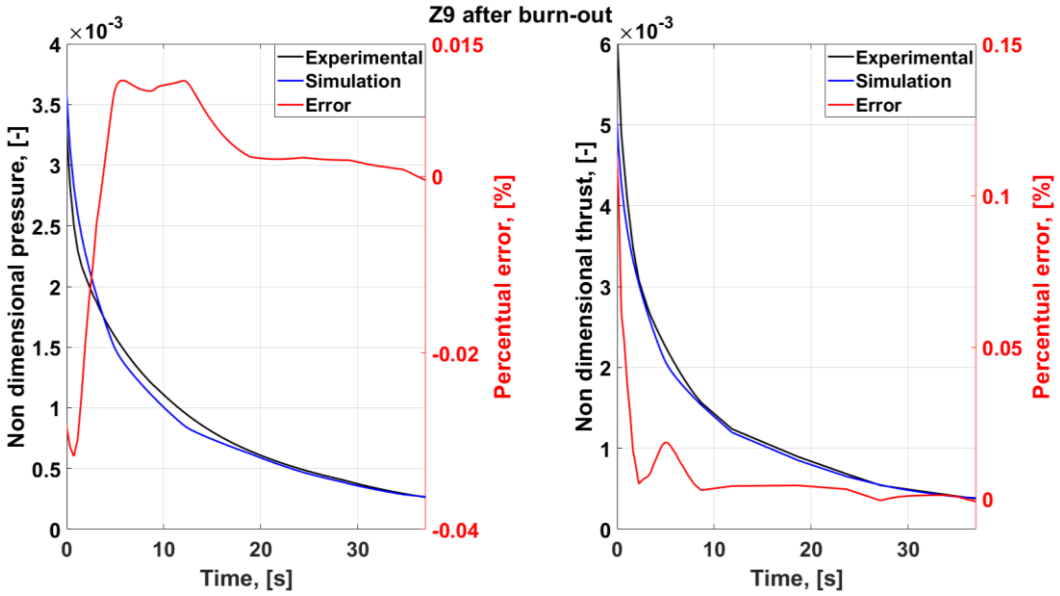

Figure 83: Zefiro 9 residual thrust.

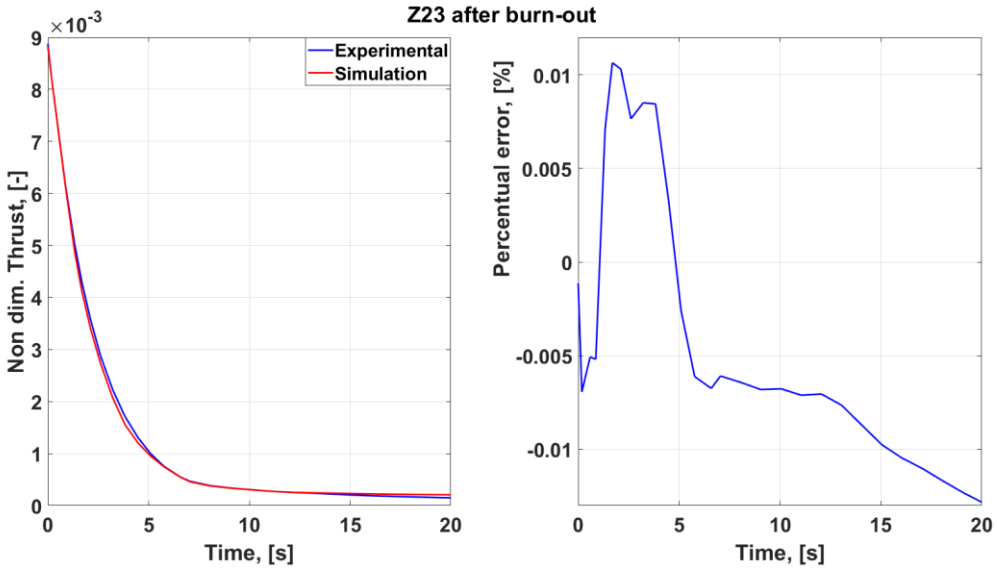

Figure 84: Zefiro 23 residual thrust.

Figure 83shows a comparison between experimental and simulated trends in terms of Z9 combustion chamber residual pressure and residual thrust after burn-out. Non dimensional pressure and thrust have been computed by dividing each value by respectively a reference pressure and thrust linked to the experimental data. Moreover, the percentual error has been evaluated as the relative percentual error with respect to the experimental curves. Pressure maximum error (absolute value) is 0.03%, while thrust error is nearly 0.12% which means that there is an acceptable match between simulation and experimental data. As it can be noticed, internal pressure (and therefore thrust) lasts for tens of seconds after burn-out and pressure levels are such that they can be usually considered negligible with respect to ambient pressure for first stage motors. This does not apply to Z9 since being a third stage means that outside pressure is almost negligible and, in addition, the total impulse produced after burn-out acts on a small residual mass, thus generating non negligible accelerations. For this reason, the ability to predict such residual thrust is fundamental to properly design the separation

procedure, both in terms of timings and separation motors total impulse. In the direction of proving the predictive ability of the above-mentioned procedure, Z23 solid rocket motor. Since Z23 has a different case size and nozzle geometry while having the same HTPB-based composite propellant and thermal protection material as Z9, maps parameters considered for Z23 residual thrust simulation are the same as the ones employed in Z9 thrust prediction, except for the view factor distribution. In fact, such quantity is different with respect to Z9 view factor because it depends on how the surface of the thermal protection case is hit by nozzle radiative power. This means that both nozzle and case geometry have an impact in predicting residual thrust behavior, however, they are determined by the motor shape. The result of the simulation for the second motor is shown in Figure 84, where the thrust has been normalized by Z23 reference thrust and the percentual error is computed as the percentual relative error with respect to the experimental data. A maximum error of 0.027 % occurs which means that the result of the Z23 simulation can be considered satisfactory. Since the residual thrust-estimation procedure has been successfully applied to two SRM configurations by using the same suitable parameters of Z9 except for the view factor, the method proposed can be recognized as predictive.

Figure 85 displays the dependance between the percentual convergence error and the grid spatial step δ_x. Specifically, the percentual convergence error is defined as the percentual relative error between each value of $M_g(t, x = 0)$ (computed on a grid with a specified value of δ_x) and the value of $M_g(t, x = 0)$ obtained at the smallest spatial step, namely $\delta_x = 5 \cdot 10^{-4}\ mm$. For the generation of each set map, the spatial step $\delta x = 2 \cdot 10^{-2}\ mm$ has been chosen with the aim of maintaining the convergence error lower than $7 \cdot 10^{-3}$ %.

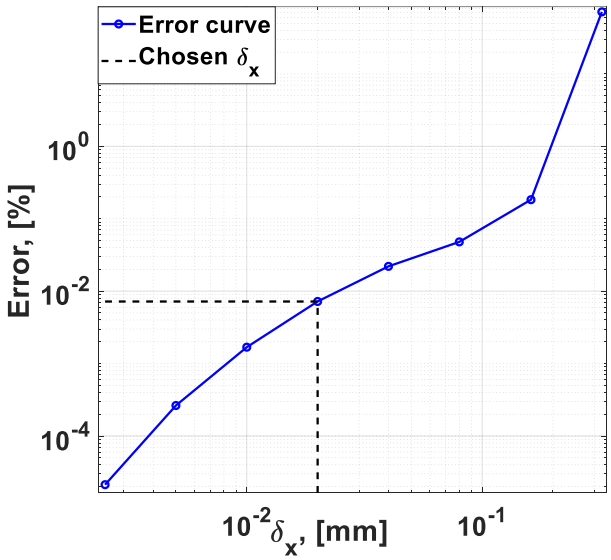

Figure 85: Grid dependence analysis.

All results previously discussed have been carried out with ROBOOST software installed on a calculator with the following features: 16 Gb RAM, Intel Core i7-7th generation CPU machine with 3.10 GHz and NVIDIA Quadro M1200 graphic card. The two maps generation process lasted 48 hrs., instead Z9 internal ballistic simulation lasted 1 hr.

5.5 Conclusions

Coupling between the mathematical-physical model of thermal protection material ablation and solid rocket motor combustion chamber ballistics has been established in order to prove the nozzle as the

main factor sustaining material ablation at tail-off phase, and hence generating the residual thrust. The procedure consists of the following steps. First, ablation maps have been obtained solving the mathematical set of equations through the finite-difference approach. Second, those maps are integrated in ROBOOST software, by which thrust – time profile has been carried out for the two solid rocket motors, namely Z23 and Z9. Then simulation results have been verified through experimental uncertainty bandwidths. A quite appreciable matching has been obtained regarding the two rockets, allowing the model to be reliable in predicting residual thrust for SRMs, other than Z9 or Z23.
Future developments will be focused on the evaluation of how the transient char formation during material ablation affects the production of pyrolysis gases, and therefore the residual thrust profile.

References

[1] Boraas, S., Hyland, B., and Smart, L., "Predicted Post Burn Residual Thrust for an Orbital Transfer Motor," AIAA Paper 1985-1395, July 1985.
https://doi.org/10.2514/6.1985-1395

[2] Chang, I-S., "Slag and Enviroment of a Spinning Rocket Motor," Journal of Spacecraft and Rockets, vol. 28, no. 5, 1991, pp. 599-605.
https://doi.org/10.2514/3.26286

[3] Akiba, R., and Kohno, M., "Experiments with Solid Rocket Technology in the Development of M-3SII," Acta Astronautica, vol. 13, no. 6/7, 1986, pp. 349-361.
https://doi.org/10.1016/0094-5765(86)90090-1

[4] Ponti, F., Souhair, N., Mini, S., and Annovazzi, A., "0D Unsteady - 1D Quasi-Stationary Internal Ballistic Coupling for ROBOOST Simulation Tool," AIAA Paper 2019-4140, August 2019.
https://doi.org/10.2514/6.2019-4140

[5] Ponti, F., Mini, S., and Annovazzi, A., "Numerical Evaluation of the Effects of Inclusions on Solid Rocket Motor Performance," *AIAA Journal*, Vol. 58, No. 9, 2020, pp. 4028-4036.
https://doi.org/10.2514/1.J058735

[6] Ponti, F., Mini, S., and Annovazzi, A. , "A Simplified Approach to Predict Friedman Curl Effect in a Solid Rocket Motor using ROBOOST Simulation Tool," AIAA Paper 2019-3960, August 2019.
https://doi.org/10.2514/6.2019-3960

[7] Swann, R., T., Dow, M., B., and Tompkins, S., S., "Analysis of the Effects of Enviromental Conditions on the Performance of Charring Ablators," Journal of Spacecraft and Rockets, vol. 3, no. 1, 1966, pp. 61-67.
https://doi.org/10.2514/3.28386

[8] Blosser, M., L., "Fundamental Modeling and Thermal Performance Issues for Metallic Thermal Protection System Concept," Journal of Spacecraft and Rockets, vol. 41, no. 2, 2004, pp. 195-206.
https://doi.org/10.2514/1.9182

[9] Bahramian, A., R., Kokabi, M., Famili, M., H., N., and Beheshty, M., H., "Ablation and Thermal Degradation Behaviour of a Composite Based on Resol Type Phenolic Resin: Process Modeling and Experimental," Polymer, vol. 47, no. 10, 2006, pp. 3661-3673.
https://doi.org/10.1016/j.polymer.2006.03.049

[10] Li, W., Huang, H., Tian, Y., and Zhao, Z., "A Nonlinear Pyrolysis Layer Model for Analyzing Thermal Behavior of Charring Ablator," International Journal of Thermal Sciences, vol. 98, December 2015, pp. 104-112.
https://doi.org/10.1016/j.ijthermalsci.2015.07.002

[11] Amar, A., J., Blackwell, B., F., and Edwards, J., R., "One-Dimensional Ablation Using a Full Newton's Method and Finite Control Volume Procedure," Journal of Thermophysics and Heat Transfer, vol. 22, no. 1, 2008, pp.71-82.
https://doi.org/10.2514/1.29610

[12] Amar, A., J., Blackwell, B., F., and Edwards, J., R., "Development and Verification of a One-Dimensional Ablation Code Including Pyrolisis Gas Flow," Journal of Thermophysics and Heat Transfer, vol. 23, no. 1, 2009, pp. 59-71.
https://doi.org/10.2514/1.36882

[13] Mohammadiun, H., and Mohammadiun, M., "Numerical Modelling of Charring Material Ablation with considering Chemical-Reaction Effects, Mass Transfer and Surface Heat Transfer," Arabian Journal for Science and Engineering, vol. 38, December 2013, pp. 2533-2543.
https://doi.org/10.1007/s13369-012-0510-0

[14] Covington, M., A., Heinemann, J., M., Goldstein, H., E., Chen, Y., K., Terrazas-Salinas, I., Balboni, J., A., Olejniczak, J., and Martinez, E., R., "Performance of a Low Density Ablative Heat Shield Material," Journal of Spacecraft and Rockets, vol. 45, no. 2, 2008, pp. 237-247.
https://doi.org/10.2514/1.12403

[15] Chen, Y., K., and Milos, F., S., "Ablation and Thermal Response Program for Spacecraft Heatshield Analysis," Journal of Spacecraft and Rockets, vol. 36, no. 3, 1999, pp. 475-483.
https://doi.org/10.2514/2.3470

[16] Chen, Y., K., and Milos, F., S., "Ablation and Thermal Response Program for Spacecraft Heatshield Analysis," Journal of Spacecraft and Rockets, vol. 36, no. 3, 1999, pp. 475-483
https://doi.org/10.2514/2.3470

[17] Milos, F., S., and Chen, Y., K., "Ablation, Thermal Response, and Chemistry Program for Analysis of Thermal Protection Systems," Journal of Spacecraft and Rockets, vol. 50, no. 1, 2013, pp. 137-149.
https://doi.org/10.2514/1.A32302

[18] Milos, F., S., and Chen, Y., K., "Ablation and Thermal Response Property Model Validation for Phenolic Impregnated Carbon Ablator," Journal of Spacecraft and Rockets, vol. 47, no. 5, 2010, pp. 786-805.
https://doi.org/10.2514/1.42949

[19] Lachaud, J., Van Eekelen, T., Scoggins, J., B., Magin, T., E., and Mansour, N., N., "Detailed Chemical Equilibrium Model for Porous Ablative Materials," International Journal of Heat and Mass Transfer, vol. 90, November 2015, pp. 1034-1045.
https://doi.org/10.1016/j.ijheatmasstransfer.2015.05.106

[20] Lachaud, J., and Mansour, N., N., "Porous-Material Analysis Toolbox Based on OpenFOAM and Applications," Journal of Thermophysics and Heat Transfer, vol. 28, no. 2, 2014, pp. 191-202.
https://doi.org/10.2514/1.T4262

[21] Lachaud, J., Scoggins, B., J., Meyer, M., G., and Mansour, N., N., "A Generic Local Thermal Equilibrium Model for Porous Reactive Materials submitted to High Temperatures," International Journal of Heat and Mass Transfer, vol. 108, May 2017, pp. 1406-1417.

https://doi.org/10.1016/j.ijheatmasstransfer.2016.11.067

[22] Huang, J., Yao, W. X., Shan, X., Y., and Chang, C., "Coupled-Fluid-Structural Thermal Numerical Methods for Thermal Protection System," AIAA Journal, vol. 57, no. 8, 2019, pp. 3630-3638.
https://doi.org/10.2514/1.J057616

[23] Wang, Y., Risch, T., K., and Pasiliao, C., L., "Modeling of Pyrolyzing Ablation Problem with ABAQUS: A One-Dimensional Test Case," Journal of Thermophysics and Heat Transfer, vol. 32, no. 2, 2018, pp. 542-545.
https://doi.org/10.2514/1.T5274

[24] Mathieu, R., D., "Mechanical Spallation of Charring Ablators in Hyperthermal Enviroments," AIAA Journal, vol. 2, no. 9, 1964, pp. 1621-1627.
https://doi.org/10.2514/3.2629

[25] Dec, J., A., Braun, R., D., and Laub, B., "Ablative Thermal Response Analysis Using the Finite Element Method," Journal of Thermophysics and Heat Transfer, vol. 26, no. 2, 2012, pp. 201-213.
https://doi.org/10.2514/1.T3694

[26] Moyer, C., B., and Rindal, R., A., "An Analysis of the Coupled Chemically Reacting Boundary Layer and Charring Ablator. Part 2- Finite Difference Solution for the In-Depth Response of Charring Materials Considering Surface Chemical and Energy Balances," NASA CR-1061, June 1968.

[27] Schoner, R., J., "User's Manual Aerotherm Charring Material Thermal Response and Ablation Program," Air Force Rocket Propulsion Laboratory, AFRPL-TR-70-92, April 1970.

[28] Bergman, T., L., Lavine, A., S, L., Incropera, F., P., and Dewitt, D., P., "Fundamental of Heat and Mass Transfer", Radiation: Processes ad Properties, 7th ed, John Wiley & Sons Inc., 2011, pp. 768-830.

[29] Dombrovsky, L. A., "Radiation Heat Transfer in Disperse Systems," Radiative and Combined Heat Transfer Problems, 1st ed., Begell House Inc. Publ., New York, 1995, pp. 145-239.

[30] Chen, Y., K., and Milos, F., S., "Navier-Stokes Solutions with Finite Rate Ablation for Planetary Mission Earth Reentries," Journal of Spacecraft and Rockets, vol. 42, no. 6, 2005, pp. 961-970.
https://doi.org/10.2514/1.12248

[31] Ponti, F., Souhair, N., Mini, S., and Annovazzi, A., "0D Unsteady - 1D Quasi-Stationary Internal Ballistic Coupling for ROBOOST Simulation Tool," AIAA Paper 2019-4140, August 2019.
https://doi.org/10.2514/6.2019-4140

[32] https://www.avio.com/it/vega

[33] Williams, S., D., and Curry, D., M., "Thermal Protection Materials," NASA RP-1289, December 1992.

Chapter 6

6 Conclusions

In this work, several phenomena affecting solid rocket motors performance were addressed.
First, ROBOOST software has been discussed since it represents the chosen software aimed to obtain SRMs burning surface, pressure and thrust behaviors with respect to combustion time. It relies on a 3D burning surface regression which is discretized as a dynamic triangular mesh. This allows the code to analyze burning rate variations since each vertex displacement is managed independently. Furthermore, it enables the possibility to investigate grain cavities/debondings. A self-intersection removal algorithm has been established and tested in the direction of integrating the SRM main burning surface with the cavity/debonding surface.
Second, an analysis involving the combustion chamber pressure variation and the case-insulating thermal protection material exposure has been performed. A novel effective procedure, meant to predict debonding impact on case material exposure, has been also presented.
Third, an example of burning rate anisotropy is addressed. Such anisotropy is linked to the Friedman Curl effect which has been supposed to appear due to particle segregation in SRM casting process. Friedman curl pressure peak has been discussed with respect to Baria SRMs where it appears nearly at the end of the combustion before the combustion chamber pressure drop.
Last, thermal protection ablation behavior has been investigated in order to theoretically explain the residual thrust after burn-out time of two SRMs, namely ZEFIRO 9 and ZEFIRO 23. The nozzle region within the combustion chamber has been proven to be the main factor leading to the ablation of the case-insulating thermal protection material after burn-out time when the propellant is almost depleted.